MONTAN
UNIVERSITÄT
LEOBEN

Chair of Reservoir Engineering

Master's Thesis

Direct numerical pore-scale simulations of biomass induced changes on hydraulic properties of porous media

Daniel Grogger, BSc

November 2022

MONTANUNIVERSITÄT LEOBEN
www.unileoben.ac.at

EIDESSTATTLICHE ERKLÄRUNG

Ich erkläre an Eides statt, dass ich diese Arbeit selbständig verfasst, andere als die angegebenen Quellen und Hilfsmittel nicht benutzt, und mich auch sonst keiner unerlaubten Hilfsmittel bedient habe.

Ich erkläre, dass ich die Richtlinien des Senats der Montanuniversität Leoben zu "Gute wissenschaftliche Praxis" gelesen, verstanden und befolgt habe.

Weiters erkläre ich, dass die elektronische und gedruckte Version der eingereichten wissenschaftlichen Abschlussarbeit formal und inhaltlich identisch sind.

Datum 27.10.2022

Unterschrift Verfasser/in
Daniel Grogger

Daniel Grogger, BSc

Master Thesis 2022

Petroleum Engineering

Direct numerical pore-scale simulations of biomass induced changes on hydraulic properties of porous media

Supervisor: Univ.-Prof. Dipl.-Phys. Dr. rer. nat. Holger Ott

Co-Supervisor/Advisor: Dipl.-Ing. Patrick Jasek

Chair of Reservoir Engineering

dpe DEPARTMENT PETROLEUM ENGINEERING

MONTAN UNIVERSITÄT

Dedicated to my beloved family and girlfriend,

who supported me throughout my entire life.

Acknowledgements

I would like to thank Prof. Holger Ott for his supervision throughout the entire process of writing my master’s thesis.

Furthermore, I thank my co-supervisor, Patrick Jasek, for his daily guidance and organization of the thesis writing process. Other big thanks go out to Saeid Sadeghnejad (University Mainz) and Pit Arnold for introducing me to the software “GeoDict” and providing me the possibility to be part of helpful discussions to expand insights and gain and strengthen knowledge on this topic. Additionally, they provided me with simulation macro and python codes and supported me in coding necessary scripts.

Finally, I want to thank my girlfriend, family and friends, who supported me constantly during my academic studies and beyond.

Abstract

The global energy demand is continuously rising and requires a significant transition to reduce greenhouse gases (GHG), reduce the ecological footprint of fossil resources and foster the expansion of renewable energies. The current European energy mix requires a meaningful change to reach the agreed 2 °C target and become a vastly net-zero economy by 2050.

The concept of large-scale underground energy storage, so-called “Geo-Batteries”, could significantly increase the stored energy volume, enable seasonal on and offloading, and balance the increased demand in winter. During hydrogen storage operations in sedimentary rocks, a side-effect of microbial methanation was detected, which led to the concept of underground energy conversion. Hereby, the injected hydrogen (H_2) and carbon dioxide (CO_2) is converted to methane (CH_4) by hydrogenotrophic methanogens. The production of methane by microorganisms from carbon dioxide and hydrogen solves two environmental problems. It captures CO_2 cutting down greenhouse gas emissions by forming a sustainable carbon cycle. Additionally, retrieved hydrogen and methane can be used for electricity and heat generation. Pilot projects investigate the controlling parameters to increase significant conversion rates and resolve the impact of biomass accumulation on storage capacity and operational conditions.

Experiments on the pore scale are necessary to describe the behavior of microorganisms and the accompanying chemical reactions. The presence and growth of microorganisms can significantly change a porous medium’s hydraulic properties. This thesis uses a “Digital Twin” approach to resolve the biomass-induced effects on the porous medium by direct numerical simulations. The task is to develop a numerical model to simulate flow in a micro model occupied by microorganisms and verify the porosity-permeability relationship with experimental results. For this, an archean culture, Methanobacterium formicicum (M. formicicum), was used and inoculated in the micro model (MM). The workflow included an improvement of a previously developed and deployed numerical twin. The MM curvature and bifurcating inflow and outflow channels were analyzed to estimate their impact on the solution. Those additional features are necessary to resolve the porosity-permeability development and extract meaningful velocity and stress fields.

The temporal velocity and stress distributions play a significant role in biofilm reconfiguration, preferential flow path formation, and intra-biomass permeability. The velocity and stress fields were analyzed using histograms and the results revealed that the net accumulation of biomass

decreased the hydraulic properties following a power law. As a result, narrower pore channels led to increased velocities and shear stresses in the domain. Moreover, the width of the histograms increased over time and a bimodal distribution of the velocity and stress peaks was detected. This refers to the assumed intra-biomass permeability and is first noticed with the onset of biomass accumulation.

This master thesis attempts to contribute to a continuing understanding of the underground hydrogen storage (UHS) concept. The primary objective of this thesis was to enhance the modeling workflow necessary to simulate velocity and stress fields, which are significant for biomass characterization in porous media.

Zusammenfassung

Der weltweite Energiebedarf steigt kontinuierlich an und erfordert einen bedeutenden Wandel, um Treibhausgase zu reduzieren, den ökologischen Fußabdruck fossiler Ressourcen zu verringern und den Ausbau erneuerbarer Energien zu fördern. Der derzeitige europäische Energiemix muss grundlegend geändert werden, um das vereinbarte 2 °C Ziel zu erreichen und bis 2050 zu einer weitgehend treibhausfreien Wirtschaft zu werden.

Das Konzept der groß angelegten unterirdischen Energiespeicherung, der so genannten „Geo-Batterien“, könnte das gespeicherte Energievolumen erheblich vergrößern, ein saisonales Ein- und Ausladen ermöglichen und die erhöhte Nachfrage im Winter ausgleichen. Bei der Wasserstoffspeicherung in Sedimentgestein wurde ein Nebeneffekt der mikrobiellen Methanisierung festgestellt, der zum Konzept der unterirdischen Energieumwandlung führte. Dabei wird der eingebrachte Wasserstoff (H_2) und Kohlendioxid (CO_2) von hydrogenotrophen Methanogenen in Methan (CH_4) umgewandelt. Die Produktion von Methan durch Mikroorganismen aus Kohlendioxid und Wasserstoff löst zwei Umweltprobleme. Sie bindet CO_2 und verringert so die Treibhausgasemissionen, indem sie einen nachhaltigen Kohlenstoffkreislauf bildet. Außerdem können der gewonnene Wasserstoff und das Methan zur Strom- und Wärmeerzeugung genutzt werden. In Pilotprojekten werden die Steuerungsparameter zur Erhöhung der Umwandlungsraten untersucht und die Auswirkungen der Biomasseakkumulation auf die Speicherkapazität und die Betriebsbedingungen geklärt.

Experimente im Porenmaßstab sind notwendig, um das Verhalten von Mikroorganismen und die begleitenden chemischen Reaktionen zu beschreiben. Die Anwesenheit und das Wachstum von Mikroorganismen können die hydraulischen Eigenschaften eines porösen Mediums erheblich verändern. In dieser Arbeit wird ein „Digitaler Zwilling“-Ansatz verwendet, um die durch die Biomasse verursachten Effekte auf das poröse Medium durch direkte numerische Simulationen zu lösen. Die Aufgabe dieser Arbeit besteht darin, ein numerisches Modell zu entwickeln, um die Strömung in einem von Mikroorganismen besetzten Mikromodell zu simulieren und die Porositäts-Permeabilitäts-Beziehung mit experimentellen Ergebnissen zu verifizieren. Hierfür wurde eine archäische Kultur von Methanobakterien (M. formicicum) verwendet und in das Mikromodell injiziert. Der Arbeitsablauf beinhaltet eine Verbesserung eines zuvor entwickelten und eingesetzten numerischen Zwillings. Die Krümmung des Mikromodells und die sich verzweigenden Zu- und Abflusskanäle wurden analysiert, um ihre

Auswirkungen auf die Simulationsergebnisse abzuschätzen. Diese zusätzlichen Merkmale sind notwendig, um die Porositäts-Permeabilitäts-Beziehung aufzulösen und aussagekräftige Geschwindigkeits- und Spannungsfelder zu extrahieren.

Die zeitlichen Geschwindigkeits- und Spannungsverteilungen spielen eine wichtige Rolle bei der Rekonfiguration des Biofilms, der Bildung bevorzugter Fließwege und der Durchlässigkeit innerhalb der Biomasse. Die Geschwindigkeits- und Spannungsfelder wurden anhand von Histogrammen analysiert und die Ergebnisse zeigten, dass die Nettoakkumulation von Biomasse die hydraulischen Eigenschaften nach einem Potenzgesetz verringert. Infolgedessen führten engere Porenkanäle zu höheren Geschwindigkeiten und Scherspannungen in dem Simulationsmodell. Außerdem nahm die Breite der Histogramme mit der Zeit zu und es wurde eine bimodale Verteilung der Geschwindigkeits- und Spannungsspitzen festgestellt. Dies bezieht sich auf die angenommene Durchlässigkeit innerhalb der Biomasse und wird erst mit dem Beginn der Biomasseakkumulation festgestellt.

Diese Masterarbeit soll einen Beitrag zum weiteren Verständnis des Konzepts der unterirdischen Wasserstoffspeicherung leisten. Das Hauptziel dieser Arbeit ist es, den Modellierungsablauf zu verbessern, der für die Simulation von Geschwindigkeits- und Spannungsfeldern für die Charakterisierung von Biomasse in porösen Medien erforderlich ist.

Table of Contents

Chapter 1

Introduction

The rising importance of affordable energy, accompanied by the increasing energy demand, created the foundation for a rapidly expanding Oil & Gas business. It has become one of the critical industries, responsible not only for the growth of the world's biggest economies but also the symbol of power and modern wealth in the world we know today.

The worldwide population and energy demand will rise in the coming decades, accelerating greenhouse gas emissions to exorbitant volumes. In 2019 the total final energy consumption summed up to 418 Eta Joule of energy (IEA, 2019). Depending on the scenario forecasts from (BP Energy Outlook, 2022), total final consumptions range between 480-520 Eta joule for 2030. It will be the duty of the energy industry to provide affordable and clean energy and simultaneously encourage decarbonization in the future by increasing efficiency and advocating lower consumption.

Climate change is one of the most discussed topics in the world in the current century. However, due to the initializations of climate demonstrations, it was first officially addressed in the Paris Agreement in 2015. Since then, plans and arrangements have been met to keep below the 1,5 °C warming scenario (*The Paris Agreement | UNFCCC*, 2015). The discussion of keeping greenhouse gas emissions low and simultaneously providing the security of supply will be one of the most significant challenges for industry and policymakers. Especially in Europe, Russia's dependencies on gas and oil were painfully depicted in the current geopolitical situation - the Ukrainian-Russian conflict (2022). These circumstances force the policymakers in Central Europe to rethink the energy system and supply of energy, understand the dependencies of other countries and start to implement creative and efficient solutions toward decentralized and CO_2-reduced or even net-zero energy systems in the future.

Applying new technologies like subsurface hydrogen storage for long-term energy storage combined with an engineered offset of emissions by implementing Carbon Capture and Storage

(CCS) will be inevitable to succeed in the race of the energy transition and balance the worldwide rising energy demand and its accompanying emissions. Renewable and conventional energy resources and their various technologies need a well-integrated system in short- to midterm. Discontinuous energy production from renewable sources combined with fluctuation in consumption will cause supply issues and require a long-term solution for energy storage. Surplus electricity cannot be stored under every circumstance and might lead to grid stability malfunctions and overloading. So, finding technologies that can store excessive energy is necessary. The Power-to-Gas technologies can vitally contribute to the production of underground storable hydrogen through water electrolysis. Suitable storage options like salt caverns are all well-studied. In contrast, others, like sedimentary rocks, known from oil and gas exploration, have not yet reached socio-political acceptance in many parts of Europe.

However, the current status quo needs to be questioned. Both ends of the energy value chain, producer and consumer, reveal significant potential for improvement and must undergo an effective change to tackle the climate crisis by implementing robust solutions to resolve the energy crisis. Several available technologies provide solutions to a sustainable energy portfolio reducing the fraction of fossil energy carriers and all of them will need to play a role in the future to balance long and short-term demands of electricity and heat supply. An essential role in increasing the efficiency of renewably produced electricity by wind parks or photovoltaic farms, is its storage at sufficient huge capacities. The production and demand envelope for renewable energy is not perfectly aligned, thus creating gaps where constant producing powerplants like nuclear or coal-fired plants secure the grid stability by providing the minimum power demand baseload.

Hydrogen, with its high gravimetric energy density of 33,33 kWh/kg (idealhy, 2013), is an excellent energy carrier and allows the surplus of produced green electricity to be compressed, transported and stored. As the smallest molecule, hydrogen has a four times higher diffusion coefficient of 0,61 cm^2/s than methane and is, in this respect, challenging to handle. Moreover, it is a non-toxic, non-oxidizing, colorless gas with its lower and upper explosion limit in the air of 18,3 and 59 Vol. [%], respectively. H_2 produced from renewable energy is also called green hydrogen and can be used in fuel cells to produce electricity to power households, heat pumps, and electric vehicles or blend with natural gas. Natural gas, in general, will serve as a bridging technology, regardless of its origin and modification. Natural gas, biogenic gas, or hydrogen can fundamentally reduce the CO_2 footprint by replacing coal and diesel-fired powerplants and replacing the grey hydrogen production from natural gas reforming.

At this point, the petroleum industry significantly contributes with substantial experience and data in the development of subsurface storage facilities. Surplus energy created from renewable energy is converted to hydrogen and might be stored in depleted gas, oil reservoirs, or salt caverns. The storage of unrefined petroleum or gas was already practiced in salt caverns since the 1980's in Germany. During this time, unconventional concepts for storing liquified natural gas or even hydrogen in salt caverns were discussed and since then, the idea of underground hydrogen storage has been born (Thomas and Gehle, 2000).

These hydrogen storage options are so-called "Geo-Batteries", which might outperform any other storage facility on the surface in terms of capacity and cost efficiency, especially if predeveloped fields are utilized. Battery storage is already well-known and will be fostered. Due to its limitations (e.g., low energy density and high initial costs), it needs further research and development in the future. Other available storage options are supercapacitors, flywheels, compressed air and pumped storage facilities. As depicted in Figure 1, the technologies "Power-to-Gas Methane" and "Power-to-Gas Hydrogen" have the most considerable storage capacity. They outperform any other type of storage regarding storage capacity. Combined with geological structures, it can be the backbone of the sustainable energy system for many years. The Power-to-Gas process is the conversion of electricity to another form of energy. In literature, often referred to as Power-to-X (PtX), where P represents the surplus power of renewables and X stands for the transformed energy source, like chemicals, methane, or hydrogen (Hassannayebi, 2019).

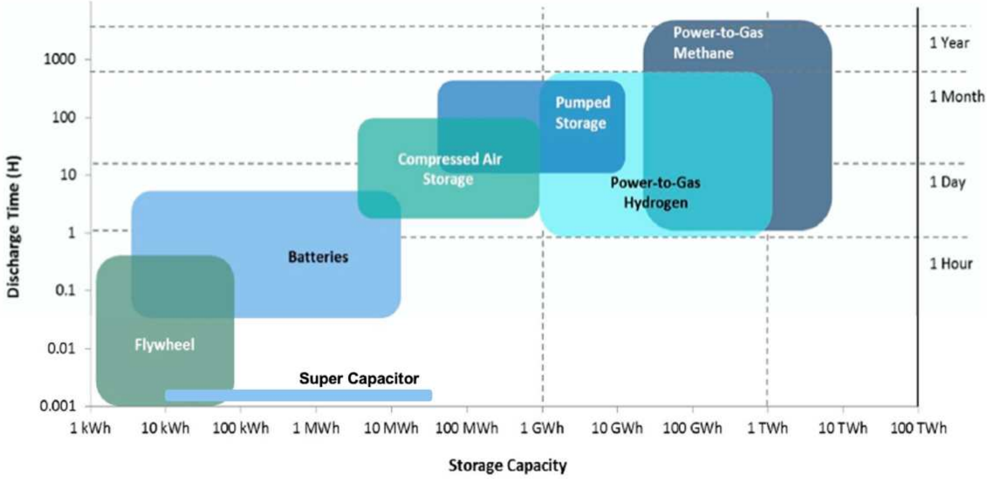

Figure 1: Comparison of storage technologies displaying the storage capacity vs. discharge time [adapted and modified, originally from (Moore and Shabani, 2016)].

Hydrogen gas properties provide technical problems with storage and transport. High pressures and low temperatures require costly materials for storage in surface tanks or transport vessels. Subsurface environments may provide a suitable environment for storing hydrogen and provide an alternative option for reusing depleted gas or oil reservoirs. Underground hydrogen storage can be fundamental to forging a hydrogen-based energy economy. Water electrolysis powered by renewable energy creates hydrogen, which will act as the storage gas due to its flexible and effective energy carrier properties.

Furthermore, the Carbon Capture Utilization and Storage (CCUS) technology is a viable and necessary solution according to the IPCC projection, where CO_2 from industrial processes or direct from the air is captured and re-injected to storage sites in close vicinity. In pilot projects, where hydrogen and carbon dioxide were injected simultaneously, side effects of methanation were detected. The same green gas can be produced during biomass and wastewater fermentation. H_2 and CO_2 are injected into a suitable depleted gas reservoir for conversion into methane by the natural metabolic processes carried out by archaea microorganisms. H_2 and CO_2 act as nutrients for the microorganisms. The product is biogenic natural gas, which can be stored in this reservoir, withdrawn when needed, and transported to customers via the existing pipeline infrastructure. The equation can be simple break down to “Wind + Sun = Green Gas” (RAG Austria AG, 2021). An area-wide eradication of this technology can reduce the dependency on gas exports in Europe, especially from Russia. The importance of renewable energy resources is evident in our future energy mix. “Despite this, the inherent intermittency of variable renewable energy sources remain an obstacle to their widespread adaption” (Stolten *et al.*, 2020).

Experiments on the pore scale are necessary to reveal the behavior of microorganisms under multiphase flow conditions and investigate the limiting factors of efficient chemical conversion of methane. Microbe’s presence and growth change the porous medium’s hydraulic properties, affecting both permeability and porosity. It is vital to understand this behavior for underground hydrogen storage and, therefore, necessary to study it as it was done for enhanced oil recovery methods. Therefore, direct numerical simulations via a “Digital Twin” approach were conducted to simulate the flow in a micro model with varying biomass permeabilities. The aim was to match experimental data and estimate the remaining base permeability of the implemented micro model, an engineered reservoir resembling a borosilicate chip. Velocity and resulting stress distributions play a significant role in biofilm attachment and detachment and are of particular interest. In the end, a representative elementary volume analysis was conducted to investigate the degree of heterogeneity of the simulation domain with respect to varied injection flow rates at different timesteps.

1.1 Hydrogen, the energy carrier of tomorrow?

“Hydrogen is considered the most promising alternative energy source due to its carbon-free nature and a wide variety of uses. Nevertheless, some issues related to the role of hydrogen are still unsolved” (Stolten *et al.*, 2020). Hydrogen has an essential potential to accelerate the process of scaling up clean and renewable energy. However, its integration into power systems remains little studied (Yue *et al.*, 2021).

Hydrogen will be the perfect energy carrier for the “energy system of tomorrow” and enable various possibilities. Hydrogen has an energy density of 120 MJ/kg, which is numerous times higher than gasoline (45,8 MJ/kg) or diesel (45,5 MJ/kg). Even with a lithium-ion battery with today’s technology, hydrogen has a higher energy density (lithium-ion energy: 0,3 MJ/kg) (Saracco, 2021).

If one m^3 of hydrogen is burned, 12,7 MJ is created, a very high potential. But it is less compared to methane, which creates 40 MJ. The downside of producing hydrogen is that more energy is needed to fabricate one unit of energy than it will contribute to one’s system. This implies that H_2 is not seen as an energy source but rather an efficient energy carrier due to its easy conversion into electricity and minor loss during transportation. The losses of hydrogen transportation are less than for a gaseous carrier options (< 0,1% - average loss during transportation) and the traditional power grid transportation (~ 8% - average loss during transportation) (Zivar, Kumar and Foroozesh, 2020).

Hydrogen is a simple element with the lowest atomic mass and it can be found in more than 90% of the world’s atoms and molecules. It is a non-toxic, colorless and odorless gas. Under room temperature and an ordinary pressure regime, hydrogen is gaseous and obtains a density of approximately 0,09 kg/m^3. With increasing pressure, the density increases to 16 kg/m^3 (Gasunie - Crossing borders in energy, 2022).

The hydrogen demand is growing massively in the energy transition to a net-zero emission world. H_2 is not naturally isolated and not available in a solitary state, therefore, it must be extracted from molecules such as water (H_2O) or methane (CH_4). The considerable challenge is producing efficient and low-carbon hydrogen from the named molecules, which requires enormous energy. The central part of today’s supplied hydrogen is grey and brown, which is carbon-emitting hydrogen. In 2018, over 95 % of the provided hydrogen came from fossil fuels (IRENA, 2018). However, due to strong policy support and massive cost reductions for hydrogen production in the future, green and blue hydrogen will increase the share of worldwide production (Tryggestad *et al.*, 2021). Forecasts from the BP Energy Outlook 2022 say that low-carbon hydrogen will account for 55 % in 2030 and 65 % in 2050 (BP Energy Outlook, 2022).

However, the challenges that must be tackled today are the high prices and the CO_2 emissions per produced tone of H_2. Multiple already existing conversion methods are “Steam Methane Reforming” (SMR), “Autothermal Reforming” (ATR), “Partial Oxidation” (POX) and “Electrolysis”. The efficiencies range between 65 - 80 % and the CO_2 emissions depend on the raw material used for the extraction. They range in the area of 9 kg CO_2 per kg H_2 for the SMR method, where methane is the primary raw material (Gasunie - Crossing borders in energy, 2022). Currently, SMR is the cheapest and most efficient way to produce hydrogen. Moreover, carbon capture methods can be used to reduce the emitted emissions. For instance, the ATR method limits the emissions to a minimal value, which can be compared to the SMR method. Other methods like POX use coal or fossil fuels to extract hydrogen, resulting in a doubled value of emissions per kg H_2.

The most promising method to produce hydrogen emission-free is electrolysis. Water is split up into oxygen and hydrogen with the help of electricity. Depending on the power source, the emissions vary. For the net-zero scenario, it is desired that only renewable energy sources like water, wind- and solar-related sources should be used. If this is the case, zero emissions will occur. Otherwise, with the actual energy mix, it will also produce an amount of 25 kg CO_2 per kg H_2. This method currently needs nine liters of water for one kg of hydrogen (Gasunie - Crossing borders in energy, 2022).

If one refers to the carbon intensity of the methods, they can be grouped into a color scheme. The different emissions levels are listed below:

- **Brown Hydrogen:** Coal and its gasification is used for the process, which results in massive CO_2 production (Saracco, 2021).
- **Grey Hydrogen:** The method uses natural gas as raw material in the SMR process and produces many emissions.
- **Blue Hydrogen:** Blue hydrogen will be one standard method in the next ten years until green hydrogen can be extensively manufactured. The energy used is non-renewable, but the CO_2 emissions are captured and stored.
- **Turquoise Hydrogen:** This process uses pyrolysis of methane and produces only a limited number of emissions.
- **Green Hydrogen:** The method which stands behind green hydrogen is water electrolysis. Green hydrogen is produced using electricity from renewable sources (e.g., wind, water, or solar power). Water is split up accordingly to the chemical reaction below, which does not emit CO_2 to the environment:

$$H_2O_{(liquid)} \rightarrow 2\,H_{2\,(gaseous)} + O_{2\,(gaseous)}$$

In 2019 the world's hydrogen production was at eight million tons, and nearly all of that was produced from fossil fuels, leading to CO_2 emissions of 830 million tons (Saracco, 2021). Figure 2 illustrates the difference between the grey, blue and green production methods of hydrogen.

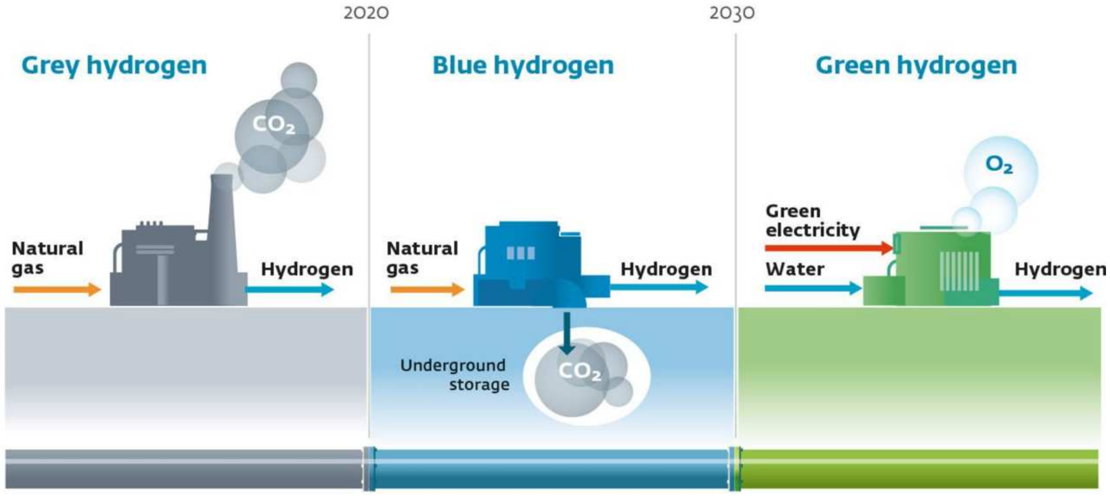

Figure 2: The different primary methods of producing hydrogen and the impact of CO_2 (Saracco, 2021).

The importance and status of implementing hydrogen in the current energy system are quite versatile all over the globe. Few countries are currently entirely committed to a national hydrogen strategy, e.g., Australia, Japan, or Germany. In the report of the World Energy Council (2020), which represents 90 % of the global gross domestic product (GDP), it was found that 20 countries showing 44 % of the GDP already passed a hydrogen strategy or are on the verge of doing so in the upcoming near-future. The national strategies differ in detail, representing the country's interests and industrial strengths. Nevertheless, overall, the main drivers of the national governments to pass hydrogen strategies were the reduction of greenhouse gases and the integration of hydrogen in renewable energy sources like wind and solar. In countries where already action happened, hydrogen is clearly recognized as an essential element of a decarbonized energy system, including securing the energy supply and economic growth. Especially in the European Union, green hydrogen is the top target. The market ramp-up will happen in three phases: market activation in the current decade, sustainable growth after 2030 and a large, well-established market by 2050 (World Energy Council, 2020).

Figure 3 compares three countries on three continents focusing on a national wide hydrogen strategy: Germany, Japan and Australia. The national goals of Germany and Japan are congruent, whereas the application fields differ entirely. On the one hand, Germany focuses on the industry and transport sector. On the other hand, Japan is concentrating, besides the transport sector, on the power generation and building sector. Both share the focus on the transport sector, whereas Germany focuses on transportation, which is hard to electrify, such as planes, ships and heavy-duty trucks and Japan focuses on passenger cars. The Japanese companies Toyota and even Honda are leading globally in the segment of fuel cell passenger cars. Due to country-specific circumstances, Germany has limited access to renewable energy potential, which cannot support green hydrogen creation. To meet the long-term demand for H_2 in Germany, imports of hydrogen will be necessary. Nevertheless, Germany wants to become one of the leading exporting hydrogen technology countries. In general, European countries with a strong focus on industry and close attention from governments aim to reduce GHG and mainly focus on the industry and transport sector.

Japan is considered the pioneer and one of the leading countries in hydrogen worldwide. The continuous governmental activity and support mainly drive this to finance hydrogen projects. Though hydrogen’s origin is until 2030 mainly produced from fossil fuels, from 2025 on, CCS technologies will be used to reduce the GHG manufacturing footprint. For comparison reasons, Australia will become a major global renewable and low-carbon hydrogen exporter by 2050. Australia has the conditions to cost-efficient produce the necessary amount of renewable energies, which will be needed to execute the electrolysis of the water to produce hydrogen. Even the industry, especially the steel industry, might be Australia’s top target to incorporate hydrogen. Furthermore, seasonal load balance and storage through hydrogen technologies in combination with renewable energy supply are crucial parts of Australia’s strategy and future (World Energy Council, 2020).

Furthermore, countries like Austria, Sweden and Canada are to be getting started producing national strategies for the usage of hydrogen and other countries like the USA, India and Brazil show only support for pilot and demonstration projects without aiming for national strategies nowadays (World Energy Council, 2020).

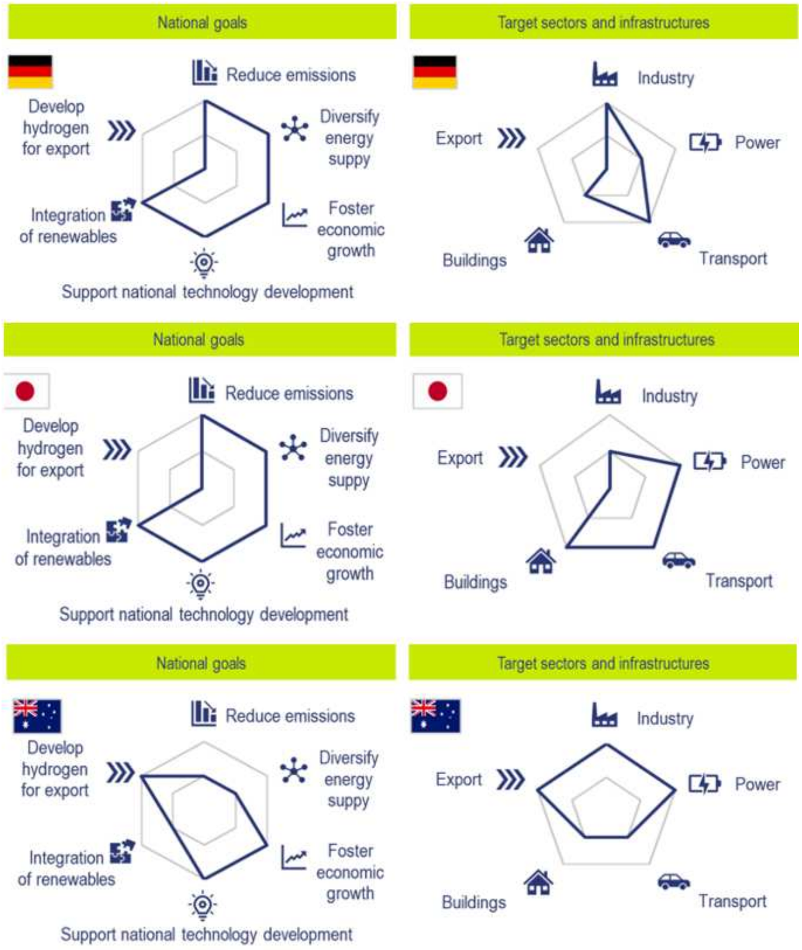

Figure 3: Comparison of the national hydrogen strategies of Germany, Japan and Australia (World Energy Council, 2020).

However, implementing hydrogen in the energy system might have advantages, but also negative rumors are associated with this topic. The cost and efficiency of the production process can be seen very critically. The cost of green hydrogen production is still too high compared to grey hydrogen produced from fossil fossils. Thus, only 0,1 % of worldwide hydrogen production is green and environmentally friendly (World Economic Forum, 2021). Furthermore, the efficiency of the supply chain of hydrogen is barely efficient. Approximately 30 - 35 % of the used energy is lost during electrolysis. Other processes, such as liquefying, can be an essential part of transporting hydrogen (transport via LNG ships) from cost-efficient locations, such as Australia, to the rest of the world. Further on, converting H_2 to other energy carriers, such as ammonium, will further lose 13 - 25 % of energy. Even the transport needs energy equal to a 10 - 12 % energy loss (World Economic Forum, 2021). The later retrieved percentage of electricity from the stored hydrogen results only in 30 % of efficiency (Wu, 2022). Another end-use of hydrogen in a fuel cell will result in another 40 - 50 % energy loss (World Economic Forum, 2021). Besides that, for instance, fuel cell cars need a condition of either 300 bar or 700 bar (depending on tank type) to store the H_2 in gaseous form, or it needs a temperature of -253 °C in a liquid state to store the H_2 onboard, which will cause safety concerns in the event of accidents (ADAC, 2022). Hence, these inefficiencies of the supply chain of hydrogen, usage and operation issues need to be tackled and advanced by the art of engineering.

1.2 Hydrogen properties

The critical point for safe and secure underground storage operations is the knowledge of the physical properties and the differences between hydrogen, carbon dioxide and methane. As Table 1 depicts, methane is eight times denser than hydrogen at 25 °C, which requires more pressure to store hydrogen gas than storing an equivalent amount of energy underground. Generally, the solubility when storing gases in depleted oil or gas reservoirs is evident to monitor. However, solubility during hydrogen storage operation will not be an issue due to the low Henry constants. Furthermore, hydrogen diffusivity increases between a temperature window of 10 - 35 °C (Engineering ToolBox, 2008).

The low molecular weight, lower viscosity and high diffusivity compared to methane can be a significant problem during operation and may cause hydrogen losses. Therefore, the geological structure needs a tight caprock and the operating equipment should be monitored constantly to avoid hydrogen-caused embrittlement, which might create leakages in the pipes and auxiliary equipment along the lifting path to the surface.

From the gravimetric point of view, hydrogen has roughly three times higher energy content than natural gas, with its main component CH_4 (Zivar, Kumar and Foroozesh, 2020). Converting CO_2 to CH_4 with H_2 can gain more energetically valuable gas, as the volumetric content of energy in hydrogen is low compared to methane (Zabranska and Pokorna, 2017). Table 1 indicates the physiochemical difference between hydrogen and methane.

Table 1: Physical properties of hydrogen and methane (Zabranska and Pokorna, 2017; Zivar, Kumar and Foroozesh, 2020).

Property	**Hydrogen** **H_2**	**Methane** **CH_4**
Molecular Weight	2,016 g/mol	16,043 g/mol
Density @ 25 °C and 1 atm	0,082 kg/m^3	0,657 kg/m^3
Viscosity @ 25 °C and 1 atm	$0{,}89\times10^{-4}$ Pa·s	$1{,}1\times10^{-5}$ Pa·s
Solubility in pure water @ 25 °C and 1 atm	$7{,}9\times10^{-4}$ mol·kgw^{-1} H_2 (g)	$1{,}4\times10^{-3}$ mol·kgw^{-1} CH_4 (g)
Normal Boiling Point	-253 °C	-165 °C
Critical Pressure	12,8 atm	45,79 atm
Critical Temperature	-239,95 °C	-82,3 °C
Heating Value	120 - 142 kJ/g	20,5 - 55,5 kJ/g
Diffusion in water @ 25 °C	$5{,}13\times10^{-9}$ m^2/s	$1{,}85\times10^{-9}$ m^2/s
Volumetric Content of Energy	10,88 MJ/m^3	36 MJ/m^3

Hydrogen can occur in three phases (solid, liquid and gas), as the phase diagram in Figure 4 depicts. It is of crucial importance to understand the temperature and pressure behavior when dealing with H_2. At low temperatures, hydrogen is in a solid state with a density of 70,6 kg/m^3 at -262 °C and a gaseous state at higher temperatures with a density of 0,0898 kg/m^3 (at 0 °C and 1 bar). The blue zone in the plot represents the liquid area of hydrogen, and the zone starts at the triple point and ends at the critical point. At the critical point, hydrogen shows a density of 70,8 kg/m^3 at -253 °C. At the ambient temperature of 25 °C (298,15 K), hydrogen is in the gas state (Züttel, 2004).

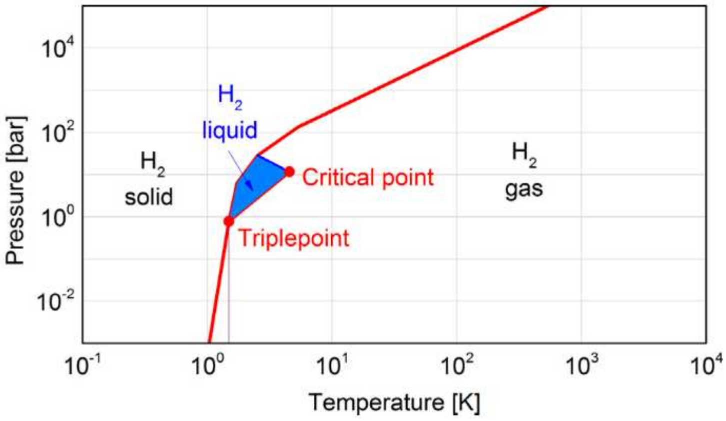

Figure 4: Hydrogen phase diagram. Liquid hydrogen only exists between the solid line and the line from the triple point at 21,2 K and the critical point 32 K (0 K=-273,15 °C) [adapted and modified, originally from (Züttel, 2004)].

Hydrogen faces a low volumetric energy density (0,003 kWh/l at 15 °C and 1 bar) compared to conventional liquid energy carriers, such as diesel or gasoline. Diesel has a volumetric energy density of about 10 kWh/l and a gravimetric energy density of 11,9 kWh/kg. This fact makes H_2 less favorable to the use of energy transport. Various options for efficient transport can be applied. For pipeline transportation, the hydrogen gas must be pressured up to 100 bar, which changes the energy density to 0,26 kWh_{LHV}/l (LHV=lower heating value). For road transport, the pressure must be increased further to 500 bar, which raises the volumetric density to 1,06 kWh_{LHV}/l. Due to the unfavorable compressibility factor of hydrogen, a pressure increase has a negligible effect on the volumetric energy density compared to methane. The reason why hydrogen is still transported over long distances is liquefication. Thus, it increases the energy density by a factor of 786, compared to the initial state, to 2,36 kWh_{LHV}/l.

1.3 Storage options in porous media

Generally, two types of geological structures can be considered. The first option is storage in the pore network of sandstone or carbonate reservoirs and the second alternative is cavern storage in a dense rock. Salt cavern storage has been done since the 1980's in Germany (Thomas and Gehle, 2000), but it is not considered as a porous media. Therefore, it is not addressed here in more detail. Different technical and safety requirements must be met depending on the type of underground storage and the stored medium. Essentially, cap rock tightness, which is complex to be monitored, creates a major challenge. Effective monitoring and identification of leakages and immediate interventions are crucial. Carefully selected materials might save frequent inspections and workover costs, especially in the wellbore, where due to limited accessibility, any operations are cost and time intensive. From the geological point of view, technical feasibility depends on the tightness of the cap rock, trapping capacity and properties of the stored gas, which need to be understood before operation. For instance, more carbon dioxide than hydrogen can be stored in the same underground facility due to its density, compressibility and solubility (Zivar, Kumar and Foroozesh, 2020).

1.3.1 Underground hydrogen storage

Hydrogen can be used as the storage medium in depleted gas or oil reservoirs, salt caverns and aquifers. If there is an energy demand, hydrogen can be withdrawn from the subsurface facility and used for whatever reason. Moreover, hydrogen has the advantage of its wide variety of usage, for instance, in the industry as feedstock, in traffic, especially in heavy-weight traffic as fuel, or as a source of electricity for grid balancing (Stolten *et al.*, 2020). In the past, methane storage, town gas storage and even CO_2 storages were standard, but most recently, H_2 storage has risen. The concept of UHS balances the temporary mismatch between supply and demand in a mainly renewable energy resource-driven energy system. The storage capacity and the security of storing hydrogen underground are much higher than surface alternatives because a mixture of hydrogen and oxygen is explosive at almost any concentration at the surface. Another advantage of UHS is the costs, which are lower than any other alternatives (Zivar, Kumar and Foroozesh, 2020).

The petroleum industry has already gained experience in the underground storage of natural gas or even carbon dioxide. Many parallels gained from experiences in the O&G industry can be drawn, which allow screening of suitable storage sites and storage techniques, including monitoring strategies and economic evaluation standards (Zivar, Kumar and Foroozesh, 2020). Nevertheless, besides the storage operation's similarities, the storage media's physiochemical properties are completely different, which must result in high awareness regarding monitoring, leakages and the different chemical affinities of the storing medium. From a reservoir engineering aspect, a propagating gas phase experiences effects like fingering through the denser phase and gravity segregation leading to overriding. As a result, the mineralogy and herewith also, the hydraulic properties of the host rock can be changed. Also, the influence of microbes can reduce the hydraulic properties (porosity and permeability) due to biomass accumulations.

Different types and options of underground storage are available. The medium can be stored in the porous medium of geological structures, such as depleted gas or oil reservoirs, aquifers, coal seams, or the cavities of salt caverns. The significant benefits of already-used and well-identified geological structures are the proven tightness and integrity of the cap rock and even the in-place surface and subsurface equipment. Therefore, depleted hydrocarbon reservoirs are a viable solution for underground storage operations. The performance of underground hydrogen storage is dictated by the rock properties of the geological structure, the fluid properties and the rock-fluid interactions (Pan *et al.*, 2021).

The appropriate storage reservoir should cover a porous and permeable formation capped by an impermeable seal. In the reservoir, the storage gas is simultaneously flowing and co-existing with the formation brine, which is always part of depleted gas or oil reservoirs (Pan *et al.*, 2021). Besides that, the reservoir heterogeneity should be as low as possible to ensure interactions throughout the entire reservoir are enabled. A reported problem with operating hydrogen storage is fingering, which can be reduced by using steeply dipping structures and thicker formations to reduce the effect of this phenomenon. However, before converting a depleted oil or gas reservoir into a storage facility, a comprehensive study of each new storage option, including laboratory work, is essential to understand the chemical reactions in the subsurface.

For operation reasons, cushion gas is inevitable and will increase the storage's performance and efficiency. Cushion gas can be nitrogen or even methane. It is considered the volume of the gas, which stays permanently in the reservoir to maintain the pressure and the required flow rate during the injection and withdrawal cycles. On the one hand, cushion gas can reduce hydrogen loss during the production and withdrawal periods due to pressure maintenance, reducing the negative effect of gravity segregation (Kanaani, Sedaee and Asadian-Pakfar, 2022). Further loss of hydrogen can be a natural result of chemical, biological and microbial reactions. On the other hand, cushion gas can be produced in a mixture of hydrogen. Therefore, suitable separation facilities must be used to segregate the phases.

Hydrogen has been stored since 1972 in salt caverns at Teesside in the UK and several salt caverns in the USA. In the USA, it started on the US Gulf Coast in Texas in 1983 and the experience of storing hydrogen on those sites has proven that it can be safely stored for a long period (Tarkowski, 2019; Zivar, Kumar and Foroozesh, 2020). Teesside stored one million m^3 consisting of a mixture of 95 % H_2 and 3 - 4 % CO_2 at a depth of 400 meters and a pressure of 50 bar. Nearby industries use the stored hydrogen to produce ammonium and methanol. The salt cavern at the Gulf Coast in Texas, named Spindletop, is shaped like a cylinder with a diameter of 49 meters and a height of 300 meters. The cavern is located at 1340 meters in depth and has a working condition of 68 - 202 bar (Zivar, Kumar and Foroozesh, 2020). This structure can contain 30 million m^3 of hydrogen and is directly connected to the pipeline network, which serves the petrochemical industry in Texas and Louisiana (Tarkowski, 2019).

Furthermore, underground hydrogen storage sites in aquifers are reported in Ketzin (Germany), Beynes (France), which operates additionally with natural gas and Lobodice (Czech Republic). The purity of the stored hydrogen is decreased compared to the salt cavern storage type, ranging between 50 - 62 % H_2 in a shallow depth of 200 - 430 meters. Only working conditions from the sites in Lobodice are reported, which are 90 bar and a temperature of 34 °C. Two additional sites for stored H_2 in depleted gas reservoirs are named: Diadema in Argentina and the "Underground Sun Storage" project in Austria. Both facilities operate with 10 % of hydrogen purity. In contrast, Argentina's site faces a condition of 10 bar at 50 °C at a depth of 600 meters and the Austrian facility works at 78 bar at 40 °C at 1000 meters depth (Zivar, Kumar and Foroozesh, 2020).

1.3.2 Carbon, capture and storage

Carbon, capture and storage will be an inevitable part of fighting climate change by cutting-off emissions in the midterm. Indeed, the site selection is quite similar to UHS, but two main characteristics are different: the physical properties of the media and the storage strategy. Regarding the properties of the gases, a higher quantity of carbon dioxide than hydrogen can be stored in the same storage volume. Solid properties like effective porosity and absolute permeability are almost equal to UHS. Fluid properties, such as density and viscosity, differ entirely between CO_2 and H_2. Therefore, the solid-fluid interactions, in the form of contact angle, capillary pressure, relative permeability, mobility ratio and chemical reactions, are different (Pan *et al.*, 2021). CCS aims to operate in the long-term, to permanently remove CO_2 from the environment or at least for hundreds of years with the phenomenon of mineral trapping (Metz, Davidson and De, 2005). This process is also known as the sequestration of CO_2. The storage of CO_2 is not cyclic and no withdrawal phase is needed. The UHS strategy is cyclic, consisting of an injection and a withdrawal phase. These cycles should serve the volatile demand of the energy market. Moreover, sufficient storage of energy can act as a buffer stock to regionally regulate energy prices in volatile periods.

1.3.3 Underground conversion – Power-to-Gas

The reservoir environment with moderate to high-pressure regimes, increased temperature and high brine salinities promotes and controls the presence of microbes and trace elements, which can catalytically interact with hydrogen. This may lead to inefficient operations and an unwanted side-effect for hydrogen storage. In the concept of Power-to-Gas, these reactions are instrumentalized to produce methane. A consortium of archaea cultures is fed by hydrogen and carbon dioxide, which produce methane and water. This chemical reaction is called methanogenesis and the optimal conditions for this reaction range from 50 to 90 bar and 30 to 90 °C. The exogenous reaction of methanogenesis, including Gibbs free energy, is pictured below (Zabranska and Pokorna, 2017):

$$CO_2 + 4\ H_2 \rightarrow CH_4 + 2\ H_2O,\ \Delta G^{\circ} = -130{,}7\ kJ/mol$$

Several factors, such as pH value, water activity, or reservoir permeability, influence the presence and activity of microbes. Microbes acquire energy via oxidation and require an electron donor, like molecular H_2, by simultaneously reducing an electron acceptor, a carbon source. Microbes use CO_2 and H_2 to grow. Within the cells of the bacteria, specific enzymes, named hydrogenases, controls the reaction of splitting H_2 into protons and electrons, which can be used to store energy chemically. This energy is responsible, for instance, for the consumption and the binding of the CO_2 molecules.

1.4 Pilot projects

As already discussed, Power-to-Gas will make it possible to produce green gas out of renewable energy through natural processes over 1000 meters below the surface, where natural gas was created millions of years ago. The aim is to store energy for seasonal energy fluctuations. Energy surplus from renewable sources in the summer should be transferred into the winter, where it is required.

In Austria, pilot projects are currently being executed. The projects are named “Underground Sun Conversion” and “Underground Sun Storage 2030”. The pilot facility is the Lehen storage in the molasse basin in Upper Austria, a depleted gas reservoir. The sandstone prospect shows a working condition of 78 bar and 40 °C at a 1000 meters depth (Dopffel, Jansen and Gerritse, 2020). Hydrogen purity is 10 %, but steps will increase this value during the project’s lifetime.

The principal concept of the “Underground Sun Conversion” is depicted in Figure 5. Water electrolysis fueled by renewable energies creates green hydrogen. The process of using solar or wind energy to split up water is called Power-to-Gas. The carbon dioxide is captured from the air or industrial applications. Then H_2 and CO_2 are injected into a suitable depleted gas reservoir for conversion into methane by the natural process of the archaea and storage reasons. H_2 and CO_2 feed the microorganisms. The product is natural, climate-neutral green gas, which can be stored in this reservoir, withdrawn when needed, and transported to the industry or private customers via the existing pipeline system. Moreover, water is also a product of this chemical reaction. The water can be used for further actions on the surface after cleaning. The Austrian company RAG holds an international patent for this process called hydrogenotrophic methanogenesis (RAG Austria AG, 2021).

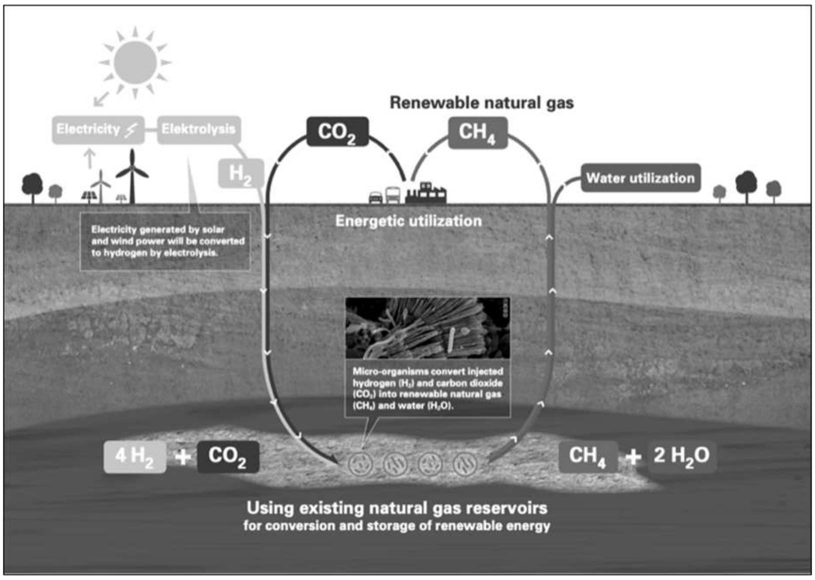

Figure 5: Pilot Project Underground Sun Conversion – Sustainable Carbon Cycle [modified and adapted, originally from (RAG Austria AG, 2021)].

The “Underground Sun Storage 2030” is the second project that aims to fuel the vision of a hydrogen energy system and therefore focus on hydrogen storage. As stated by the company side: “Storing hydrogen seasonally and in large volumes is the best basis for a hydrogen economy” (RAG Austria AG, 2021). The central concept remains, as pictured in Figure 6. In this case, hydrogen is injected and withdrawn. The stored energy, in the form of gaseous H_2, can be directly utilized by the industry or injected into the gas grid. Furthermore, due to its wide variety of usage, hydrogen storage can be an essential part of the future transport sector as syn-fuel.

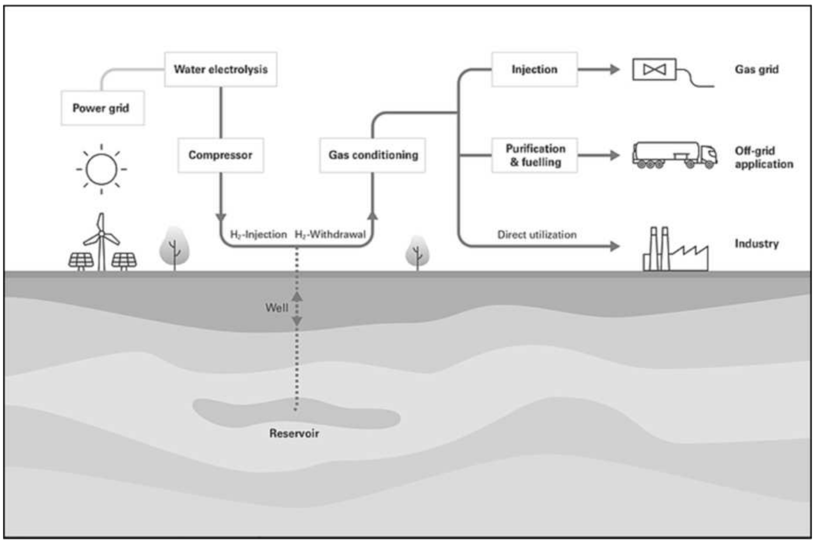

Figure 6: Pilot Project Underground Sun Storage [modified and adapted, originally from (RAG Austria AG, 2021)(RAG Austria AG, 2021)].

1.5 Background and context

This master thesis, including the simulations, is based on the dissertation of Dr. Hassannayebi, “An assessment of underground hydrogen storage: Transport, geochemistry, and bioactivity” and on the master thesis of DI Jammernegg, “The influence of microbial growth on hydraulic properties of subsurface gas storage and in-situ gas conversion”, which is also the continuation of the work of Dr. Hassannayebi. The doctoral thesis was further based on two well-known industrial project series from the Austrian gas storage company RAG: “Underground Sun Conversion” (www.underground-sun-conversion.at) and “Underground Sun Storage” (www.underground-sun-storage.at). The leading research of the “Underground Sun Storage” project is to store large volumes of hydrogen in depleted gas reservoirs. Whereas the project “Underground Sun Conversion” focuses on the technology of Power-to-Gas, which considers the production of green gas in the reservoir with the help of microorganisms.

Both previous publications conducted experiments via the usage of micro model chips. The biomass accumulation and growth were captured over time to quantify the change in hydraulic properties in the model. Moreover, the focus was on investigating the internal permeability and porosity of the biomass. The experiments were recorded via high-resolution time-lapse images and investigated to study this phenomenon and its impact on hydraulic properties. The gained images were segmented based on their grey values assuming varying biomass permeability.

The master thesis of DI Jammernegg was to study the influence of microbial growth on the hydraulic properties in the pore network and to investigate the types of possible mass transfer within the biomass, diffusion and advection. Furthermore, both publications used a numerical model to survey biomass behavior thoroughly. The utilized microbial culture during the experiments was lactobacillus casei (L. Casei). The study reveals a remaining base permeability in the porous medium resulting from forming of preferential flow paths and the intra-biomass permeability.

1.6 Scope and objectives

This master thesis is part of a “BioPore” research project conducted with several universities and an industrial partner. This thesis aims to study the growth characteristics of methanogenic species under anaerobic, saturated flowing conditions and perform direct numerical simulations in the pore network resembling a digital twin. The microbes used in the project are methanobacterium formicicum (M. Formicicum). The objective of this study was to improve the numerical model by introducing the original depth and curvature of the micro model. Furthermore, the study focused on the implemented microbe’s growth and accumulation characteristics and the permeability-porosity relationship. Moreover, the changes in velocity and the stress distributions over time were investigated. In the end, a heterogeneity analyses were performed to investigate the degree of heterogeneity of the micro model (MM) to find a smaller representative volume for the total domain (TD).

1.7 Overview of the master thesis

Chapter 1 briefly overview a hydrogen energy system and the possible ways to produce hydrogen. Furthermore, different storage options in porous media are reviewed and current executed pilot projects are discussed.

Chapter 2 reviews basic literature and definitions of one-phase and multi-phase flow theories, such as porosity and permeability. Further on, concepts of microbial growth, microbial transport and clogging mechanisms in porous media are part of the chapter.

Chapter 3 describes the principal experimental workflow of the master thesis. The experimental setup is pictured and the journey from the raw image to the simulation input is discussed in detail. Furthermore, the numerical simulator inputs are reviewed and summarized.

Chapter 4 represents the result and discussion section, achieved via the enhanced numerical model simulations. The hydraulic properties, porosity and permeability, were estimated in the simulation domain. Furthermore, velocity and stress fields are extracted and investigated in detail via a histogram analysis.

Chapter 5 states the conclusion and suggests some future work.

Chapter 2

Literature Review

This chapter addresses fundamental concepts to understand the physical processes for underground storage in porous media. The concepts apply to two-phase arrangements, which are essential for underground storage applications. Although the covered experiments in this thesis are conducted in a one-phase system, multiphase systems are explained for enhanced understanding. Furthermore, other relevant aspects of underground hydrogen storage, like microbial activity and biomass accumulation, are also reviewed.

2.1 Multiphase system

The following section briefly describes general definitions of fundamental reservoir engineering aspects and the two-phase flow inside a porous medium. Multiphase flow characterizes the system, where at least two separate phases are present. To describe these systems entirely, capillary pressure and relative permeability, in addition to porosity and permeability, are necessary. Usually, each phase has its chemical composition and physical properties. Therefore, the definition of a wetting and a non-wetting phase can be introduced. Furthermore, an interfacial tension exists on the interface of those phases, which is responsible for the capillary pressure.

2.1.1 Porosity

The porosity of a rock is the storage capacity or the pore volume, which fluids can occupy. The porosity ϕ of a rock is the void space in a medium and is defined as a fraction or as a percentage of the total bulk volume (Equation 1):

$$\phi = \frac{pore\ volume}{bulk\ volume} [\%] \qquad (1)$$

where ϕ is the porosity and the pore volume represents the free pores of the rock sample. The bulk volume covers the entire rock volume, including fluids.

Two types of porosities are distinguished: absolute and effective porosity. The absolute porosity is the total pore space in a rock and in contrast, the effective porosity counts only the interconnected pore spaces. Figure 7 illustrates the interaction between porosity and permeability. Permeability is only given when the pores are connected. Typical porosity values for a loosely packed sandstone are 35 - 40 %, and a more consolidated sandstone just shows 20 - 35 %, respectively (Nagib, 2021).

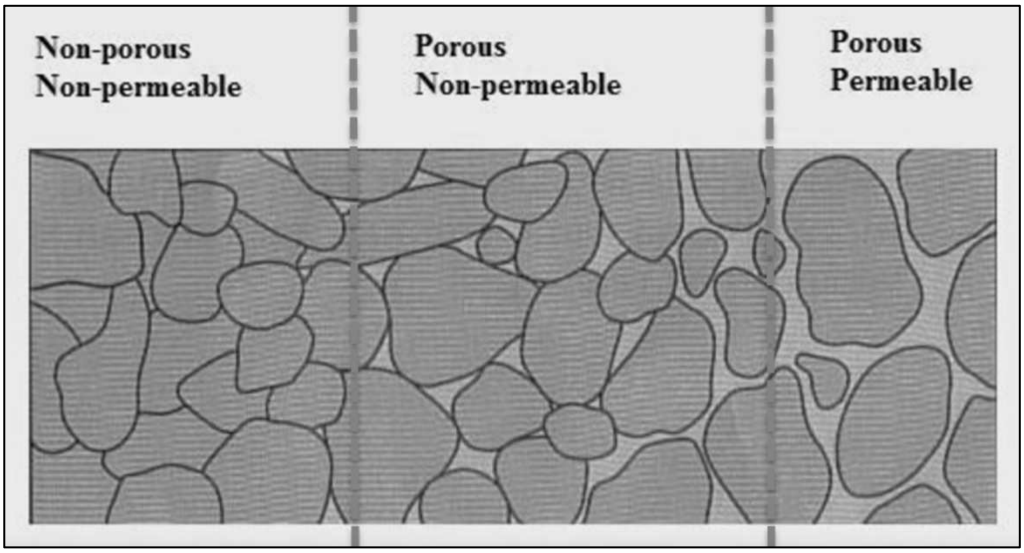

Figure 7: Illustration of permeability and porosity (Joseferd and Mahmood, 2015).

2.1.2 Permeability

The permeability is, together with the porosity, an inseparable pair for determining the rock's storage and producibility, respectively. The permeability K measures a porous media's ability to transmit or conduct a fluid (Nagib, 2021). Three types of permeabilities are used: absolute, effective and relative permeability. The absolute permeability K represents the hydraulic conductivity of a medium at 100 % saturation. Effective permeability is defined as the ability of a fluid to flow in the presence of another (e.g., k_{oil}, k_{gas}, and k_{water}). When more than one fluid phase is flowing, the concept of relative permeability is used. It is the ratio of effective k to an absolute K for each fluid. For instance, like $k_{ro}=k_o/K$, $k_{rg}=k_g/K$ or $k_{rw}=k_w/K$ (Nagib, 2021). Where k_{rx} describes the relative permeability and k_x the effective permeability for a medium x (e.g., oil, gas, or water) and K is the absolute permeability, representing 100 % saturation of one fluid.

Darcy’s law is one of the well-known equations used to describe a fluid’s flow through a porous medium. Equation 2 represents Darcy’s equation in a one-phase system, but it can even be adapted to multiphase flow:

$$u = -\frac{k}{\mu}(\nabla \mathrm{P} + \rho g) \qquad (2)$$

where u represents the velocity, k the permeability and μ the viscosity. ∇P illustrates the pressure gradient and indicates the direction of flow. Additionally, the gravitational term ρg is included in Equation 2.

Figure 8 illustrates the flow through a core plug, with the parameters essential for Darcy’s law. The geometry of the core plug is given with the area A (cm^3) and the length L of the tube (cm). The liquid stream through the pipe is the flow rate q (cm^3/s). The fluid is characterized by the permeability K (D) and the dynamic viscosity μ (cP). The pressure drop is captured via the pressure gradient dP/dx (atm/cm) between the inlet and outlet of the sample.

The unit of permeability is Darcy. “One darcy is the permeability of a 1 cm long sample with a cross-sectional area of 1 cm^2 when a pressure difference of 1 dyne/cm^2 between the ends of the sample causes a fluid with a dynamic viscosity of 1 poise to flow at a rate of 1 cm^3/s.” (Glover, Zadjali and Frew, 2006). The Darcy unit is sparsely used in practical geological use because it is too large. More common is the scale for millidarcy (mD).

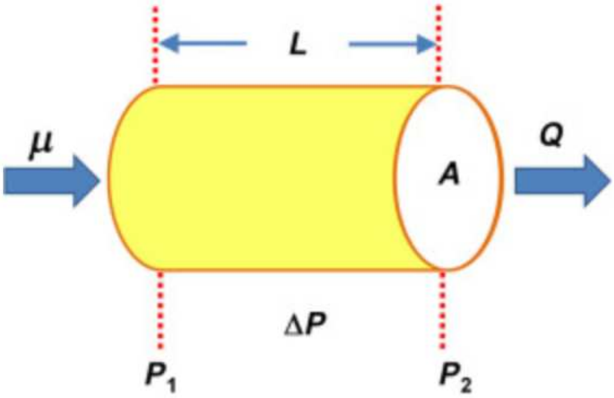

Figure 8: Schematic picture illustrating Darcy’s law’s parameters for incompressible flow through a core plug (McPhee and Zubizarreta, 2015).

In a multiphase system, Darcy’s law can be expanded by the concept of relative permeability. The pore space may be filled not only with one fluid phase but contain two or three phases. Relative permeability is a function of fluid saturation and the wetting state of the system and relative permeability controls the separated fluid flow of different phases (Rose, 1949).

As Figure 9 depicts, these pores are filled with water and gas. Both fluids flow at different rates and the permeabilities depend on rock properties, fluid properties and saturations. Hence, one fluid's relative permeability decreases as that fluid's saturation decreases. Furthermore, a specific threshold value of saturation of any fluid needs to be present before the fluid moves. The relative endpoint permeabilities on each side of the graph mark this area. In this case, the water phase is immobile until the saturation S_{wir} is reached and this zone is called the irreducible water saturation (unmovable water). The opposite area is the irreducible gas saturation (S_{gr}), which is very narrow in this case. The phase permeability curves for these systems are often biased to one side of the graph.

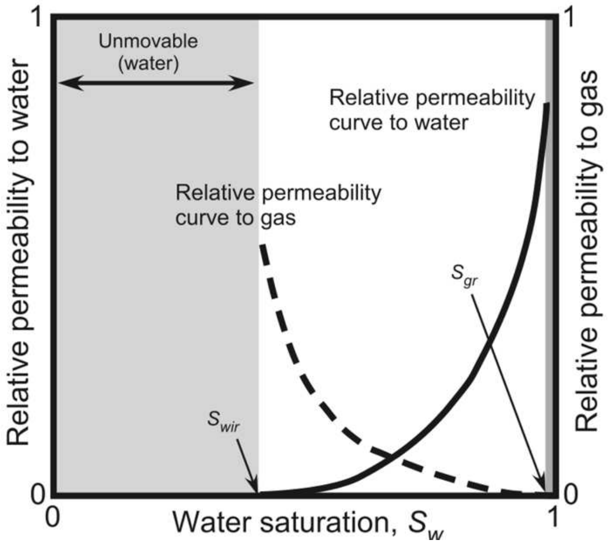

Figure 9: Relative permeability curves for an water/gas system [adapted and modified, originally from (Kogure et al.*, 2011)].*

2.1.3 Capillary pressure

Capillary pressure (P_c) is the pressure difference at the interface between two immiscible fluids in the pores or the reservoir rock. It is the amount of pressure required by the non-wetting phase to displace the wetting phase. The capillary pressure controls the fluid distribution in the reservoir and the displacement of one fluid can be either aided or opposed by capillary pressure. The capillary pressure is defined as the following Equation 3:

$$P_c = P_{nw} - P_w \qquad (3)$$

where P_c is the capillary pressure and P_{nw} and P_w are the pressure values for the non-wetting and wetting phases, respectively. For instance, the non-wetting phase can be gas and the wetting phase can be water. In this example, the capillary pressure will be calculated as the pressure difference between gas and water.

When it comes to two immiscible fluids in a narrow cylinder, the fluids will form a meniscus. Laplace suggested the following relation to describe this phenomenon (Equation 4):

$$P_c = \sigma(\frac{1}{R_1} + \frac{1}{R_2}) \qquad (4)$$

where σ is the interfacial tension (N/m) between the two phases, wetting and non-wetting. R_1 and R_2 are the radii of the interface curvature. If this formula gets a further simplification (R_1=R_2=r) in the form of a spherical droplet, the Young-Laplace equation (Equation 5) can be established:

$$P_c = \frac{2\sigma cos\Theta}{r} \qquad (5)$$

where Θ is the wetting angle (°), σ is the interfacial tension (N/m) between the two phases, wetting and non-wetting and r is the radius of the pore throat.

Capillary pressure has immense importance in the petroleum industry. The concept has been used to evaluate the rock qualities, pore size distributions and fluid saturations in a reservoir. The idea of capillary pressure is clear: the entry capillary pressure must be exceeded by the non-wetting phase to enter the pore space.

Moreover, capillary pressure is vital for the tightness of the sealing layers of the storage reservoir. If the capillary entry pressure of the sealing layer will not be surpassed, then the stored fluid or gas will not flow through the cap rock and the storage option is tight and safe for operation. Usually, shales have orders of magnitude higher entry pressures than good quality sandstone rock for the same fluid system.

The concept of capillary pressure and relative permeability can be linked via the Brooks-Corey correlation (Corey and Brooks, 1964). If the capillary curves of primary drainage are approximated, then the Brooks-Corey model, as in Equations 6 and 7 depicted, can be used:

$$S_e = (\frac{P_e}{P_c})^{\lambda}, (P_c \geq P_e) \qquad (6)$$

$$S_e = \frac{S - S_r}{1 - S_r} \qquad (7)$$

where S_e represents the effective saturation and S_r is the irreducible saturation, the amount of liquid the medium with a given pore structure can retain. S displays the absolute saturation, whereas S_e is a linear function of saturation S and is related to the residual saturation S_r. P_e (Pa) denotes the entry pressure and P_c is the actual capillary pressure (Pa). The entry pressure is the minimum pressure required to act, for instance, on a liquid phase to invade the pore. λ is the scaling parameter representing the pore size distribution index (Lu *et al.*, 2020).

2.1.4 Wettability

Wettability is an essential parameter in evaluating a reservoir due to its influence on fluid saturation and capillary pressure. The concept of wettability is only applicable if two phases are present. "Wettability describes the preference of a solid surface to be in contact with one fluid rather than another" (Abdallah *et al.*, 2007). A surface is called water-wet when the water tends to cover it, and the counterpart is oil-wet, where the surface prefers to be in contact with the oil phase (Anderson, 1986). The state is called neutral wet when the media prefers neither oil nor water wet. The angle between the liquid-solid surface is measured and represents the contact angle (Θ).

Two wetting states are distinguished: wetting and non-wetting or water-wet and oil-wet. Wetting states have an angle smaller than 90° and non-wetting conditions have an angle larger than 90°. In general, the contact angle will be measured in the denser phase. Low values of Θ will achieve a complete spreading of the droplet on the surface, as shown in Figure 10 for the water-wet case. Higher values tend to repel the droplet, like in Figure 10 in the oil-wet case.

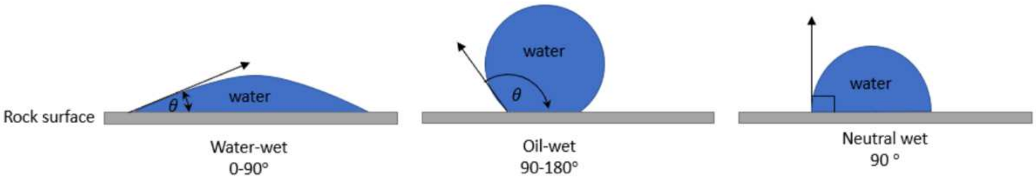

Figure 10: Contact angles and wettability states (Sandnes, 2020).

If the system changes to a gas-liquid system, the method used to measure the contact angle is the captive bubble method. This method is executed due to the density differences between a liquid and a gas. A syringe inserts the gas into a liquid-filled box sealed by a solid, where the contact angle can be measured via a microscope. Figure 11 depicts the different wetting cases and the contact angles using the captive bubble method.

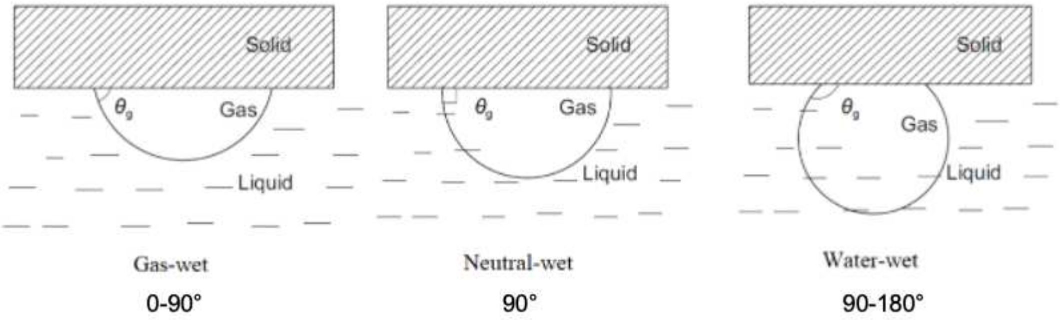

Figure 11: Contact angles and wettability in a gas-liquid system using the captive bubble method [adapted and modified, originally from (Jiang, Li and Zhang, 2013)].

2.1.5 Drainage and imbibition

Regarding displacement processes in porous media, the original wettability and the capillary pressure play a significant role. Hysteresis curves are used to display the change in a system. Figure 12 shows the two processes, primary drainage and imbibition, which leads to a hysteresis curve after frequent occurrences.

Drainage describes the displacement in a porous medium of a wetting phase, e.g., water-filled pores, by a non-wetting phase, e.g., oil or gas. The vice-versa process is imbibition. Imbibition is when the wetting phase saturation increases and the non-wetting phase saturation decreases (Nagib, 2021). Both processes differ in their path. The endpoint for drainage and the start point for the imbibition stays the same, but the endpoint for the imbibition is different. This inconsistency and the various paths of P_c are known as capillary hysteresis.

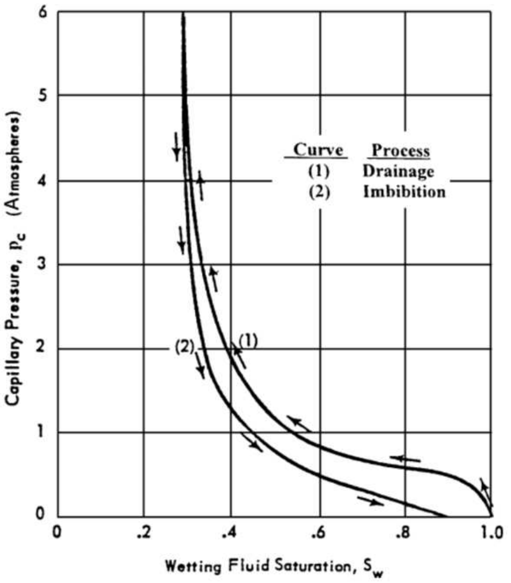

Figure 12: Primary drainage (1) and imbibition (2) curves in a porous medium. The starting point for drainage is S_w=1 and the endpoint for imbibition is S_w=0,9 (Dr. Jawad et al.*, 2017).*

Drainage and imbibition are categorized into different groups depending on when the process occurs. Usually, an aquifer holds fresh water or a brine system. When the first medium enters the porous medium, for instance, gas, the drainage is called primary drainage. Primary drainages happened millions of years ago in the reservoir when the migration of hydrocarbons was released from the source rock to be trapped in the reservoir rock. Further, reinjections of gas into the reservoir are called secondary drainage or tertiary drainage. For storage operations, it is vital to determine the initial state of drainage before secondary and tertiary drainage happens (Tweheyo, Talukdar and Torsæter, 2001). The same convention applies to the imbibition cycle hysteresis.

2.1.6 Trapping mechanisms

Not only for enhanced oil recovery methods but also for hydrogen or carbon dioxide storage operations, the understanding of trappings mechanisms is vital. For instance, in the subsurface storage of hydrogen, hydrogen will be lost due to capillary-induced actions or to dissolution and solubility in water or brine. But it must be mentioned that the dissolution of hydrogen in water is very low. The native fluid is brine for aquifers, while for depleted oil and gas reservoirs, it is a mixture of oil, gas and brine. Additionally, different trapping mechanisms are desirable for carbon sequestration, which is a permanent storage operation. Long-term trapping includes structural and stratigraphic trapping, residual CO_2 trapping, solubility trapping and mineral trapping. Mineral trapping has the highest security in the CO_2 storage mechanisms and will last for 100 years and more (Metz, Davidson and De, 2005).

It is essential to understand these trapping mechanisms to increase storage efficiency, identify leakage potentials, and develop mitigation actions. The snap-off effect is one trapping mechanism that mainly relies on interfacial tension and capillary pressure. If gas or oil moves inside a water-wet system, the interfacial forces form a droplet and separate it from the moving phase. First, the capillary pressure has to be high enough for the gas or oil to invade the pore, then the P_c has to drop by a factor of two, for the water to retake the pore at a later stage (Rossen, 2000). The pore can only be invaded if the capillary pressure exceeds the capillary entry pressure P_c^e of the pore throat. Thus, this can be simplified to Equation 8 for a water-wet system ($\Theta = 0°$) with a cylindrical pore:

$$P_c^e = \frac{2\sigma}{r} \qquad (8)$$

where σ is the gas-water interfacial tension (N/m) and r is the radius of the pore throat (μm). The unit of the capillary entry pressure is N/m^2 or Pa. This equation states that pore throats with smaller radii require a more significant pressure to invade the pore. For more prominent pores, the capillary pressure is minor. Figure 13 sketches a snap-off process in a water-wet system for a trapped non-wetting phase (oil).

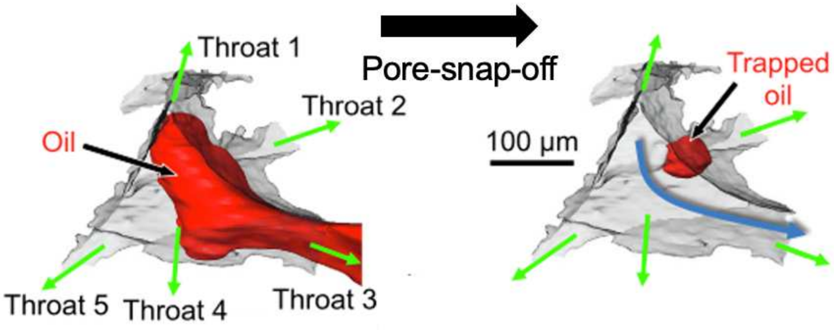

Figure 13: Sketch of the snap-off for trapping of a non-wetting phase (oil) [adapted and modified, originally from (Singh et al.*, 2021)].*

Figure 14 depicts a capillary-trapped hydrogen bubble during water injection. As already discussed, a bubble in a pore needs to overcome a high capillary entry pressure to move through a narrow pore throat, because with lower radii of the throat, the capillary entry pressure increases. This means that during water imbibition, such kinds of pores are bypassed and pores invaded with lower entry pressures. The hydrogen bubble is immobile and trapped by a capillary forced phenomenon. The capillary pressures P_{c1} and P_{c2} prevent the H_2 bubble from getting pushed through the pores by the viscous force F_v. Hence, the mathematical statement can be formed: $P_{c1} + P_{c2} > F_v$, where P_{c2} is larger than P_{c1} due to the smaller radius of the pore neck. In theory, a force exists parallel to the F_v, but this is neglectable due to the large radius (Van der Hart, 2021).

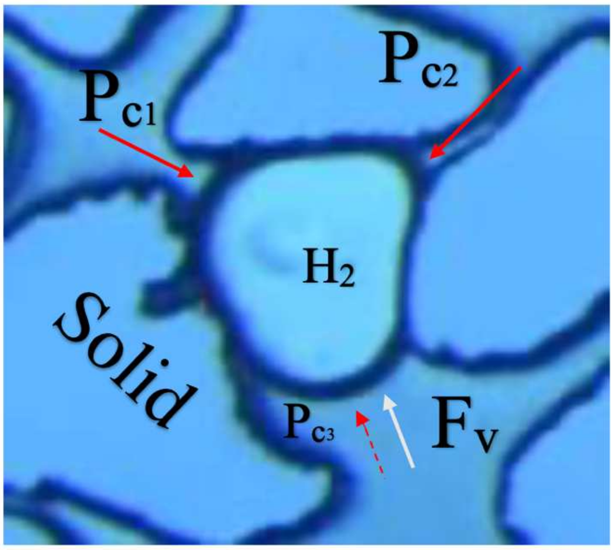

Figure 14: Hydrogen bubble - capillary trapped during water injection. Capillary forces (red arrows) confront the viscous forces (white arrows). $P_{c1}+P_{c2} > F_v$ *and* $P_{c2} > P_{c1} >> P_{c3}$ *(Van der Hart, 2021).*

2.2 Underground hydrogen storage

The following should describe the phenomenon relevant to underground hydrogen storage and basic concepts of relevant microbiological processes, which should explain the behavior and transport of microbes in the subsurface. Important aspects related to hydrogen underground storage, as well as the side-effect of methanation, are discussed. During underground hydrogen storage, microbial metabolic reactions can potentially convert carbon dioxide to methane.

Due to microbial presence and their advective transport, reservoir porosity and permeability changes can be observed. Hence, hydrodynamic properties are mainly influenced by biomass accumulation. The process of pore blocking is often referred to as bioclogging, which might be a favorable effect in water flooding operations, where the blockage of high permeable zones is desired to avoid any bypassing of the injected fluid and enhance the sweeping efficiency in hydrocarbon-bearing zones. This phenomenon might show non-desirable consequences for underground energy storage (Hassannayebi, 2019).

The macroscopic behavior on the continuum scale of the injected fluids is not the topic of this thesis, like fingering or gravity over-/under-ride. The thesis focuses on the pore scale effects and the microscopic behavior of microbes.

2.2.1 Microbes in the subsurface

In the past, archaea were part of bacteria nomenclature and were called archaebacteria, but during history, two categories were divided due to different evolution stories. Nevertheless, in this thesis, as simplification, the terms "bacteria" and "archaea" are identical. Microbial communities are complex systems shaped by their local microenvironment (Aufrecht *et al.*, 2019).

Usually, bacteria cannot be seen without any optical support. The typical size of one microbial cell is between 0,2 - 1,5 μm in diameter and 3 - 5 μm in length (Ananthanarayan and Paniker, 2008). The structural appearance of archaea can be of any shape, but the most known forms are rod, sphere and spiral shapes. They might appear in single, pairs, groups, clusters, or cubes. The schematic composition of a bacteria cell consists of an outer cell membrane, the cell wall, which is filled with cytoplasm and a nuclear body (Ananthanarayan and Paniker, 2008).

The growth of microbes is signified by the increasing cell concentration, where the number or the mass of cells has increased. According to Mohanta, Dutta and Goel (2017), cell concentration over time is the most common quantitative property of bacterial growth. Binary fission is responsible for cell replication and the growth of microbial cultures. If the cell size reaches a significant threshold, the cell, including the nuclear cell, starts to divide into two daughter cells. The time required for binary fission is also known as doubling time. The population of microorganisms grows exponentially, which can reach an enormous concentration in just a short period. However, the growth is limited to the supply of nutrients or the accumulation of toxic elements (Ananthanarayan and Paniker, 2008). In the case of UHS, the nutrient is supplied by injecting H_2 and CO_2. Reservoir heterogeneity might influence nutrient accessibility in the subsurface. Moreover, significant growth and the conversion reaction might be limited to a reduced part of the reservoir.

Suitable methods to investigate the growth of bacterial cultures are time-series experiments called batch culture or continuous culture experiments. These experiments are executed in a closed system at fixed conditions (temperature, pressure, etc.) (Nikolaev, 2020). The standard method to display the growth of the culture is to plot the bacteria count as a function of time. Some characteristic patterns with typically four stages of growth are identified. Figure 15 shows an arbitrary growth curve of a bacterial culture.

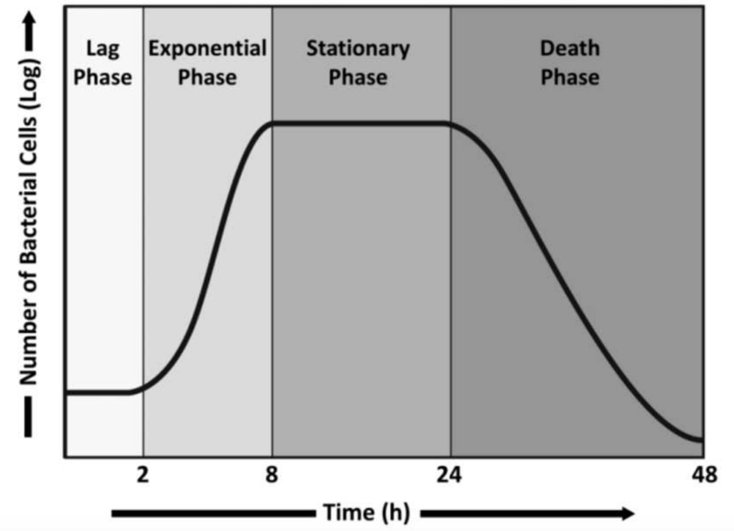

Figure 15: Bacterial growth curve indicating four phases (Garrison and Huigens, 2016).

The “Lag Phase” is the period just after the start of the experiment. The nutrients are already in place and the cells are consuming them, but no increase in the bacterial number is taking place. The cells are rising in size, but no replications occur. The constant number can also be explained by adapting to the new environment and conditions (Parker *et al.*, 2018). The “Exponential or Log Phase” follows the “Lag Phase”. The archaea start to duplicate and the number of cells grows exponentially. In the “Stationary Phase”, the growth rate is nearly equal to the death rate. Thus, a plateau of the living cells is formed. The last phase is the “Death or Decline Phase”. The number of cells is decreasing due to faster microbial cell death than replication leading to a net loss in biomass. This can be mainly explained by the exhaustion of nutrition and the accumulation of toxic elements. The decline rate is also exponential but usually slightly lower than the growth rate (Maier, Pepper and Gerba, 2009). The dead cells lyse or break open and spill their inner content into the environment, which can be used from the living cells as a nutrient source. This supports the survival of microbes in harsh conditions without a permanent nutrition supply (Bailey, 2021).

2.2.2 Microbial reactions

The most relevant chemical reactions executed by microbes in the subsurface are depicted in Table 2 below.

Table 2: Most relevant chemical reactions (including the enthalpies of the reactions) in the subsurface (Hagemann, 2018; Szyk and Czernia, 2022).

Name	Chemical equation	Enthalpy of reaction
Methanogenesis	$CO_2 + 4\,H_2 \rightarrow CH_4 + 2\,H_2O$	$\Delta H^{\circ} = -252{,}97\ kJ/mol$
Acetogenesis	$2\,CO_2 + 4\,H_2 \rightarrow CH_3COOH + 2\,H_2O$	$\Delta H^{\circ} = -269{,}16\ kJ/mol$
Sulphate-reduction	$SO_4^{2-} + 5\,H_2 \rightarrow H_2S + 4\,H_2O$	$\Delta H^{\circ} = -253{,}70\ kJ/mol$
Iron (III)-reduction	$3\,Fe_2^{III}O_3 + H_2 \rightarrow 2\,Fe_3^{II}O_4 + H_2O$	$\Delta H^{\circ} = -50{,}03\ kJ/mol$

2.2.3 Microbial metabolism

The driving mechanism for the metabolic reaction is the gain in energy to foster survival and growth. The desired energy comes from the metabolic reduction of hydrogen within the microbes. Different metabolisms can be distinguished: chemoheterotroph, chemoautotroph, photoautotroph and photoheterotroph. The metabolic types differ in the source of energy supply and carbon sources. Energy sources can be sunlight, or in the more specific case, in the subsurface, the redox reaction of chemicals. Available carbon sources like carbon dioxide are injected or already in place. The carbon source can be of organic or inorganic matter, as is the case for CO_2 (Maier, Pepper and Gerba, 2009).

Two types of bacteria metabolism are distinguished: respiratory and constructive metabolism (nutrition). During respiration, hydrogen and carbon dioxide are consumed, but the biomass is not changing in mass. Furthermore, in the methanogenic reaction, respiration is responsible for transforming reactants into products of the reaction, which are methane and water. Biomass production follows a catabolic reaction, which differs in how external carbon is converted into organic cell material. The chemical outcome of the reaction is the same as for the respiratory metabolism, which is methane and water (Panfilov, 2016).

The chemical reaction below demonstrates an anabolic reaction, which simultaneously occurs with the catabolic reaction of methanogenesis. The molecular formula of biomass was assumed to be $C_5H_7O_2N$ and NH_3 is ammonia (Batstone *et al.*, 2002):

$$10\ H_2 + 5\ CO_2 + NH_3 \rightarrow C_5H_7O_2N + 8\ H_2O$$

Microorganisms and their metabolisms under nearly every condition are hugely important to humans. Especially in the food, fermentation and medicine industry, microorganism plays a non-replaceable role. For instance, some convert milk into useful dairy products such as yogurt and cheese. The microbial culture L. Casei, used in the named previous experimental approaches, is responsible in a mixture of microbes for the ripening of Swiss cheese and its characteristic taste and large gas bubbles (Kadner and Rogers, 2022).

2.2.4 Hydrogen migration

If a hydrogen phase gets trapped through capillary forces and is immobile, it creates an interface with the water phase. At this contact point between the two phases, the migration of H_2 into the water phase will occur until an equilibrium at constant conditions is reached (Buchgraber, Kovscek and Castanier, 2012). The molecular diffusion of hydrogen controls the mass transfer under no-flow conditions into water. Diffusion is the movement from a higher concentration towards a minor concentration of a medium, in this case, hydrogen, from the gas-water interface to the liquid phase. The probability of diffusion and molecular transport is linked to the random motion of molecules, which is controlled by temperature (Meyers, 2002). Unlike advection, the diffusion flux is independent of velocity and orientation. Several studies state that diffusion is the primary process for nutrient transport within the biomass under the assumption of impermeable biomass. Advection regarding nutrient supply within biomass is often neglected. Molecular diffusion is described by Fick's first law (Equation 9):

$$J = -D\frac{\partial\varphi}{\partial x} \qquad (9)$$

where, J is the diffusion flux ($kg/(m^2 \cdot s)$), D is the diffusion coefficient in area per time (m^2/s), φ is the concentration of solute per volume (kg/m^3) and x is the position in space (m).

Performed experiments from Van der Hart (2021) featured following outcomes. Suppose the concentration of hydrogen increases in the water phase and the gradient of molecular diffusion is decreased. During imbibition, hydrogen is in contact with new fresh water and dissolution occurs via advection in each phase. At this time, the pressure of the injected phase is increased and dissolution through advection is partially reversible when the pressure is reduced again. The pressure reduces if the imbibition is finished and gas-water equilibrium is established or the already dissolved hydrogen gas in the water phase returns to its initial state and breaks out of the solution as free gas (Van der Hart, 2021).

Advection is the motion of particles along the bulk flow and is caused by pressure gradients. As Figure 16 depicts, the velocity vector of the advection is controlled by the pressure gradient. P_1 is larger than P_2 and, therefore, is fluid A displacing fluid B from left to right. Advection is a component transport mechanism faster than diffusion.

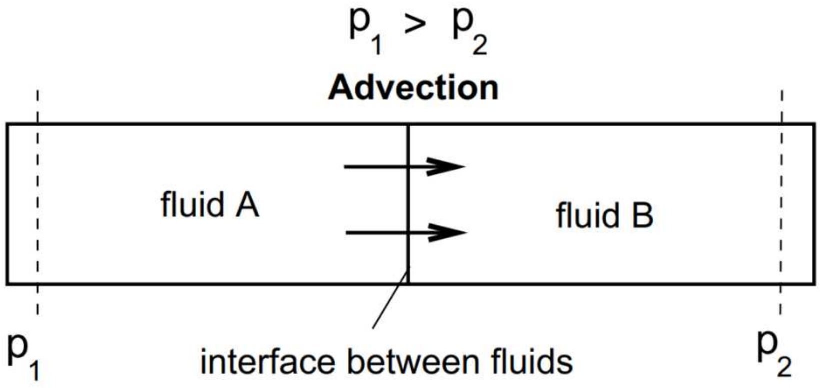

Figure 16: Schematic illustration of advection in multiphase flow (Bielinski, 2007).

The relation between diffusion and advection can be quantified via a dimensionless number called the Peclet number (Pe). The Pe number is the advective term divided by the diffusivity coefficient, as can be seen in Equation 10:

$$Pe = \frac{ul}{D} \qquad (10)$$

where u is the local flow velocity (m/s), l is the characteristic length (m) and D is the relevant diffusion coefficient (m^2/s).

Before hydrogen can be transported and transferred to the microbes, it must be dissolved in the liquid phase. Solubility is defined as the maximum amount of a substance (solute) that will dissolve in a given amount of solvent at a specified temperature and pressure (Bhavishya, 2017). Additional factors influencing solubility is the presence of other solutes competing in the dissolution process. For the specific hydrogen-water reaction, hydrogen acts as the solute and water as the solvent. Hydrogen is hardly soluble in water under standard conditions since water is polar and hydrogen is non-polar, which aggravates the bond (USP, 2015). The solubility of H_2 and H_2O increases with pressure and decreases with higher temperature and salinity in the solvent phase (The Engineering Toolbox, 2021).

In underground hydrogen storage operations, hydrogen trapping and dissolution are not desirable and reduce the efficiency of the storage. The aim is to keep these reactions at a minimum rate. All the above chemical and physical reactions are connected. First, drainage happens. Second, the imbibition occurs and the continuous hydrogen phase gets disconnected. H_2-bubbles can get trapped by capillary forces. These trapped bubbles cannot be back-produced under these conditions and will get bypassed. After the hydrogen gets trapped, dissolution at the H_2-H_2O interface occurs. Whereas the capillary number N_c is decisive, whether diffusion, advection, or both simultaneously occur in the hydrogen dissolution. The hydrogen stays dissolved in the water phase until the pressure is reduced again. As mentioned, higher pressures force an increased solubility, which will further result in a faster dissolution and higher depletion rates of H_2 (Van der Hart, 2021).

2.2.5 Microbial movement

Every microbe exerts a specific type of movement. For instance, plankton is known as the most active bacteria regarding its movement. However, different processes emerge when it comes to the more complex movement of biofilms. Advective transport describes the movement in a flow field and rheotaxis describes the orientation according to the flow direction to reduce energy (Panfilov, 2018). Biofilms are usually formed in zones with low fluid velocity, having a higher chance of settling. Attached biomass is more probably to detach if the fluid flow is speeding up, thereby, microbial cells are removed from the biofilm layer and redistributed. Once the organic tissue reaches a location of decreased velocities, also called the stagnation zone, it attaches again (Hassannayebi, 2019). The transportation of microbes through the pore network is comparable to a filtration process, also known as the physical straining of microorganisms via pore throats. Physical straining is a function of microbial size, shape, and pore network properties (Hassannayebi, 2019).

2.2.6 Biofilms

In this thesis, the formulation “biofilm” is used for an accumulation of microbial cells and metabolic products with a current flow between the cells rather than within or through the cells. According to Panfilov (2018), three main forms of the existence of microorganisms are crucial. First, it can appear as “Plankton”, a collective microorganism that lives in large volumes of water without the ability to swim against the current. Second, microorganisms living in the water on the gas and water interface are called “Neuston”. Third, organisms, which occur mostly on solid interfaces in the water, e.g., on the pore surface in the underground storage facility, are called “Biofilm”. More accurately, the entire cluster of microbial cells and produced UHS (EPS), together with trapped organic and inorganic materials, are termed the “Biofilm” (Cunningham, 1991).

A biofilm is formed if cells of microbes attach to a surface in natural environments. They can be formed on nearly every surface and environment, regardless of whether the environment is saturated or undersaturated. Whereas distinct factors must be given to let the microbes grow.

Biofilms are the predominant form of microbial life, especially in porous media (Gerlach and Cunningham, 2010).

Microbial biofilm formation on surfaces is a complex phenomenon consisting of several events. Biofilms can be part of nature, as well as engineered systems. They prefer to live in aqueous environments and form via biomass attachment and growth. The biofilm life cycle is shown in Figure 17. First, the transport and attachment of microbial cells at an interface occur. At this stage, the cells are reversible attached and can be easily removed. Second, during the growth process, EPS is produced to improve the cohesive strength of the biofilm bonding. The EPS material also acts as a nutrient reservoir. The fully developed biofilm is in its maturation phase. Third, microbial cells can leave the bonding due to cell death, which can be caused by insufficient nutrient supply. Another reason for cell dispersal can be the varying velocities and flow conditions caused by microbial growth (Barraud, 2007; Gerlach and Cunningham, 2010). Higher velocities in the porous network will increase the shear forces, leading to increased cell detachment. Free-swimming cells in the system can be reattached to a surface to form new biofilms, which closes the biofilm life cycle. According to Yao, Habibian and O'Melia (1971), these mechanisms and kinetics during the attachment process within porous media can be described via the colloid filtration theory.

Figure 17: Biofilm life cycle: (i) Reversible attachment of cells to a surface. (ii) Secretion of adhesins and EPS that result in irreversible attachment of the biofilm and the start of the proliferation of the cell (Including biofilm maturation). (iii) Cell death and dispersal of single cells (Barraud, 2007).

The accumulation of microbes is not entirely determined by the growth and decay but is also influenced by detachment and (re-)attachment of biomass (Thullner, 2008). Detachment is the continuous separation of a small number of microbial cells driven by shear forces and sloughing is the detachment of large biomass portions (Clement *et al.*, 1997). Further studies found that critical shear stress must be exceeded to begin the detachment process.

The structure of biofilms is predominately heterogeneous and may contain voids. Thus, it can be said that biofilms are not entirely impermeable. Some researchers state that biomass has internal permeability and porosity, which implies that biomass films can be treated as porous media. As a result, biomass may contain enormous amounts of dynamic and static water, which will be as high as 97 % of water (Ahmad and Husain, 2017).

A punch of factors influences the growth of the biofilms if it is attached to the surface. According to Gerlach and Cunningham (2010), five crucial parameters are noteworthy:

1. Sufficient nutrition
2. Sufficient energy
3. Proper geochemical conditions (pH, temperature, pressure, liquid ionic strength, etc.)
4. Absence of inhibitors (waste products and toxic materials)
5. Hydrodynamics, which influences the solute mass transport (e.g., advection)

It is visible that the availability of nutrition mainly drives microbial growth. The biofilm rate was directly linked to the available nutrient concentration. If the biofilm thickness increases through accumulation and growth, the path for diffusion is also rising. Hence, the nutrient concentration decreases towards the surface. Biofilm accumulation results in narrower pore throats, leading to higher flow velocities in the pores (Hassannayebi *et al.*, 2021).

Furthermore, the solid surface’s characteristic, e.g., the roughness, plays another crucial role. The higher the roughness of the surface, the higher the activity of the cells to form biofilms (Characklis, McFeters and Marshall, 1990).

2.2.7 Bioclogging

As discussed, systems with a large surface area to volume ratio, as is the case for porous media, provide an excellent environment for microorganisms. The effects of the growth and accumulation of microbial biomass can lead to a reduction of pore space and a decrease in permeability. Bioclogging is often referred to as the decline in hydraulic conductivity (Hassannayebi, 2019). The clogging is driven by the buildup of microbial biomass, which consists of cell growth and cellular polymeric substances. The EPS forms a protecting structure increasing the stability of the accumulated microbes. It has been observed that higher shear forces acting on the biofilms will enhance the production of polysaccharides and cell proteins, resulting in a more balanced and increased biofilm growth (Tay, Liu and Liu, 2001). Besides that, also pore sizes play a significant role in bioclogging. To avoid serious plugging issues, the pore entry diameter must be at least two times larger than the diameter of the microbial cells (Davis and Updegraff, 1954).

Underground clogging can be divided into three subcategories: physical, chemical and biological clogging. Physical clogging can result from clay swelling, migration of fines, accumulation of organic or inorganic materials, or invasion of drilling fluid in porous media. It is mainly described by physical processes and is the prevailing clogging type in porous media, but bioclogging takes over the predominant role after some time. Therefore, at later stages in microbial growth, the categories of physical and biological clogging are merging, such as biomass accumulation and growth can plug pore throats. In comparison, chemical clogging is related to precipitations of salts in the form of sulfates, carbonates and phosphates, etc. (Hassannayebi, 2019). Another type, a combination of physical and chemical clogging, is physiochemical clogging, which can be divided into filtration and straining. Filtration occurs when microbes are removed from the solution and attached to grains or preexisting biofilms, like when a coffee suspension is poured through a filter. Therefore, surface irregularities have a noticeable effect, increasing the filtration process. Moreover, straining is a mechanical/physical trapping process when pore throats are too narrow for microbes to flow (Cunningham, 1991).

Bioclogging is controlled by the flow velocity and other conditions like surface roughness and nutrient supply. The probability of clogging is highest in two shear stress regimes. First, pores with meager shear rates were caused by constant and uniform velocity distributions across the pore throats. Second is a region with low velocity, paired with a common variation in shear stresses. The shear stress rate is a time differential of velocity. Thus, low shear rates can occur when there is a constant velocity distribution across the pore.

2.2.8 Effect on hydraulic properties in porous media

Good knowledge of hydraulic properties is inevitable for performing forecasts and predictions for underground hydrogen storage. Effects of changed hydraulic properties due to microbial actions were first observed at the beginning of the 19th century (Slichter, 1905). Excessive enrichment of biomass results in a reduction of porosity and permeability. Both properties are related via a power law, hence a reduction in permeability is very sensitive to a decrease in porosity (Hommel, Coltmann and Class, 2018). Therefore, the permeability-porosity relationship is a decisive factor in all reactive transport problems. The biofilm thickness can reach a equilibrium state, where the porosity and permeability stabilize and remain constant until the operating conditions are changed (Cunningham, 1991).

Biofilms are changing their structure over time to improve substrate transport and stability. Biofilms are not accumulated homogenous in the pore network. Instead, they face various spatial and temporal settlements, where low permeable areas and flow channels are favorable places to form continuous biofilms (Thullner, 2008).

The environment limits microbe’s growth if critical shear stress is reached. Shear stress is a concept of solid mechanics: shearing forces push one part of a body in one specific direction and the opposite part in another. For instance, in Figure 18, the flow velocity is represented by the tangential force F, which tends to deform the solid cube with an area A on top. In the underground, the solid cube acts as biomass accumulation.

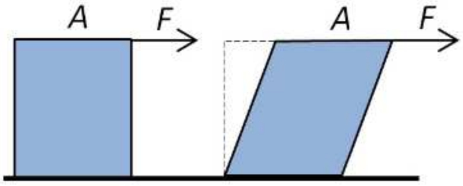

Figure 18: Schematic representation of shear stress (Roux et al.*, 2020).*

The shear stress is formulated as the ratio of a force acting on an area, which implies a pressure (Equation 11):

$$\tau = \frac{F}{A} \qquad (11)$$

where τ is the shear stress (Pa), F is the tangential force (N) and A represents an area (m^2).

The shear stress influences the spatial distribution of biomass. In a constant flux system, narrower pore throats lead to increased flow velocities and, consequently, higher shear stresses (Thullner, 2008). The shear stress magnitude can control the removal of microbial cells from a biofilm or even the erosion of larger packs of biomass. According to Stewart's and Fogler's (2001) visual observations, the more significant removal of biomass packages must be considered a frequent but singular event in the pore network. Areas, which are protected and reveal low shear stresses, have relatively thicker and rougher biomass accumulations (Gerlach and Cunningham, 2010).

Moreover, biomass permeability also plays a significant role in the shear stress distribution and hence, the erosion and detachment of microbial cells. “The sensitivity of flow fields to biomass permeability directly affected the spatial distribution of where transport is dominated by advection or diffusion” (Hassannayebi, 2019).

Zones of higher shear stresses will result in thin, smooth and homogenous layers (Gerlach and Cunningham, 2010). Moreover, organic cells with higher adhesion forces tend to foster bioclogging, as these microbial cells are washed out less quickly. Therefore, they can reach higher accumulations in a porous medium (Vandevivere and Baveye, 1992). These structural changes will affect the velocity distributions and hence the nutrient supply in the porous medium.

Besides bulk and effective porosity, internal biomass porosity has a considerable impact on nutrient supply, according to Gerlach and Cunningham (2010). Furthermore, the porosity-permeability relationship is influenced by the location of biomass accumulation. If the biomass occupies the inner side of a large pore or fracture, the porosity might not change dramatically and therefore, permeability stays nearly unaffected. Vice versa, when biomass accumulates at pore throats or other spots with possibility to plug pores, the influence on the flow behavior will significantly increase. Thus, also minor porosity changes can considerably impact the permeability due to the cut-off of pore sections (Gerlach and Cunningham, 2010).

The primary affected hydrodynamic property in biomass accumulation is permeability and even minor changes in the system will vary the permeable values. Due to the clogging or plugging of available pore throats, biofilms can tremendously impact permeability. Several studies reported a maximal permeability reduction of three orders of magnitude (Gerlach and Cunningham, 2010).

Chapter 3

Experimental Part

This chapter deals with the experimental and numerical setup of this master thesis. The experimental setup is part of a current research project on subsurface methanation, which is a continuation of Dr. Hassannayebi's work. This section describes significant process steps from raw imaging over simulation settings to simulation evaluation.

The experimental setup aims to study microbial growth under optimal conditions and analyze the hydraulic property changes over time, which might be crucial for understanding underground gas storage processes. A two-step approach was used to perform the experiments: bacterial suspension flooding (one-phase system) and nutrient flooding (two-phase system). Images in the first phase, representing a one-phase system, were used to extract specific information about the growth characteristics and accumulation of the selected culture, M. formicicum. The relevant properties were collected through a pseudo-2D model under distinct laboratory conditions. The experiments were carried out to illustrate underground gas storage conditions on the microscale and investigate the microbial growth over time.

Several parameters can be withdrawn from the "Digital twin" approach. Direct numerical simulations based on experimental outcomes allow us to verify the developed numerical model and investigate the influence of biomass accumulation on the porosity-permeability relationship. Moreover, the visualization of the spatial distribution of biomass in the micro model gives insights into possible arrangements in the underground. Velocity and shear stress data can be extracted for more detailed analysis and to investigate the changes in a velocity and stress histogram.

3.1 Experimental setup

The laboratory experiments were based on a microfluidic approach. High-resolution time-lapse imaging was used for biomass visualization in the porous medium. During the experiment, pressure sensors controlled the relative and absolute pressure, which allowed us to combine the information and investigate the correlation between porosity-permeability reduction and biomass increase. The experimental setup consists of a microfluidic system (1) apparatus in combination with a high-end microscope including a camera (2) to execute the experiments under anaerobic, two-phase flow conditions. A digital camera continuously took high-resolution images to capture any changes on the pore scale coming from biomass accumulation in space and time. The images were recorded with an exposure time of 1 millisecond (ms) and a pixel-size of 1,8 μm.

The pressure is monitored via a differential pressure sensor (3) between the inlet and outlet of the model. The gases are injected into the micro model (MM) via a syringe pump (4) at constant rates. The gas comes from the gas infrastructure (5) consisting of a nutrient (red gas bottle) and inert gas (green gas bottle), such as nitrogen. Furthermore, a heating jacket was used to keep the temperature constant at 37 °C during the experiment. Figure 19 represents the experimental construction, including the numbering of the individual components.

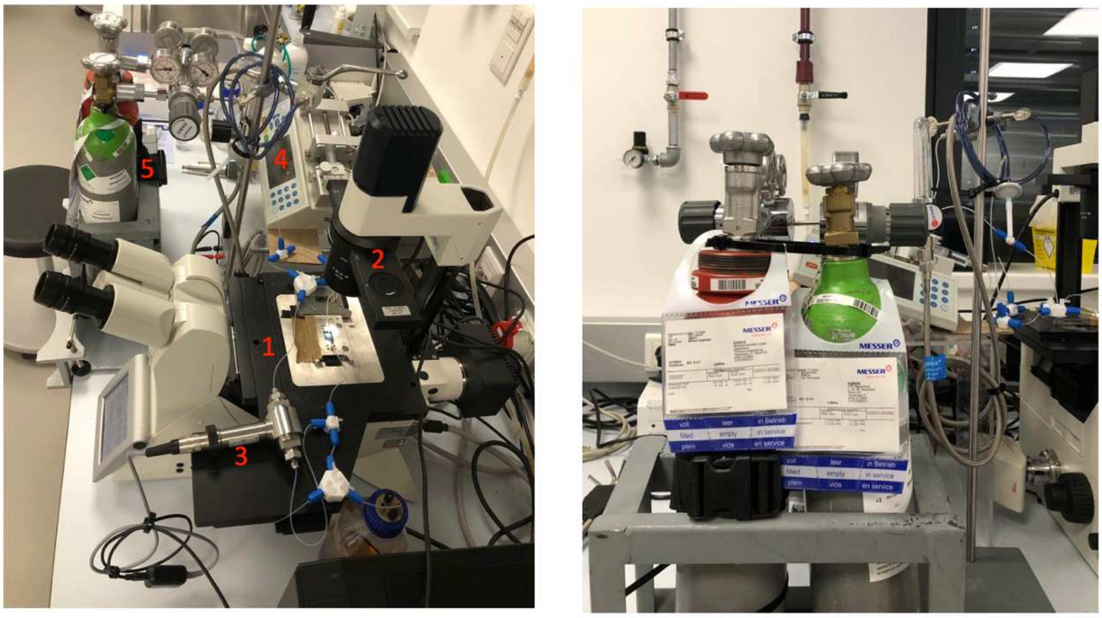

Figure 19: Left: The experimental setup consisting of the micro model (1), microscope including camera (2), fluid network (3), syringe pumps (4) and gas infrastructure (5) for anaerobic experiments at the department of Reservoir Engineering at the Montanuniversity Leoben. Right: Detailed view of the gas infrastructure: inert gas or nitrogen (green gas bottle) and nutrient gas (red gas bottle).

The affordable availability of application-tailored microchips with etched flow patterns introduced new options to investigate hydrodynamic characteristics on the pore scale (Karimifard *et al.*, 2021). The MM matrix in the experiment resembles an arbitrary pore network and enables the observation of microbial growth in porous media. The microchip is made of thin borosilicate glass manufactured by an etching process with hydrofluoric acid and a fitting top glass for coverage. This MM mimics an arbitrary reservoir rock with specific properties, such as a porosity of 57 % and a permeability of 2,5 D. The etching depth is 20 μm and the total domain size is 2 x 1 cm. The chip also covers branched paths at the inlet and outlet. As a result of the etching process in manufacturing, a rounded grain structure is achieved. Figure 20 shows a curved structure in the depth profile, which plays a crucial role in the simulation settings. Furthermore, the figure shows a region of interest (ROI), where pores (white area) and grains (grey area) are illustrated.

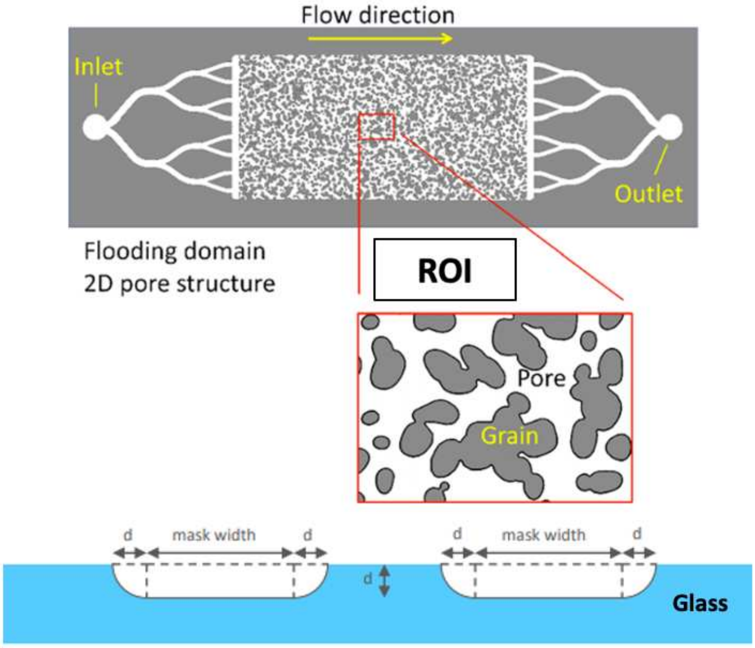

Figure 20: Top: pore structure including inlet and outlet paths of the microfluidic chip. Bottom: lateral depth profile of the microchips [adapted and modified, originally from (Micronit B.V., 2020)].

The used microchip sizes and properties in the experimental process are summarized in Table 3.

Table 3: Property summary of the microfluidic chip (Micronit B.V., 2020).

Specification	***Value***
Domain Size	20 × 10 mm
Channel Height	20 μm
Pore Volume	2,3 μl
Porosity	57 %
Permeability	2,5 D

3.1.1 Experimental workflow

The experiments were conducted under saturated flow conditions. First, nitrogen gas is injected to displace air from the system and create an anaerobic environment. A two-step approach was used to perform the experiments: bacterial suspension flooding (one-phase system) and nutrient flooding (two-phase system). After the flushing and cleaning with inert gas, the microbes are injected via the syringe pump in a step called suspension flooding. The microorganisms utilized are M. formicicum, a hydrogenotrophic methanogenic culture. The accumulation and growth process of the bacterial cells takes place within the domain and after approximately 72 hours, the nutrient gas is injected to enhance the microbial growth (nutrient flooding). Two experiment series were executed with different injection rates, 0,2 ml/h and 0,05 ml/h, respectively. A combination of hydrogen and carbon dioxide in an argon mixture represents the nutrient gas collocation. This phase, representing a two-phase system, aims to investigate the possible methane yield, which will not be further addressed in the scope of this work.

During the experiment, the differential pressure across the domain is recorded. After reaching constant pressure, an image of the total domain is taken to determine the saturation of the phases. A steady-state condition can be assumed when the fluid saturation is constant, combined with a constant differential pressure response. This procedure is repeated for different injection ratios of gas. In the end, gas samples will be captured, analyzed with analytical methods and compared with the mixture before injection to quantify the conversion efficiency and the claimed time horizon.

Both numerical simulations and imaging determine the porosity of the domain. The permeability can also be simulated or directly calculated from the experimental setup from the differential pressure records. Hereby the pressure is recorded at different flow rates. The slope of the pressure vs. flow rate relationship is inverse proportional to permeability and can be calculated using Darcy's law. During the experiments, a pressure rise from biomass accumulations can be captured. Significant pressure spikes were observed and indicated the flow of a dense suspension of biomass and water in the domain. This can be described as a sudden filtration event.

3.2 Image processing and segmentation

The recorded images need further steps before they can be embedded in the simulator. Two software programs, ImageJ and Ilastik, were used to crop and binarize the image and segment the images, respectively. ImageJ (Fiji®) is a Java-based image processing open-source freeware developed at the National Institutes of Health and the Laboratory for Optical and Computational Instrumentation (LOCI) at the University of Wisconsin (U.S. Department of Health & Human Services, 2021). Ilastik is an AI-based, user-friendly tool for interactive image classification and segmentation. It is built as a modular software framework, which currently has workflows for automated (supervised) pixel- and object-level classification, automated and semi-automated object tracking, semi-automated segmentation and object counting without detection (Berg *et al.*, 2019).

Steps of image cropping, stacking and segmentation contain potential error sources, which must be kept at a minimum. The experimental setup delivers raw images cropped to the correct size. Figure 21 depicts a cropped section from a raw image including biomass accumulation (brown-colored). Images of a complete time series can deviate from its predecessor and successor images. Therefore, ImageJ is used to stack all images from one experimental time series to enable the creation of one uniform mask of grains and to correct lens effects (uneven illumination effects). Before the mask can be fitted, the raw images (RGB images) must be converted via a grey scale to an 8-bit image. The grey-scale value of the biomass is determined by comparisons of several histograms of different timesteps. Then the uniform mask can be fitted and aligned with the stacked images. Afterwards, the images can be unstacked again.

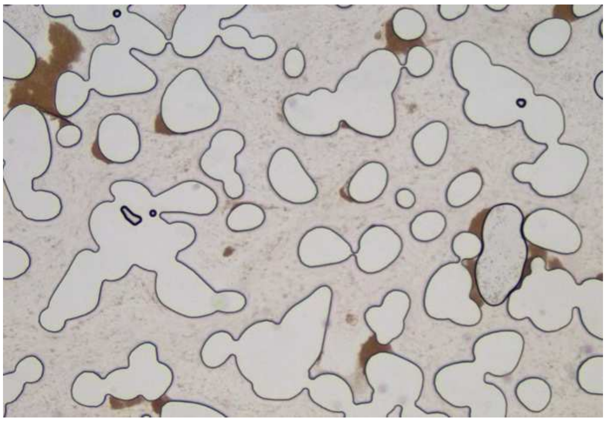

Figure 21: Image of the digital camera of the experimental setup representing a raw image. Pores, grains, and biomass can be captured.

Segmentation of the images is done using Ilastik. The images are thresholded based on their gray values in grains, pores and biomass. The pores, grains and biomass are precisely differentiated via a machine learning algorithm. Furthermore, artifacts in the images can be cleaned up with this software and the images are ready for use in the numerical simulator. Figure 22 shows a region of interest (ROI) for the conversion from the raw image to the simulation input.

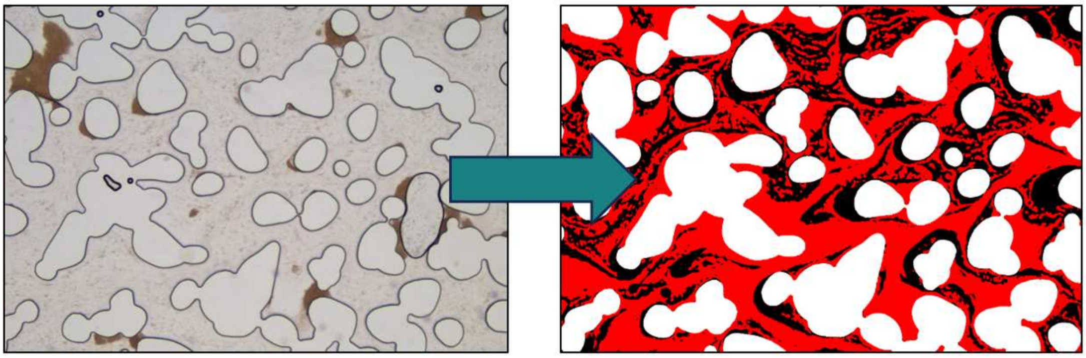

Figure 22: Schematic illustration of the image processing. Left: raw image (original image). Right: simulation input – segmented image (final image). Images were converted to 8-bit, the mask of grains was removed and finally, the images were thresholded based on their grey values.

Figure 23 visualizes the TD as an input for the numerical simulator. The left picture shows an empty domain (ED) without biomass, and the flow direction is from left to right. In comparison, the right picture depicts the last timestep of an experiment series (approximately after 48 hours) with the corresponding biomass accumulation. The change of porosity from an ED to a later timestep can be seen, which is tracked in all timesteps. The remaining pore space after an experiment is calculated from the extracted initial pore fraction and the remaining void space after biomass accumulation. The red area in Figure 23 represents the pore space available for fluid transport. In contrast, the white area represents the grains of the rock structure (material:

glass), which naturally disturb the flow field and the black area displays the accumulated biomass.

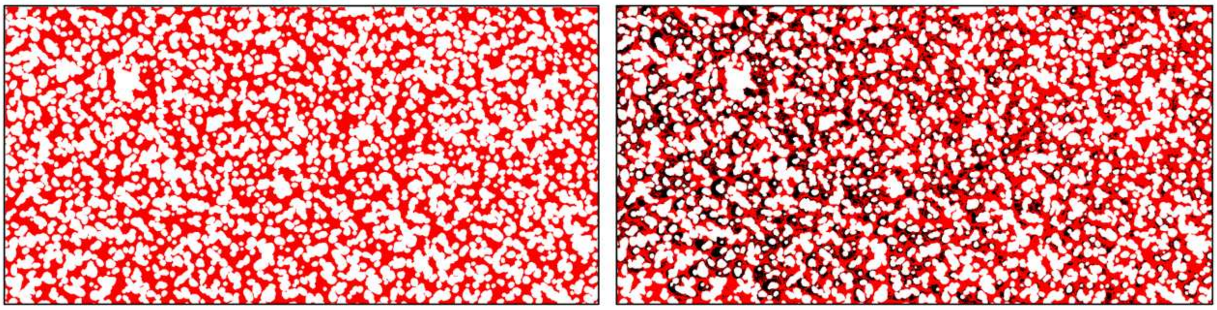

Figure 23: Input of images for the numerical simulator visualizing the pores (red), grains (white) and biomass (black). The flow direction of the domains is from left to right. Left: Empty total domain. Right: Total domain after 48 hours, including biomass accumulation.

3.3 Numerical setup – Simulation

Simulating the total domain of the micro model requires a punch of computing power. Hence, the simulations were performed on a 64-core server with 1 TB RAM running CentOS 7 (Linux-based system software). For numerical simulations, GeoDict 2022 was utilized. GeoDict, developed by the company Math2Market and the Fraunhofer Institute, is an innovative and easy-to-use material simulator that offers the complete solution for multi-scale 3D image processing, visualization, characterization of material properties and many more (Math2Market GmbH and Fraunhofer ITWM, 2022).

3.3.1 Model setup – Model creation

After the segmentation, the imported 3D image must undergo a further internal segmentation step of GeoDict, where the constituent materials must be selected. The grains are allocated to glass since the micro model consists of borosilicate glass. The pore volume is assigned to water (fluid) and the biomass is allocated to a porous solid, which can attain any number of internal permeability. The temperature of the simulation experiment is kept at 37 °C. Moreover, the software sets the fluid densities and viscosities by default value, which are 993,15 kg/m^3 and 0,71 cP for the corresponding temperature of 37 °C.

The image must be transformed into a three-dimensional structure. Therefore, the module “LayerGeo” was used to add additional layer. The starting point was based on the final setting of the previous work, which covered five layers, leading to a depth of 9,14 μm (Voxel-size: 1,828 μm). Several simulations with a variety of depths and settings were performed. However, the final state was the correct domain size (CDS) setting, including a curvature to fit the manufacturer’s blueprint, as seen in Figure 20. The depth is matched with ten layers with a thickness of 1,828 µm, which results in a depth of 18,828 µm. In general, the length is 1,828 µm per voxel. The empty domain exhibit 10871 voxels in x-direction (1,99 cm) and 5413 voxels in y-direction (0,99cm), which approaches the real domain size of 2 × 1 cm. The injection is directed towards the positive x-direction. Figure 24 depicts the schematics of the ED model.

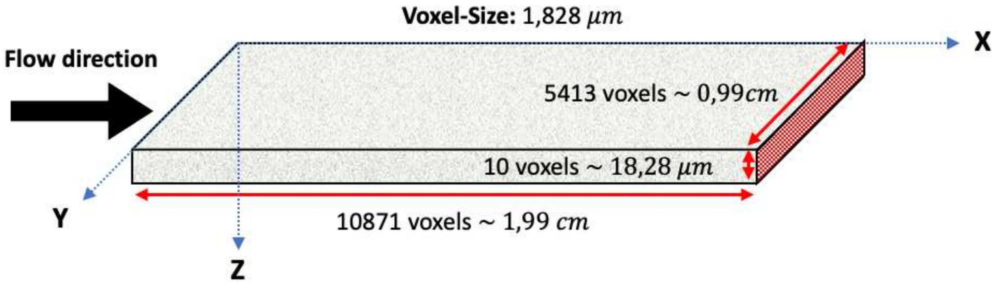

Figure 24: Schematic illustration of the empty domain (ED) model, including voxel number and sizes in cm and µm. The flow direction is in positive x-direction and the size is 1,828 µm per voxel. The red shaded area visualizes the flow area for the experiment input in the numerical simulator.

With the help of the module "ProcessGeo" and the command "Dilate" it was possible to dilate layers to create curvature. The base layer is the original size and the following layers on top of the base level are dilated by a predefined value. Due to the small number of layers, the smoothness of the curvature is limited to some degree. Furthermore, it must be added that the biomass covers the entire depth profile and is a possible source for deviated results. The interfaces between water and biomass are featured as straight and linear. The biomass is generally assumed to be homogeneously stretched vertically through the entire model depth, which is also not the case in the real structure. Except in the vicinity of the curvature, the biomass accumulation is cut off, which reduces the absolute amount of biomass in the model. Figure 25 represents an empty model's curvature and a biomass accumulated domain.

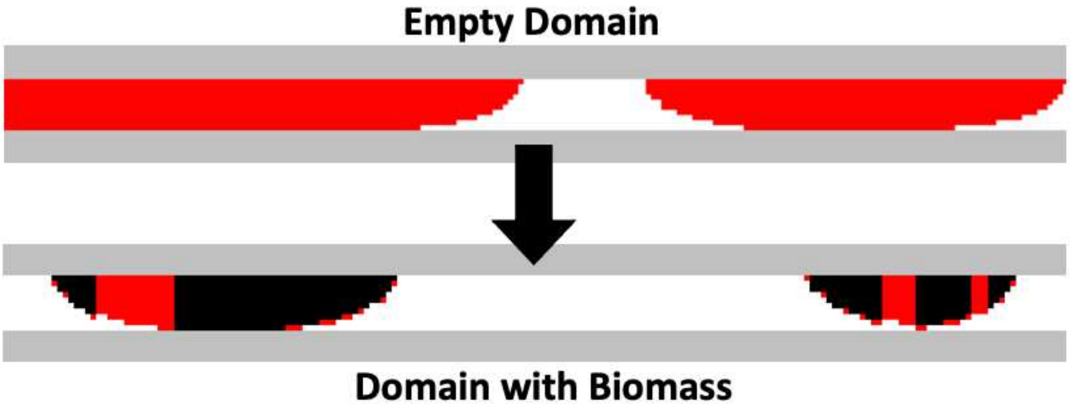

Figure 25: Schematic visualization of the curvature in GeoDict. Top: Empty domain (red area – water; white area – grain). Bottom: (Domain with biomass accumulation (red area – water; white area – grain; black area – biomass).

3.3.2 Model setup – Physical equations and solver

The "FlowDict" module from the GeoDict software can calculate flow properties and the permeability of porous media obtained by 3D image data. Especially permeability is an intrinsic property of a flow structure, which strongly depends on the geometry. A diversity of solver options is available to solve the flow field of the micro model. The selection of physical equations depends on describing the flow field (linear or non-linear) and the structure's material. The Stokes or Navier-Stokes equation can be used if the structure contains empty and solid voxels, as in a porous medium without any fluid (Hilden *et al.*, 2021).

Nevertheless, if biomass in a porous matrix including a defined permeability needs to be simulated, the Stokes-Brinkmann or Navier-Stokes-Brinkmann equations need to be selected. The Stokes-Brinkmann equation is applied for linear and laminar flows with empty, porous and solid voxels. A non-linear relationship between velocity and pressure drop will appear by increasing the flow speed or the injection rate. The influence of inertia needs to be considered, which can be handled by adding the Navier term (Hilden *et al.*, 2021). However, more computing power will be needed to solve and executed the simulations with the Navier-Stokes-Brinkmann Equation.

Besides the low injection rates of the experimental series, which are part of this master thesis and the structure of the simulation model, the Stokes-Brinkmann equation was selected. Furthermore, both solvers (Navier-Stokes-Brinkmann and Stokes-Brinkmann) were executed on three different domains (ED, first and last timestep of Exp. 2) if significant variances between the solver equations can be obtained. Table 4 represents the comparison result, which shows the duration of 10 % simulation runs.

Table 4: Comparison of using Stokes-Brinkmann or Navier-Stokes-Brinkmann equations based on the simulation duration of 10 % simulation runs. The simulation was done on three domains: ED, first and last timestep of Exp. 2. The experimental input was 50 mBar, 500 mD of biomass intra-permeability and 64 cores were used.

Description	Stokes-Brinkmann	Navier-Stokes-Brinkmann	Delta, Δ
Empty Domain	Time: ~ 12 min 10 %: 4,108 D	Time: ~ 40 min 10 %: 4,147 D	Time: ~ 28 min 10 %: 0,039 D
Scan-00 – First Timestep	Time: ~ 40 min 10 %: 2,396 D	Time: ~ 118 min 10 %: 2,452 D	Time: ~ 78 min 10 %: 0,056 D
Scan-15 – Last Timestep	Time: ~ 53 min 10 %: 1, 940 D	Time: ~ 165 min 10 %: 1,976 D	Time: ~ 112 min 10 %: 0,036 D

The experimental input for the comparison was 50 mBar, 500 mD of biomass intra-permeability and 64 cores were used, which is the total amount of available cores on this server setting. The results from Table 4 show shortened simulation times for the Stokes-Brinkmann compared to Navier-Stokes-Brinkmann. The accuracy of the 10 % outcome stays nearly unaffected, which emphasizes the selection of Stokes-Brinkmann.

For solving the Stokes-Brinkmann, the following equations need to be resolved in the numerical simulator, whereas Equation 12 is the conservation of momentum and Equation 13 is the conservation of mass:

$$-\mu\Delta\vec{u} + \mu K^{-1}\vec{u} + \nabla \mathrm{p} = \vec{f} \tag{12}$$

$$\nabla\vec{u} = 0 \tag{13}$$

where μ is the dynamic viscosity (kg/m·s), $\vec{u}$ is the velocity vector of the fluid (m/s), K^{-1} is the reciprocal of the permeability tensor (m^2) and μK^{-1} describes the flow resistivity. P represents the pressure component (Pa) and $\vec{f}$ is an external force (N).

For this set of equations, three different solvers for solving the partial differential equations are available in GeoDict: LIR, SimpleFFT and EJ. Which one should be chosen depends on the numerical nature and computing power. The LIR (Left-Identity-Right) solver was chosen due to its usage for linear and non-linear fluid flow and low memory requirements. Furthermore, compared to other solvers, the LIR solver is faster for highly porous materials (Hilden *et al.*, 2021).

The iterative process is stopped via an error bound. An error bound of 10 % flow permeability was chosen as the solver's stopping criteria to keep the relationship between simulation time and the necessary accuracy in an adequate proportion. Lower error bounds might iterate the result further, but these kinds of differences in the digital places of the result cannot be reproduced in an experimental approach.

Moreover, the relaxation factor, grid type and grid refinement can be adjusted. Due to the experience of fast and stable simulations, the relaxation was set to 1,2. The grid type was "LIR-Tree" and the grid refinement was "Enabled".

3.3.3 Model setup – Boundary conditions

Boundary conditions (BC) are a vital part of solving differential equations. The behavior of the fluid is dedicated to the BC if it faces an obstacle or is near the boundary border of the micro model. "Periodic", "Symmetric", "No-slip" or "Expert" boundary conditions can be elected for flow direction and tangential direction. Note: the simulated flow direction is in the positive x-direction, which implies that the z-direction is the tangential direction. The periodic option in flow direction is chosen due to the recommendation of (Hilden *et al.*, 2021) for best working in non-periodic structures due to the heavy accumulation of biomass in the entry area of the domain, with high porosity. The no-slip condition implies zero fluid velocity at the solid surface. In the tangential direction and hence on the surface of the solids, the no-slip boundary condition (Equation 14) is used for all simulation cases (Hilden *et al.*, 2021):

$$\vec{u} = 0 \qquad (14)$$

where, $\vec{u}$ is the velocity vector of the fluid (m/s).

Another crucial simulation input is the experiment inlet and outlet of the model, whereas the options of pressure drop, mean velocity, or flow rate are available. Pressure drop and the flow rate were mostly used in the master thesis. The experimental setup can measure the pressure drop between the inflow and outflow of the micro model. As empirically proved, a variance of pressure drop is not influencing the permeability results of the simulation, so the pressure drop was fixed at 50 mBar for all simulations.

For the extraction of velocity and stress fields, the experiment input must be changed to flow rate (l/min) on a flow area (cm^2). Two experimental series were executed during this master thesis: "Experiment 1_2021" with a flow rate of 0,2 ml/h and "Experiment 2_2022" with a flow rate of 0,05 ml/h. Thus, the flow rate can be calculated as 3,33$\times$10^{-6} l/min and 8,33$\times$10^{-7} l/min, respectively. The flow area was calculated based on the y- and z-lengths of the total domain, which results in a value of 0, 0018088 cm^2 (see Figure 24 for visualization: the red shaded area acts as the flow area).

Moreover, an implicit region of ten voxels each at the inlet and outlet (in flow direction) is added to avoid the possibility of closing inflow channels. Hence, the simulation gains stability and accuracy.

3.3.4 Model setup – Velocity and stress field

The detailed investigation of the velocity and stress field of the simulated domain is of interest to estimate the influence of biomass on nutrient supply. The accumulation of biomass changes over time and with it also the velocity and stress behavior. The velocity and stress field analysis aimed to investigate critical values and the general behavior of the velocity and the stress over time.

For the numerical establishment of the wanted fields, including a histogram analysis of the velocity and stress values, the following procedure must be performed:

1. GeoDict simulation: “FlowDict” Simulation of the desired domain.
2. Macro script (Appendix A.1): a macro script must be run in GeoDict to create the velocity and stress field. Furthermore, the script exports the field in an array (npz.-file) for further offline usage.
3. The stored npz.-files must be transferred to an offline computer for graphical plotting steps.
4. Python script (Appendix A.2): a python script on an offline computer must be used to create histograms out of the stored velocity and stress fields (npz.-file).

The execution of the python scripts requires different inputs in the boundary conditions and solver section in the “FlowDict” module. First, as discussed in the previous chapter, the experiment input must be changed from pressure drop to flow rate due to enhanced flow information needed to execute the python script correctly. Since the experiments in the lab are also conducted with a constant injection flow rate, this setting is changed to find the correct flow velocities and shear stress values. Further, it is expected that the channels get narrower over time by biomass accumulation, which will vary the pressure drop over the domain and hence, a constantly applied pressure drop will not correspond to reality.

Second, in the solver settings, “Discard PDE Solver Files” and “Write compressed Volume Fields” must be disabled. “Write compressed Volume Fields” is a function of GeoDict, which decrease the storage volume of simulated volume fields (e.g., velocity and stress fields). However, for the macro script execution, the entire information about the field is necessary. Figure 26 displays the commands with a red rectangular, which must be ticked off for correct python script execution.

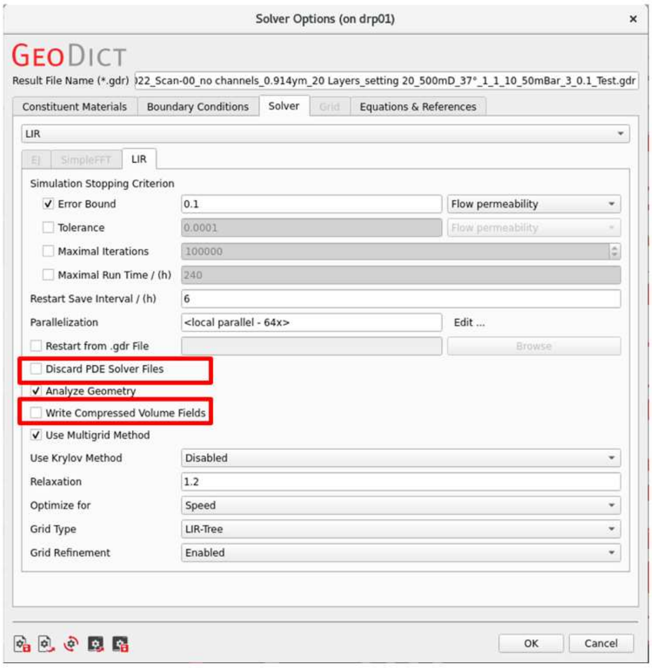

Result File Name (*.gdr))22_Scan-00_no channels_0.914ym_20 Layers_setting 20_500mD_37°_1_1_10_50mBar_3_0.1_Test.gdr

LIR

Simulation Stopping Criterion

☑ Error Bound 0.1 Flow permeability

☐ Tolerance 0.0001 Flow permeability

☐ Maximal Iterations 100000

☐ Maximal Run Time / (h) 240

Restart Save Interval / (h) 6

Parallelization <local parallel - 64x>

☐ Restart from .gdr File

☐ Discard PDE Solver Files

☑ Analyze Geometry

☐ Write Compressed Volume Fields

☑ Use Multigrid Method

Use Krylov Method Disabled

Relaxation 1.2

Optimize for Speed

Grid Type LIR-Tree

Grid Refinement Enabled

Figure 26: Solver Options in GeoDict. The red-marked commands must be disabled for correct python script execution.

Figure 27 summarizes the journey from the segmented image (simulation input) of GeoDict, over the visualization of the volume fields, to the histogram plot of velocity and stress. The histogram compares four different timesteps during an experiment series. The histograms at the top show the distribution of velocity and stress within the domain. In comparison, the lower part is a magnification of the peak at the beginning of the plot. The seventh slice out of tenth slices is chosen for the representation in the figure.

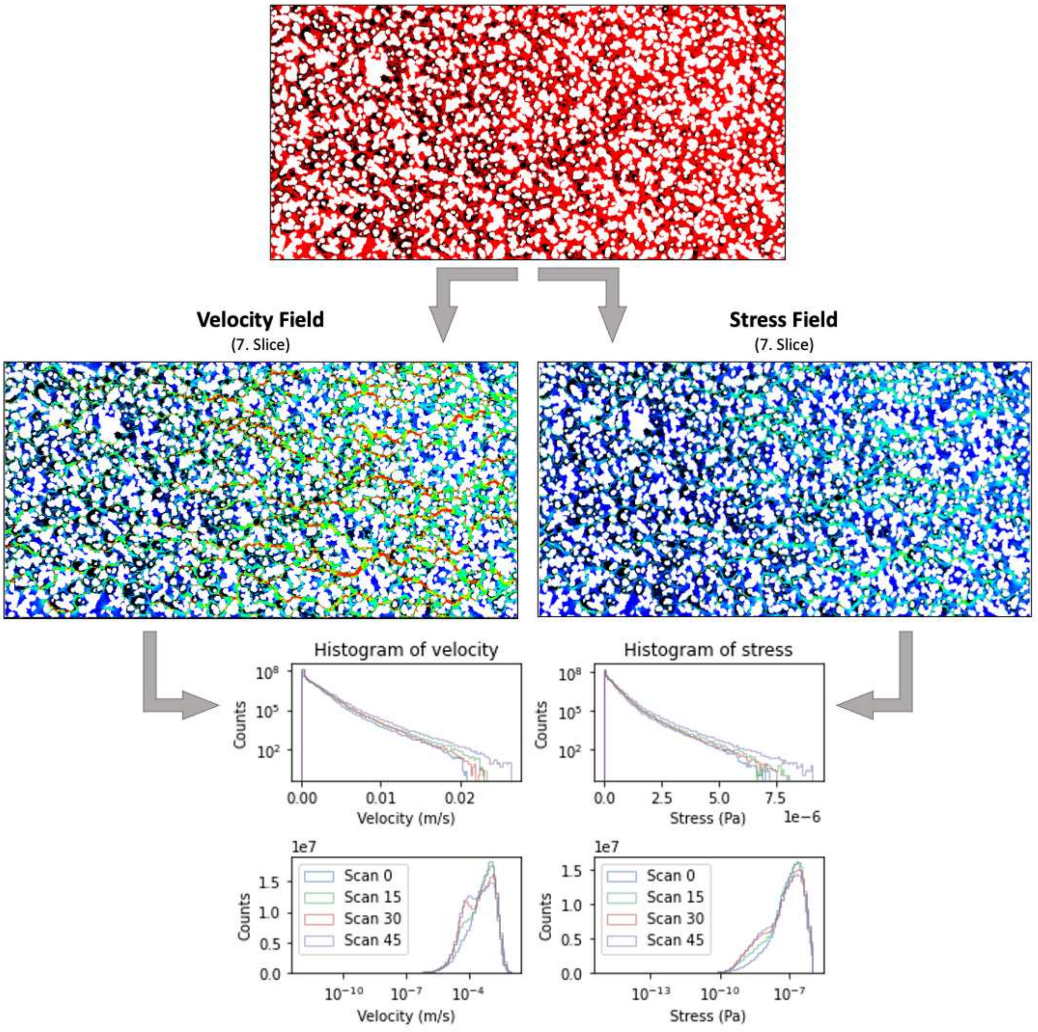

Figure 27: Schematic description of the journey from the segmented image (simulation input) over the visualization of the volume fields to the histogram plots. Top row: simulation input. Middle row: left – velocity field of slice 7. Right – stress field of slice 7. Bottom row: top – histogram of velocity and stress field of the total domain. Bottom – magnification of the peak at the beginning of the above histogram.

3.3.5 Model setup – Heterogeneity analysis

An additional analysis was conducted to investigate the heterogeneity of the total domain. The idea was to conduct a REV (Representative elementary volume) like analysis to research similarities over different sizes of the simulation area. A REV aims to find the spatial variability of an attribute at a coarser scale, given the variability at a finer scale (Singh and Srinivasan, 2014). The representative elementary volume is defined as the smallest rock volume representing the region of local heterogeneities for the length scale and the investigated property and when the averaged attribute becomes stable (Singh, 2017). The interest was to examine whether a small elementary volume could represent the total domain.

The analysis was conducted via a macro script, which symmetrically decreased the size of the TD in steps. The reduction step was 500 voxels in the x-direction (inflow and outflow) and 250 voxels in the y-direction (top and bottom). This step was repeated ten times until a domain size of 8 % of the total domain size remained. The numerical input stayed the same as for the standard case simulations, which can be seen in Table 5. Figure 28 schematically represents the procedure and working principle of the macro script, where the percentage values correspond to the total domain size of the time step of the experiment stage.

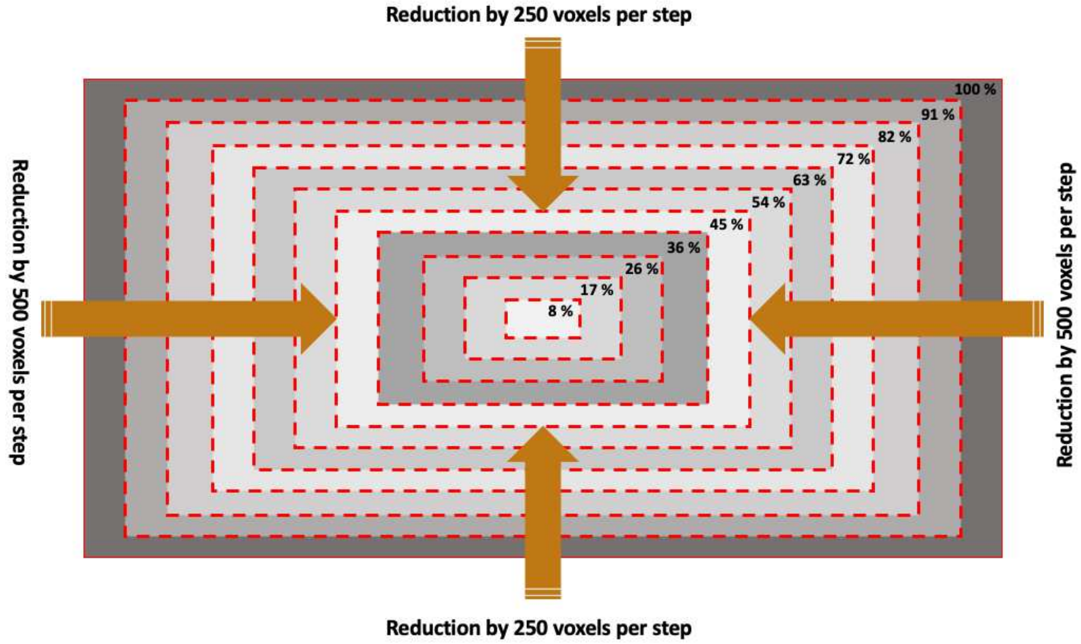

Figure 28: Schematics and working principle of the heterogeneity analysis macro script, including the total domain size reduction steps and percentage values of the remaining domain size.

3.3.6 Summary of numerical input

Table 5 summarizes all crucial input parameters for the numerical simulator applied to the simulations executed during this thesis. The table is split into the standard case/heterogeneity analysis and velocity/stress field analysis. The last-named category required different numerical inputs to be executed. Therefore, the additional column is inserted for modifications in the numerical settings. The column is only filled with content if settings other than the standard case must be applied. Otherwise, the columns stay empty and the standard case setting was used. The settings were applied to TD as well for ROI simulations.

Table 5: Summary of critical numerical inputs for the standard case/heterogeneity analysis and velocity/stress field analysis.

Description	***Value/Input***	
	Standard Case/ Heterogeneity Analysis	Velocity/Stress Field Analysis
Curvature implemented	Yes – 10 layers	
Temperature	37 °C	
Permeability	0/ 100/ 125/ 500mD	
Solver		
Set of Physical Equations	Stokes-Brinkmann	
Solver	LIR	
Error Bound	10 % of permeability	
Relaxation	1,2	
Boundary Conditions		
Computation Direction	x-direction	
BC in Flow Direction	Periodic	
Implicit Region	10 voxels	
Experiment Input/Output	**Pressure drop:** 50 mBar	**Flow rate:** $3{,}33\times10^{-6}$ or $8{,}33\times10^{-7}$ l/min **Flow area:** 0,0018088 cm^2
BC in Tangential Direction	No-Slip	

3.3.7 Simulation roadmap

At the very beginning, simulations from the doctoral thesis (Hassannayebi, 2019) and the follow-up master thesis (Jammernegg, 2020) were repeated to understand the subject better and familiarize with the GeoDict software. The starting point was based on the final setting of the previous works, which covered five layers, leading to a depth of 9,14 μm (Voxel-size: 1,828 μm). The aim was to recreate those values and match them for five layers settings with the manufacturer's plan of 2,5 D. However, the starting point of this thesis was six layers, which best reproduced the results from this experimental series, including the new microbes M. Formicicum.

The global aim of this thesis was to enhance the numerical setting toward the genuine manufacturing plan of the microchips and the natural experimental setting. As a last consequence, the permeability value for the empty domain should approach the original 2,5 D. These main variances of the numerical setting were conducted: inclusion of channels, approaching the actual depth of the microchips (20 μm) and implementation of curvature into the simulation model.

Prior simulations in previous works excluded the inflow and outflow channels, as depicted in the MM's manufacturing building plan (Figure 20). Therefore, empty masks were created to illustrate microchips with an 8-line-path inflow/outflow system. Further on, cropped channel and fully elongated channels masks were created, whereas fully elongated masks make much more sense. Nevertheless, since the experimental setting can only take pictures of cropped images with biomass, this type was also investigated. With the current experimental setting, it is not possible to display microbe accumulations in the inflow or outflow lines, so a trade-off value between the empty domain model without channels and with channels must be found. Figure 29 represents the three available alternatives of masks: simulation mask without inflow/outflow channels, simulation mask with cropped inflow/outflow channels and a simulation mask with fully elongated inflow/outflow channels. The masks were created with ImageJ.

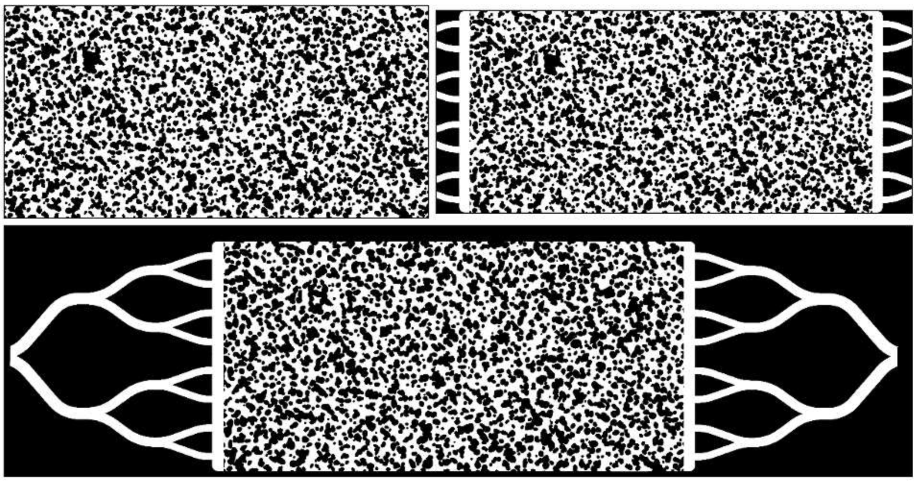

Figure 29: Simulation masks of empty domains (no biomass). Top left: simulation mask without inflow/outflow channels. Top right: simulation mask with cropped inflow/outflow channels. Bottom: simulation mask with fully elongated inflow/outflow channels.

Furthermore, it was essential to adjust the curvature of the model to be as realistic as possible and that was a necessary premise for the velocity and stress field analysis. As Figure 30 sketches, several settings were screened until the final setting was brought up. As already mentioned, the first executed simulations were conducted on six-layer settings without a curvature, which fit the original 2,5 D quite well. Even so, the micro model depth does not correlate with the original depth of 20 μm. With a voxel size of 1,828 μm and six layers, the depth of the simulation model results in a depth of 10,968 μm, which is approximately only half of the actual setting.

Therefore, in the next step, the number of layers increased to 20. The chosen voxel size was halved to 0,914 μm, which approximates the original depth of the model. The finer voxel size and the increased number of layers enabled a perfect combination to shape flawless curvature for the channel structure. A punch of iterative simulation runs was conducted to end up with the result depicted in Figure 30. Due to the halving of the voxel size, even the domain size in the x-and y-direction decreased, which ended up in a halved TD (1 cm × 0,5 cm × 18,28 μm).

The re-establishment of the correct domain size (CDS) model required a new segmentation in GeoDict and the number of layers in the z-direction was halved to ten layers and the depth profile was averaged. After this operation, the voxel size in x-, y- and z-direction became 1,828 μm per voxel. Through this reduction in the z-direction, the symmetric curvature was averaged and concomitantly, the exact resolution from the previous setting got lost. However, the CDS was restored (2 cm × 1 cm × 18,28 μm).

Figure 30 documents the journey from six layers without an implemented curvature to the final setting of the correct domain size with curvature. The main simulation model was the CDS model with implemented curvature. Another aspect that can be obtained from the figure is that biomass is distributed over the entire depth and gets cut off if placed around the curvature area. Both facts may lead to numerical errors when the results are matched to the experiments.

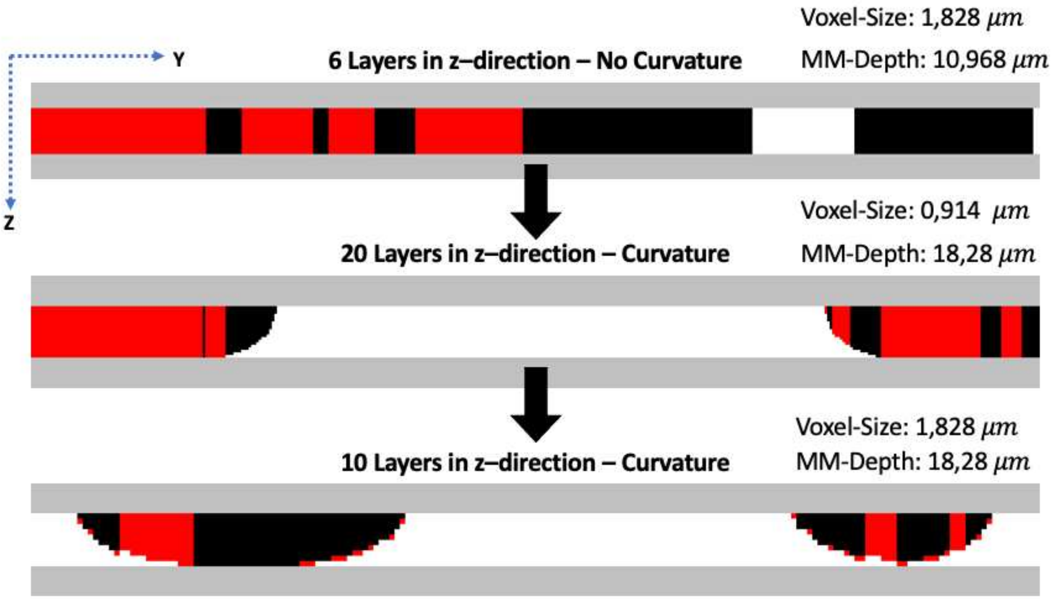

Figure 30: The schematic illustration of the journey from a six-layer model without a curvature to a ten-layer model with a curvature. The slices are depicted in the x-direction. White area: grains/glass. Red area: water. Black area: biomass. Top: six-layer model without a curvature (Voxel-size 1,828 µm; Micro model depth: 10,968 µm). Middle: 20-layer model with curvature (Voxel-size 0,914 µm; Micro model depth: 18,28 µm). Bottom: ten-layer model with curvature (Voxel-size 1,828 µm; Micro model depth: 18,28 µm).

Chapter 4

Results and Discussion

This chapter summarizes the impact on the hydraulic properties of the pore network. Two experimental series were conducted: Experiment 1 (flow rate: 0,2 ml/h; duration: 48 h) and Experiment 2 (flow rate: 0,05 ml/h; duration 60 h). First, the empty domain (ED) was fitted to the experimental outcomes. Based on this, simulations with various biomass permeability values were executed. Second, velocity and stress fields on the total domains were created and the behavior at different permeability values over time was investigated. The analysis was performed using python scripts, which allowed the comparison of model outputs in a histogram. In the next step, the study on the region of interest was commenced on two sections of interest. Moreover, a heterogeneity analysis of the total domain was included to find a representative volume for the total domain.

4.1 Empty domain fitting

A sensitivity analysis of empty models is depicted in Table 6 and Table 7. The influence of channels and curvature in the simulation domain is analyzed. Furthermore, the difference in numerical results at different stopping criteria is investigated, comparing 5 % and 10 % error tolerance simulations. Lower error bounds than 5 % will increase the simulation time enormously and will not improve the result significantly. In general, the duration of simulations, including microbial accumulations, is much higher than in empty models. Therefore, domains with biomass accumulation were simulated with a 10 % error tolerance.

A delta value of approximately 0,5 D is in the range of the experiment variations and therefore, acceptable. Further, the original value from the manufacturer for an empty domain is 2,5 D with a porosity of 57 %. As described in the simulation roadmap, the six-, ten- and 20-layer models were analyzed, but only the six-layer- and ten-layer models are discussed in detail.

4.1.1 Six-Layer model

The six-layer model was the starting point in the simulation roadmap. Table 6 compares the simulation outcome of the 5 % and 10 % of the six-layer model without and with channels. It should give an idea about the magnitude of the distinct influence of including channels in the simulation domain. Consequently, a trade-off value can be located and used for forecasting without adding the channels to the simulation run. Furthermore, the numerical accuracy is investigated towards 5 % and 10 % simulation runs. This trade-off can prevent reducing to 5 % error bound of simulation, saving time executing the simulations. The delta columns/rows indicate the difference between the different variables.

Table 6: 5 % and 10 % simulation results of the empty domain of the six-layer model without and with channels, including porosity values of the domains. The delta should give an idea about the simulated variable sensitivity.

6-Layer Model	10 % error	5 % error	Porosity, ϕ	Delta, Δ
w/o Channels	2,94 D	2,39 D	54 %	0,55 D
w. Channels	2,41 D	2,01 D	37,12 %	0,40 D
Delta, Δ	0,53 D	0,38 D	16,88 %	

The six-layer model approximates the value of the manufacturer for permeability and porosity. Except for the model with channels, the porosity value is lower. Thus, can be explained because GeoDict is calculating the porosity of the total given image. Figure 29 (bottom picture) displays large solid areas beneath the inflow/outflow channels (black spots). This will increase the total amount of solid voxels in the denominator, resulting in smaller porosity values. So, the consequence of this value can be invalidated. Another notable fact is that, including channels to the domain, the permeability is decreasing in a range from 0,38 - 0,53 D. The influence of the numerical stopping criteria is in a range from 0,40 - 0,55 D. The values are very close to fitting the original values and thus is preferable for simulation forecasting. However, the six-layer setup does not match the micro model dimensions in the z-direction and was therefore improved.

4.1.2 Ten-Layer model

The ten-layer model aimed to represent the corrected domain sizes (CDS) of 2 cm × 1 cm × 20 μm. Especially, the depth of the CDS with 18,82 μm resembles the original micro model vertical extension better. This model also includes an averaged curvature (see the bottom picture of Figure 30) and the subject for further simulation on biomass accumulated domains.

Table 7 compares the simulation results at 5 % and 10 % error tolerance without and with channels. Additionally, it should give an idea about the magnitude of the influence of curvature on permeability and porosity.

Table 7: 5 %, 10 % and porosity simulation results of the empty domain of the ten-layer model without and with channels vs. without and with curvature. The delta should give an idea about the magnitude of the distinct influence variable.

10-Layer Model (CDS)	w/o Curvature	w. Curvature	Delta, Δ
w/o Channels	10 % = 6,68 D 5% = 5,73 D ϕ = 54,18 %	10 % = 4,11 D 5% = 3,61 D ϕ = 47,75 %	10 % = 2,67 D 5% = 2,12 D ϕ = 6,43 %
w. Channels	10 % = 5,55 D 5% = 4,84 D ϕ = 37,12 %	10 % = 4,35 D 5% = 3,35 D ϕ = 33,76 %	10 % = 1,15 D 5% = 1,49 D ϕ = 3,36 %
Delta, Δ	10 % = 1,13 D 5% = 0,89 D ϕ = 17,06 %	10 % = 0,24 D 5% = 0,26 D ϕ = 13,99 %	

The curvature impacts the CDS model significantly. Especially in the model without the channels, a high delta value for 5 % and 10 % simulations was reached. The influence of the curvature for the model ranges between 1,15 to 1,49 and 2,12 to 2,67 D for the simulated model with channels and without them, respectively. The impact on porosity is comparable to the previously introduced models. The simulated model, including curvature and channels for the 5 % case, is notable and resembles the experimental data best.

As mentioned, the reported value from the manufacturer for an empty domain is 2,5 D and was experimentally matched with the best approximation within the CDS model. The simulation at later time steps was performed with the setting including the curvature but corrected for the lack of channels by subtracting the absolute difference in ED resulting from the in- and outflow channels. Furthermore, the difference in numerical error tolerance was also included to reduce the impact of systematic error.

4.2 Experimental and simulation results

First, experimental results were shown based on the experimental setup described in Chapter 3. As already mentioned, two experimental series are part of this master thesis: Experiment 1 and Experiment 2. Additionally, it must be noted that Experiment 1 was executed in two parts. Therefore, the notations of part 1 (Exp.1-1) and part 3 (Exp.1-3) can occur. But both parts covered represent experiment 1.

4.2.1 Experimental results

Figure 31 displays the experimental pressure readings of experiment 1 with a flow rate of 0,2 ml/h and experiment 2 with a flow rate of 0,05 ml/h over time. The differential pressure is converted to permeability values via Darcy's equation (Eq. 2). Exp. 1 was stopped after 48 h and Exp. 2's duration was approximately 60 h. Further, the biomass saturation S_{Bio} over time is included, which indicates a growth of biomass saturation in the domain. The biomass saturation is related to the overall porosity of 57 % porosity (see Table 3). Simultaneously, with the increasing biomass, the experimental permeability decreases, as expected. Both permeability readings start at approximately 2,5 D and are reduced to 1 D for experiment 1 and 0,6 D for experiment 2.

Moreover, especially in experiment 2, filtration events can be detected. After approximately 36 hours (Exp. 2), the shear stresses are high enough to cause sudden rupture and detachment of the biomass. As described in previous chapters, significant biomass reconfigurations can be observed by a sudden pressure jump. Resulting velocity and shear stress variations are the primary drivers of those detachment and re-attachment events. Furthermore, according to Clement *et al.* (1997), detachment and sloughing are considered differently based on the size of the biomass portion. Detachment is the continuous separation of a small number of microbial cells driven by shear forces. Sloughing is the detachment of large biomass portions, which might also be recognizable by the varied height of the pressure readings.

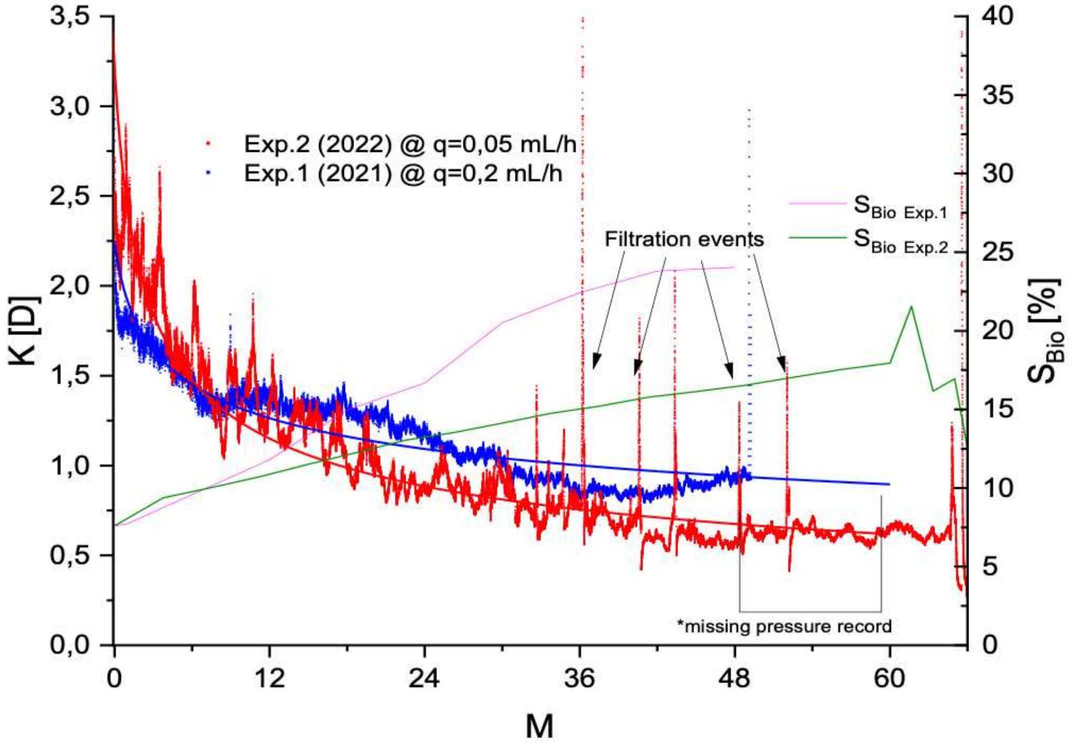

Figure 31: Experimental results of Exp. 1 and Exp. 2 over time and biomass saturation over time.

Figure 32 shows the experimental permeability evolution, k_{exp} of experiments 1 and 2 over time. Three trend lines for porosity, Exp.1 and Exp.2, were implemented to fit the experimental data. The permeability trend for both experiments is similar, with an offset that might be subject to different injection flow rates and biomass growth behavior. The second experiment reaches lower permeability values due to lower injection rates and higher biomass accumulation density near the micro model injection area.

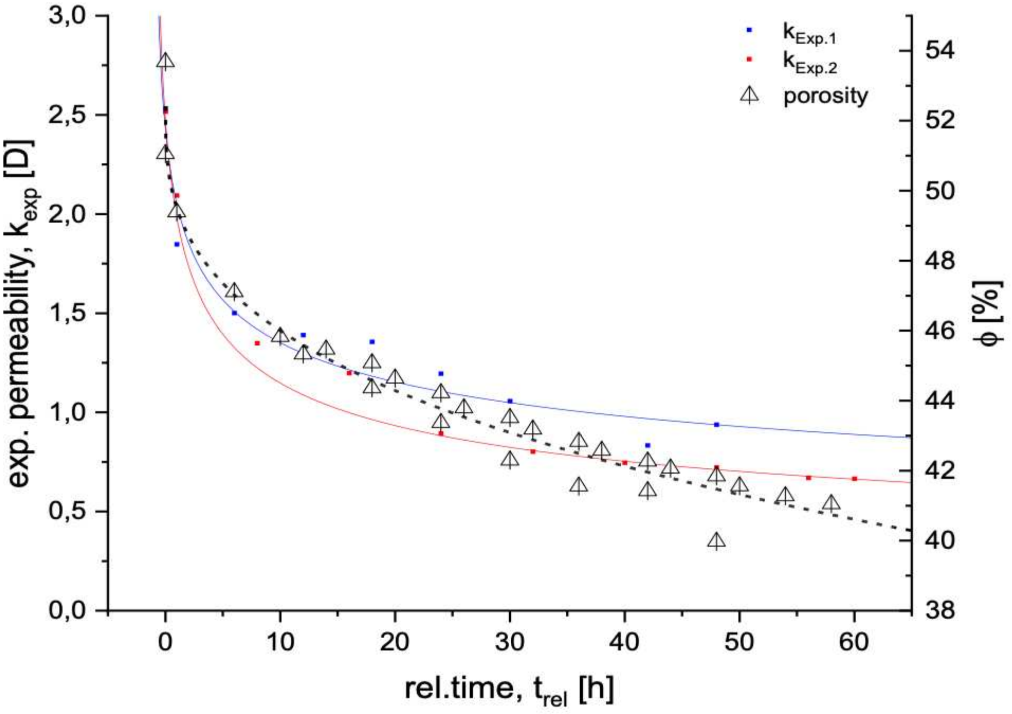

Figure 32: Experimental permeability k_{exp} over time (Exp. 1 and Exp. 2), including porosity.

Table 8 compares the experimental porosity and the porosity extracted in the numerical simulator on the curved model. A slight deviation can be detected and therefore, a root mean square error (RSME) was calculated based on the delta values in Table 8. The outcome of the RMSE and the deviation in porosity is 4,43 %.

Table 8: Comparison of experimental and simulated (with curvature) porosity

Timestep	ϕ - Experiment	ϕ - Simulation	Delta, Δ
Exp. 1 – After 1 h	49,39 %	44,39 %	5,00 %
Exp. 1 – After 48 h	39,98 %	37,16 %	2,82 %
Exp. 2 – After 1 h	45,83 %	40,81 %	5,02 %
Exp. 2 – After 60 h	41,10 %	36,60 %	5,50 %

4.2.2 Simulation results

The permeability and porosity values were determined according to the methodology described in Chapter 3. The plotted simulation results show the difference between the implemented error tolerance and the error from including inflow and outflow channels, as discussed in Chapter 4.1. The permeability values of the simulated time series are corrected by the systematic error resulting from the simulation tolerance and excluded channels. These values are summarized in Table 7. Of relevance is the difference between the 5 % and 10 % error simulations, including curvature, without channels, compared to the values from the simulations, including channels and curvature. Furthermore, the offset extracted from the correlogram in Figure 33 was used to calibrate the simulator. Thus, a systematic correction factor of 0,2585 D was applied to the simulation outcomes of the 10-layer model.

Figure 35 demonstrates the graphical interpretation of the offset value, which resulted from executing a variety of biomass permeabilities. The cross-plot displays simulated vs. measured permeability data of the 10-layer model. For Exp. 1, the permeability cases were impermeable (0 mD), 100 mD and 250 mD. For Exp. 2, the biomass permeability was impermeable (0 mD), 125 mD and 150 mD. The red area in the plot represents the maximal biomass permeability variance of Experiment 1. The red dotted line indicated an offset value of 0,2585 D on the y-axis, which is a systematic error.

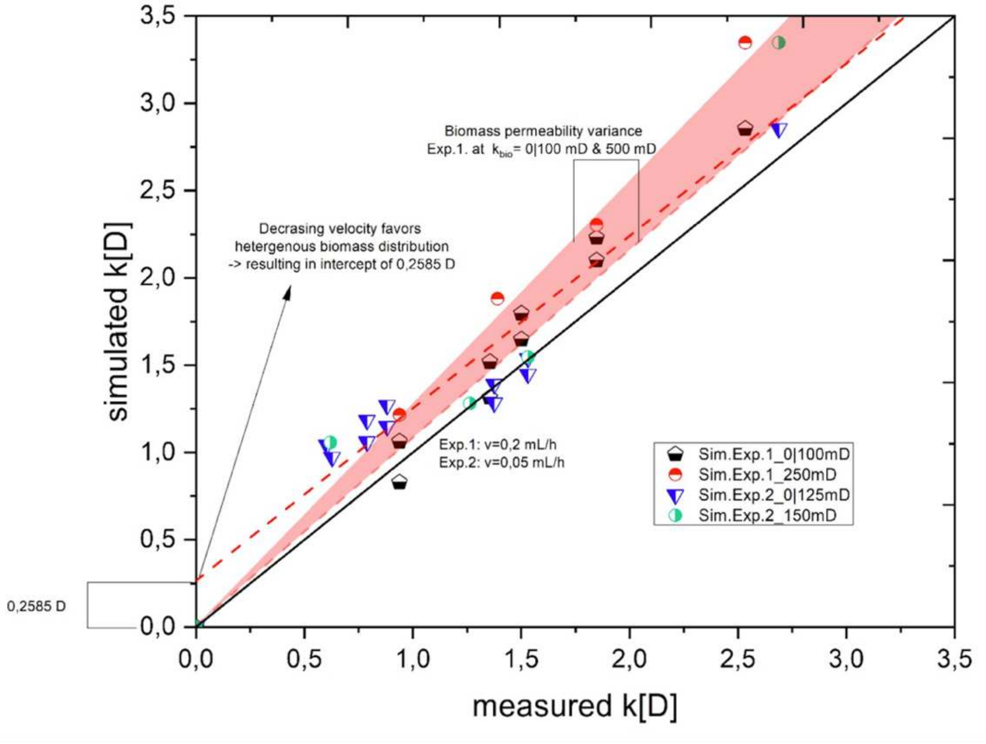

Figure 33: Correlogram showing measured vs. simulated data to illustrate the systematic error of 0,2585 D.

Figure 34 compares the experimental and the simulation results at different intra-biomass permeabilities over time. The black dotted lines represent the trend for both experiments and the red line is the parametrization of Exp. 2 with simulated 0 mD and 125 mD biomass permeability. The biomass permeability covered in the green triangles (0 mD and 125 mD) fit very closely with the experimental results. For Exp. 1, the biomass permeability ranges between 0 mD and 500 mD, where the violet triangle (0 mD and 100 mD) approaches the experimental results best. In general, lower permeability of biomass will lead to reduced nutrient distribution by advection. Therefore, the packages of the same symbol arrange from top to bottom according to the number of the biomass permeability. The gathering of 150 mD, 250 mD and 500 mD simulation outcomes (Exp. 1: turquoise triangle; Exp. 2: black triangle) match the experimental trend only in the early phase. In the area between 6 and 24 hours, the trend can only be fitted by reduced biomass permeabilities (violet and green triangles). After 30 hours of simulation, the establishment of preferential flow paths (PFPs) is increasingly impacting hydraulic properties. Thus, the declining trend flattens and a plateau is formed, which indicates a quasi-static equilibrium between net accumulation and detachment and is symbolized by the blue lines. This trend can also be seen in Figure 31. After a steep dipping trend, the permeability readings start to fluctuate after 30 hours, significantly reducing the slope.

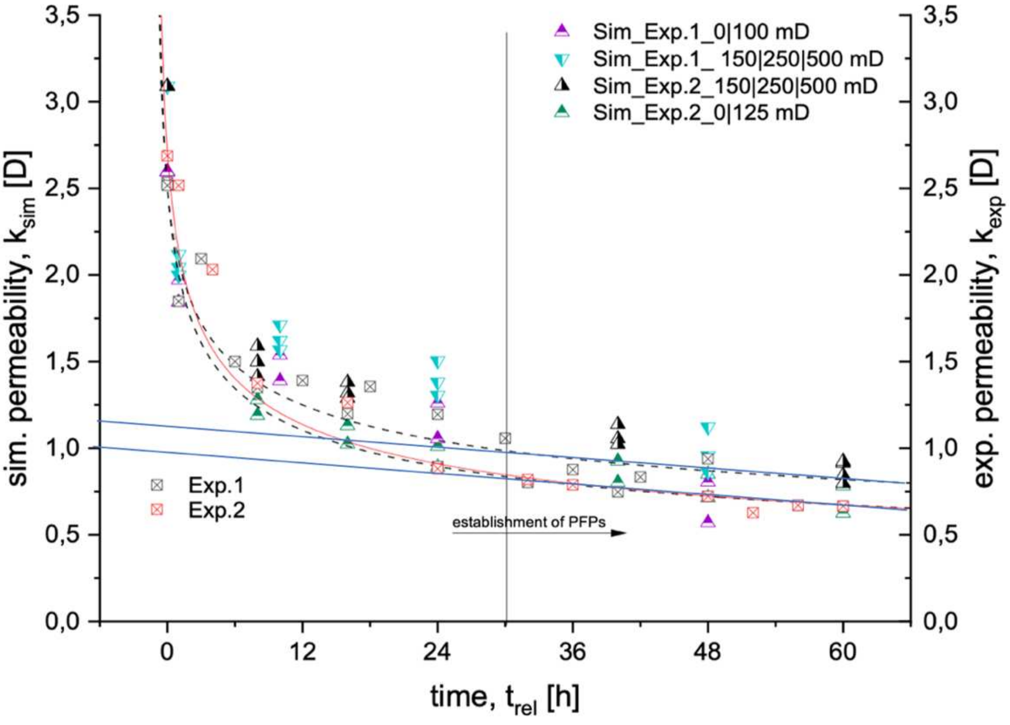

Figure 34: Simulation results of Exp. 1 and Exp. 2 over time with varied intra-permeabilities of the biomass matched with experimental results of Exp. 1 and Exp. 2 over time. The biomass permeabilities for Exp. 1 are 0 mD, 100 mD, 150 mD, 250 mD and 500 mD. The biomass permeabilities for Exp. 2 are 0 mD, 125 mD, 150 mD, 250 mD and 500 mD.

Figure 35 shows a normalized porosity-permeability reduction plot of experimental and simulation results. The x-axis $(1-\frac{\phi}{\phi_0})$ is represented via the porosity ϕ and the y-axis $(\frac{K}{K_0})$ via permeability K, where ϕ_0 and K_0 are derived from the ED. The two experimental series are matched with the following power law (Equation 15) and displayed by red lines in the plot (Ott, Roels and De Kloe, 2015):

$$\frac{K-K_C}{K_0-K_C} = \left(\frac{\phi-\phi_C}{1-\phi_C}\right)^{\tau} \quad (15)$$

where K is the actual permeability, K_0 is the reference permeability of the empty domain and K_C is the critical permeability, which is the permeability of the last timestep of the experimental series. Porosity ϕ represents the actual porosity and ϕ_C is the critical porosity (last timestep of the experimental series). τ displays the exponential coefficient, which is, in this case, -1,5.

Figure 35 compares normalized experimental results with normalized simulation results. The simulations were conducted with 10 % stopping criteria and the correction factors were applied. Three different biomass permeabilities (0 mD, 100 mD/125 mD and 250 mD) were used to match the experimental outcomes and come up with matched biomass permeability. The trend line of experiment 1 can be captured between the 0 mD and the 100 mD results. The trend line from Exp. 1 intersects the y-axis at an estimated biomass permeability of 105 mD.

On the contrary, experiment 2 faces a disruption after four measured points. First, the 125 mD and 250 mD outcomes match best and after the interruption, the experimental results approach the 0 mD simulation results. The intersection point exhibits a critical biomass permeability of 33 mD, representing a fully accumulated biomass domain that allows even a fluid flow.

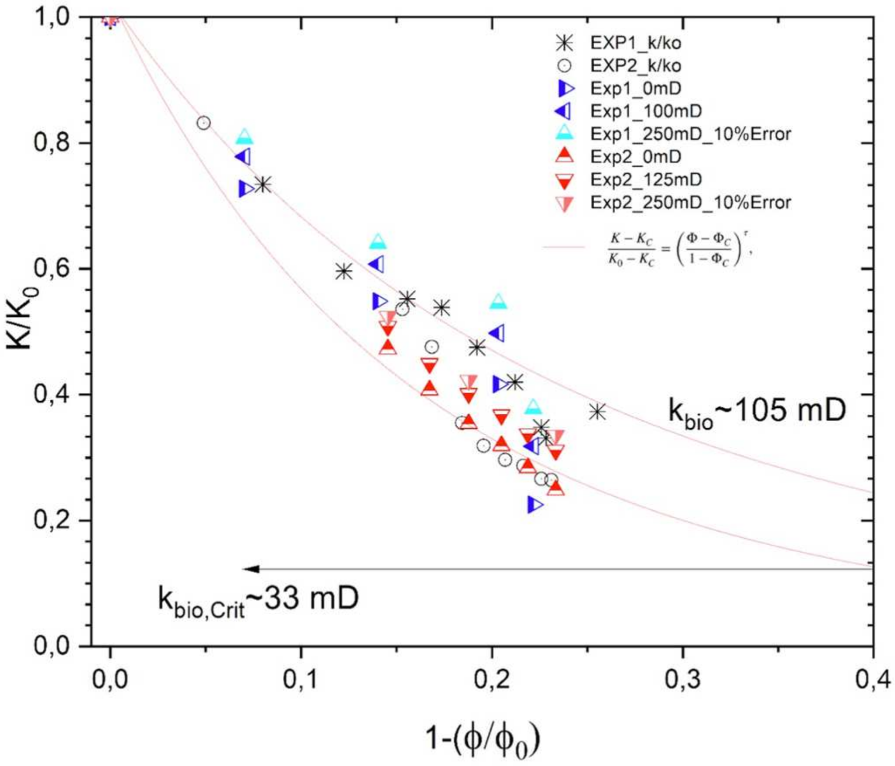

Figure 35: Comparison of experimental and simulation results (different biomass permeabilities) in a normalized porosity-permeability reduction plot. The trend line correlation is conducted via Eq. 16.

4.2.3 Porosity vs. Biomass

The porosity is reduced with increasing biomass accumulation. The exact change in the simulated pore space composition of experiment 1 (48 h) and experiment 2 (60 h) is illustrated in Figure 36 and Figure 37. The grain volume of the simulated domain is 52,25 %, which results in an available pore space of 47,75 %, as depicted in the ED case. The pore space during the simulation is assumed to be occupied by liquid. The plots are related to the total domain and contain the implemented curvature.

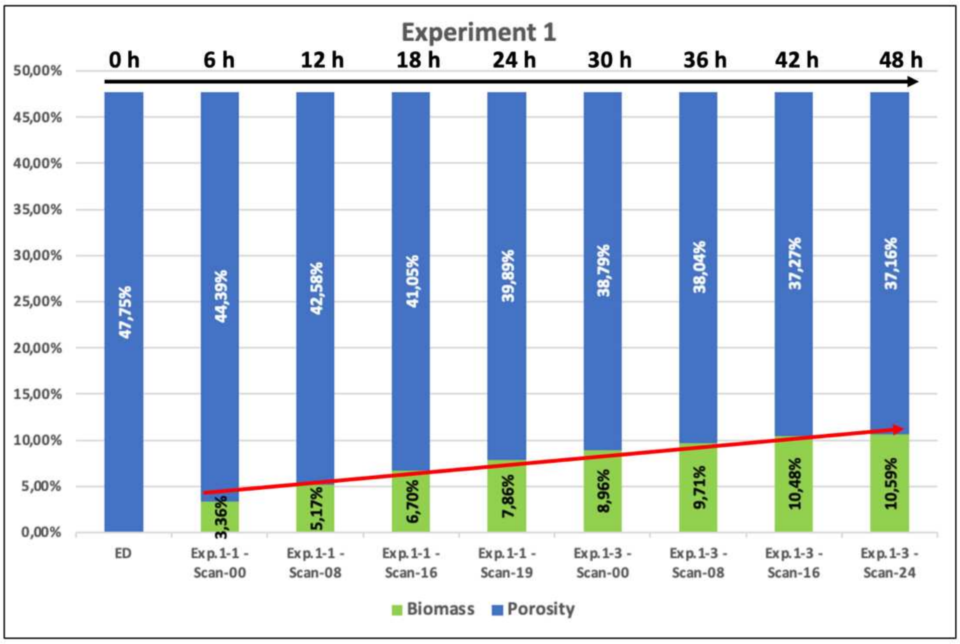

Figure 36: Experiment 1 - Illustration of the change in pore space composition on the total domain (w. curvature), showing ED and eight additional scans over time. The grain volume of the domain exhibits 52,25 %. The blue bars refer to the porosity and the green bars represent the growth of the biomass.

Experiment 1 (Figure 36) started in the first timestep after one h with a biomass accumulation of 3,36 % and ended at 10,59 % after 48 h. This is an increase of 315 % and represents a growth rate of 0,15 % biomass volume per hour. Experiment 2 (Figure 37) was conducted over 60 h. The initial biomass accumulation was relatively high in the beginning at 6,94 % and the experiment ended at 11,15 %. The biomass increase is 160 % compared to the beginning and the growth rate is 0,07 % biomass volume per hour.

The different flow rates might explain the difference in biomass growth over time. Exp. 1 has an experimental flow rate of 0,2 ml/h, four times higher than in Exp. 2.

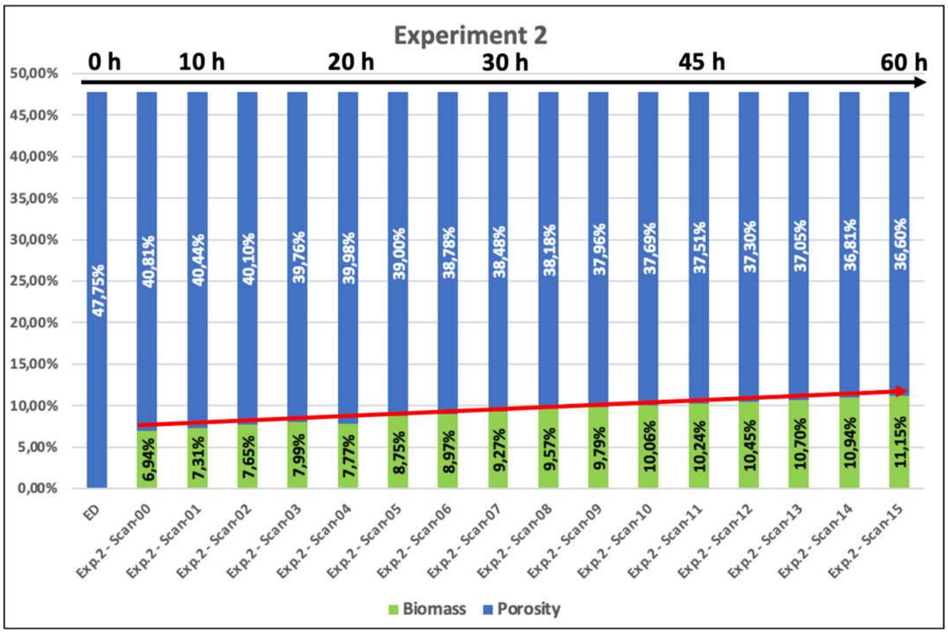

Figure 37: Experiment 2 - Illustration of the change in pore space composition on the total domain (w. curvature), showing ED and 16 additional timesteps over time. The grain volume of the simulated domain exhibits 52,25 %. The blue bars refer to the porosity and the green bars represent the growth of the biomass.

The implementation of curvature impacts both porosity and biomass accumulations since these are vertically distributed, as depicted in Figure 25. The porosity and biomass volume slightly decrease in the model with curved edges. Table 9 compares the root mean square error of porosity and biomass.

Table 9: Comparison of porosity and biomass within the curved model and without curvature via calculating the root mean square error.

Description	**Porosity - RMSE**	**Biomass - RMSE**
w/Curvature vs. w. Curvature	4,75 %	1,54 %

4.3 Velocity and stress field analysis

In general, biomass accumulations decrease the permeability and porosity of the domain. They may gather as stream tracers, especially in high-velocity areas, as biofilms, which tend to form thin layers covering the surface, or as bigger aggregates, called clumps (Hassannayebi, 2019; Jammernegg, 2020). In a constant flux system, narrower pore throats lead to increased flow velocities and, consequently, higher shear stresses (Thullner, 2008). The impact of shear stress influences the spatial distribution of biomass. Therefore, the flow fields, including velocity and stress values at different intra-permeabilities of the biomass, are studied. The histograms show a shift towards higher values for both properties, impacting the accumulation rate.

4.3.1 Introduction to flow field simulations

After the simulation run in GeoDict, a macro script (Appendix A.1) was executed to establish the velocity/stress field and make the data available to store in an array (npz.-file). The array contains velocity and stress data of approximately 280 million lines. It must be noted that the python script removes all zero values of velocity or stress to reduce the amount of data in the array. The extracted npz.-file will be used as an input file for the python script (Appendix A.2), leading to four histograms. The histograms show the velocity and stress distributions in the simulated domain. Furthermore, two plots, located at the bottom row of the plots, are used for zoomed investigation at the beginning of the histogram for enhanced analysis. This enables the comparison of varied timesteps, including different biomass permeability.

Due to the implementation of the curvature to the domain, the layers or slices are dilated from top to bottom. This leads to different velocity and stress distributions over the depth profile. The following figures show a collection of varying flow channels in the simulation domain in the x-direction with the vertical distribution of velocity and stress of the empty domain. In Figure 38, the high velocities occur preferentially in the center of the flow channel or even in the curved edge region. The velocity decreases from the center of the high velocities towards the outside. Due to the no-slip boundary condition, the velocities in the near vicinity of the borders are zero. Furthermore, the slices are numbered from top to bottom (slice ten to slice one), whereas slice number 10 at the top refers to the original layer size the remaining layers are modified.

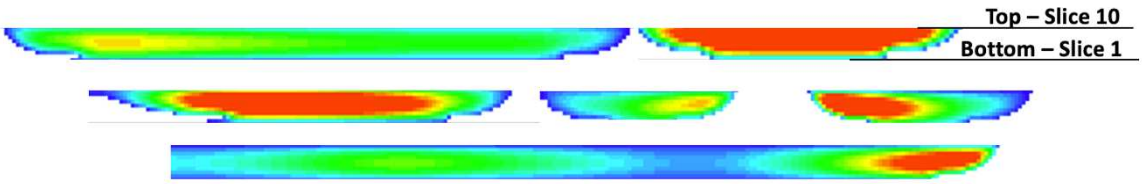

Figure 38: Collection of flow channels showing lateral velocity distribution. Red color: high velocity. Blue color: zero velocity.

In contrast, the shear stress is the space derivative of velocity, leading to the velocity gradient multiplied by viscosity, as depicted in Equation 16. Hence the shear stress maximizes towards the zones where the velocity is small in the model.

$$\tau = \mu \frac{\partial u}{\partial y} \qquad (16)$$

Where τ is the shear stress (Equation 11), μ the dynamic viscosity and $\frac{\partial u}{\partial y}$ the velocity gradient or the rate of shear deformation.

Figure 39 shows a collection of flow channels with high-stress spots. High shear stresses occur tendentially around borders and the channel's center exhibit no shear stresses. The order of slices stays consistent: the top is slice ten and the bottom is slice one.

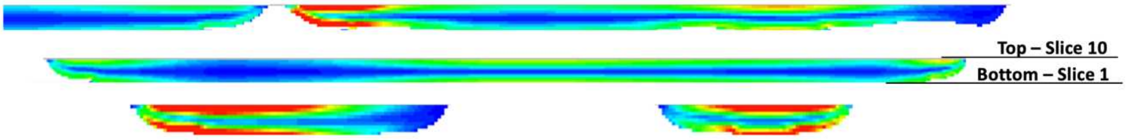

Figure 39: Collection of flow channels showing lateral stress distribution. Red color: high stress. Blue color: zero stress.

Figure 40 represents slice 7 of the velocity field of the empty domain. The naked eye can see varied preferential flow paths considering the high-velocity readings.

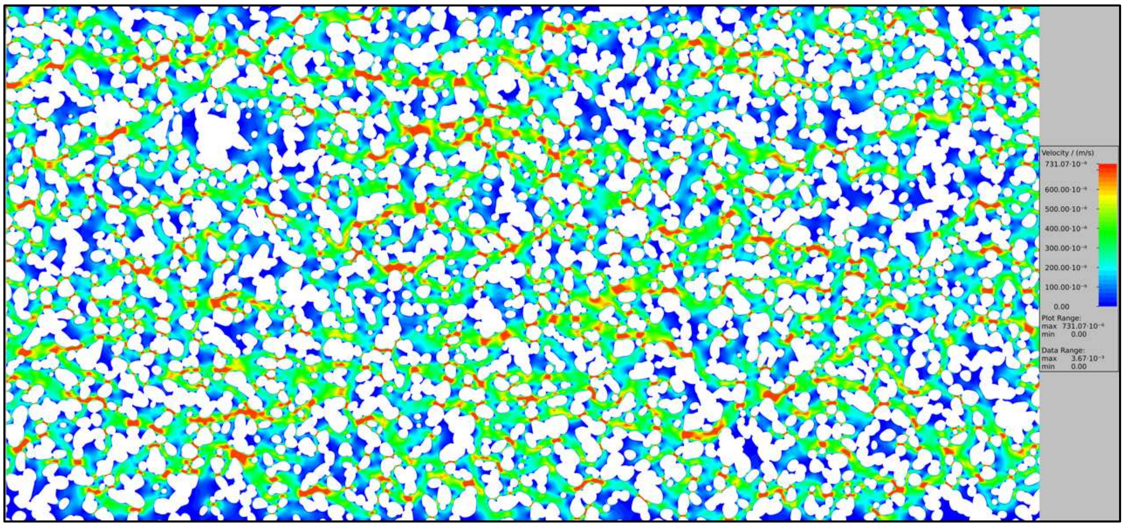

Figure 40: Velocity field of the empty domain – Slice 7.

In contrast to that, Figure 41 shows the stress field of the ED (slice 7). As described before, slices towards the edges show higher stress values, but this stress field represents a slice in the center of the depth profile (depicted in Figure 39), where lower stress magnitudes are displayed.

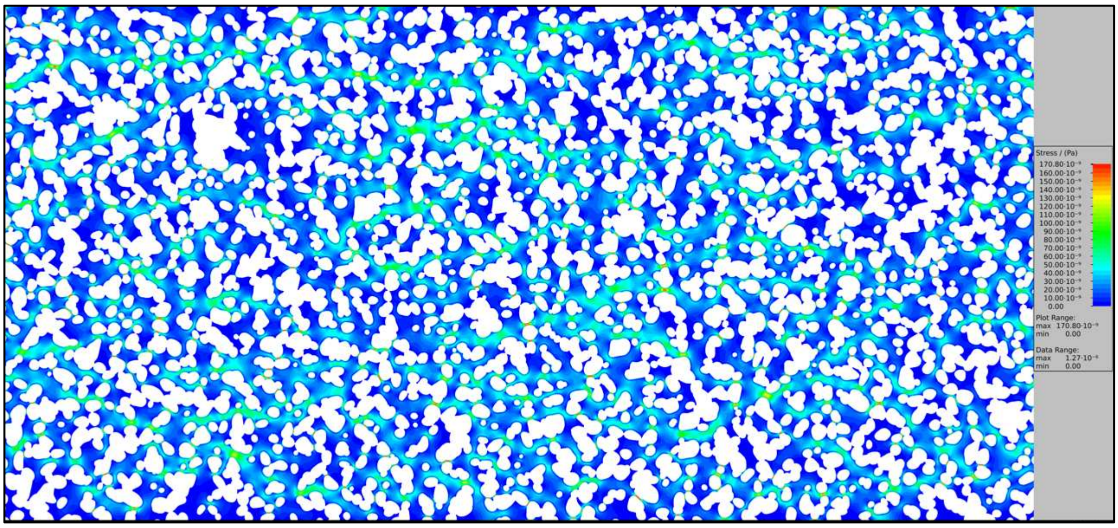

Figure 41: Stress field of the empty domain – Slice 7.

4.3.2 Impact of curvature on the empty domain

Implementing the curvature was essential to enhance the numerical setup to a more realistic scenario in the lab. Figure 42 compares the model without and with curvature in the histograms. The two subplots on the left describe the distribution of the velocities and the two subplots on the right show the stress distributions within the modeled domains.

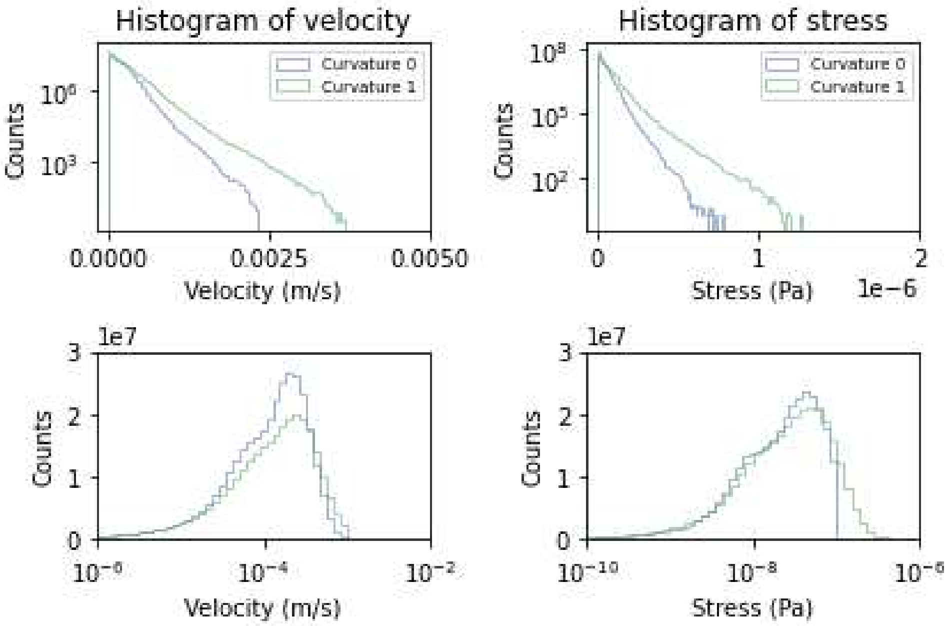

Figure 42: Impact on the flow fields by including a curvature. The simulated domain is an empty model with an injection rate of 0,05 ml/h. Curvature 0 – ED without a curvature. Curvature 1 – ED with implemented curvature.

The impact of the curvature on velocity and stress distribution simulation results cannot be neglected to match the actual experimental MM setup. The effect of implementation is visualized in Figure 42. Higher velocities and shear stresses occur due to the curved elements in the simulation model. Table 10 shows the increase from the maximum velocity and stress in comparison. Nevertheless, the consideration increased the span from minimum to maximum for both variables.

Table 10: Impact of curvature - Data table of min. and max. values of velocity and stress.

Description	**Min. Velocity [m/s]**	**Max. Velocity [m/s]**	**Min. Stress [Pa]**	**Max. Stress [Pa]**
Curvature 0	2,16E-11	2,30E-03	7,68E-15	7,82E-07
Curvature 1	1,64E-11	3,67E-03	5,86E-15	1,27E-06

4.3.3 Comparison of injection flow rates

The main distinction between the two experimental series is the injection flow rate. Experiment 1 has a flow rate of 0,2 ml/h and experiment 2 has a flow rate of 0,05 ml/h, respectively. The influence of increasing the injection rate by four times can be seen in Figure 43. As expected, the higher flow rate increases the velocity and, therefore, the share rates. The width of the velocity and stress histograms for Exp. 1 are extended four times compared to Exp. 2. Hence, the domain covers higher velocities, which occur more often in the model. When the peak of the plots is analyzed in further detail (lower row of Figure 43), a shift to the left can be seen in both scenarios. This underlines the previous statement that lower velocity and stress numbers can be found in experiment 2 with the lowered injection rate.

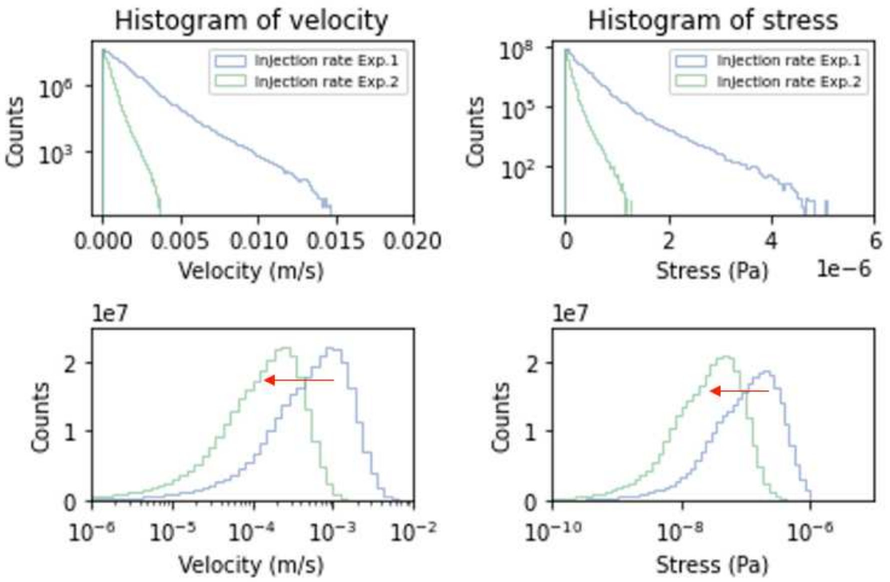

Figure 43: Comparison between injection flow rates: Exp. 1 (0,2 ml/h) vs. Exp. 2 (0,05 ml/h).

Table 11 gives a numerical overview of the comparison of the injection rates, displaying the min. and max values of velocity and shear stress.

Table 11: Comparison of injection flow rates - Data table of min. and max. values of velocity and stress.

Description	**Min. Velocity [m/s]**	**Max. Velocity [m/s]**	**Min. Stress [Pa]**	**Max. Stress [Pa]**
Injection rate Exp. 1	6,57E-11	1,47E-02	2,34E-14	5,07E-6
Injection rate Exp. 2	1,64E-11	3,67E-03	5,86E-15	1,27E-6

4.3.4 Histogram analysis of experiment 1

The following should describe the outcome of the simulation results from Exp. 1. Figure 44 shows four timesteps of experiment 1, which were simulated with an injection rate of 0,2 ml/h. Timestep 0 is the start of the experiment, represented by the empty domain model without any biomass accumulation. The subsequent timesteps correspond to the first timestep (after one h) and last timestep (after 48 h) and an arbitrary timestep in the middle (24 h). The selected biomass permeability is 100 mD and is a result of the previous investigations.

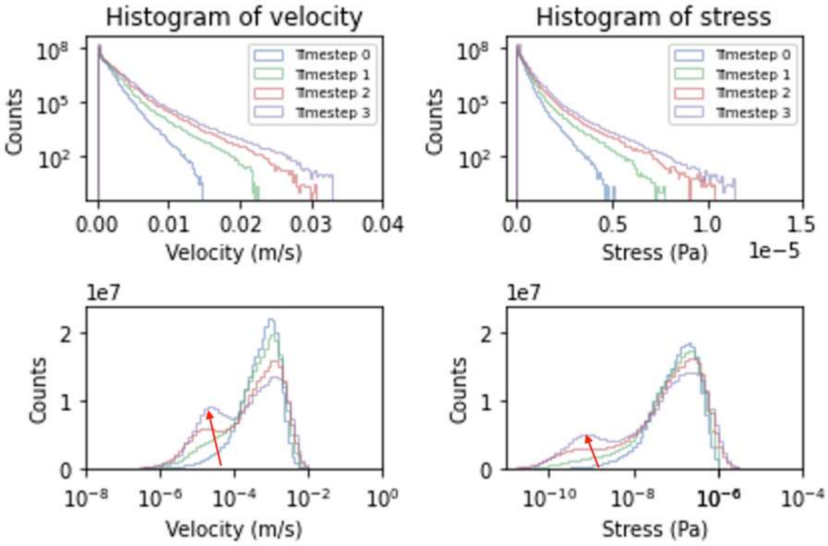

Figure 44: Experiment 1 - Velocity and stress histograms over time with a simulated biomass permeability of 100 mD. Timestep 0 – Empty domain (no biomass). Timestep 1 – Simulation after 1 h. Timestep 2 – Simulation after 24 h. Timestep 3 – Simulation after 48 h.

An increase in the width of the histograms can be seen, which implies a higher velocity with time. Pore throats get narrowed by biomass accumulation and hence the velocity and stress values increase in the domain. Furthermore, with a closer look at the peak at the beginning of the plots, a dual distribution of the velocity/stress distributions, which develops over time, can be obtained. It might be that these velocities, or stresses respectively, are created due to the biomass since, in the first timesteps, none of these exists. The line color of the various timesteps is not correlated with velocity or stress magnitudes in the upcoming flow fields.

Table 12: Experiment 1 (comparison over time) - Data table of min. and max. values of velocity and stress.

Description	**Min. Velocity [m/s]**	**Max. Velocity [m/s]**	**Min. Stress [Pa]**	**Max. Stress [Pa]**
Timestep 0	6,57E-11	1,47E-02	2,34E-14	5,07E-6
Timestep 1	3,79E-12	2,24E-02	1,35E-15	7,73E-6
Timestep 2	4,49E-12	3,06E-02	3,20E-15	1,04E-5
Timestep 3	6,01E-12	3,30E-02	4,25E-15	1,14E-5

Table 12 shows a data summary of the minimum and maximum values of velocity and stress. The min. value for velocity and shear stress decreases over time, but simultaneously the maximums are increasing, as shown in Figure 44.

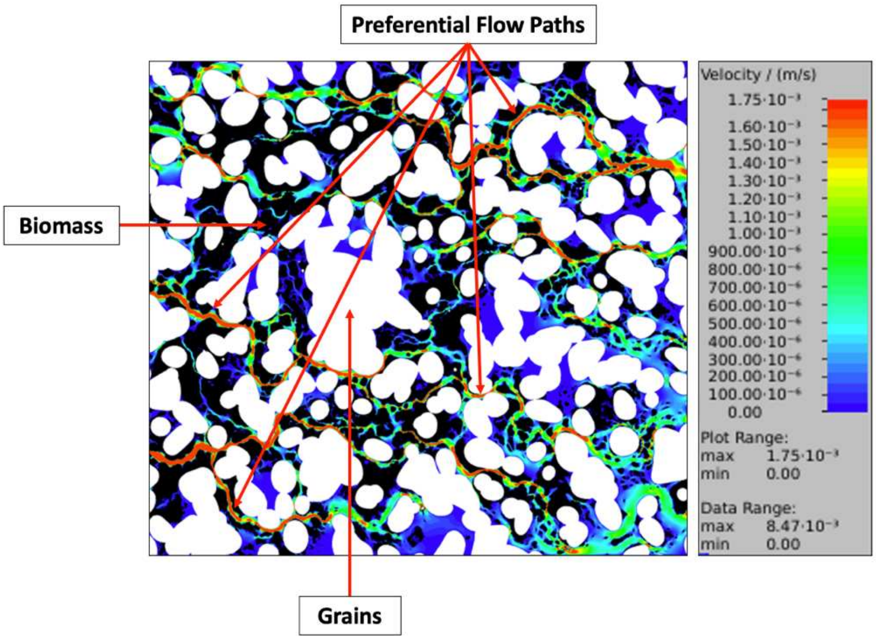

Figure 45: Illustration of velocity field including color legend

Figure 45 illustrates an arbitrary location in a velocity field, including a color legend. Grains (white areas) and biomass (black spots) are highlighted with an arrow. The magnitude of the shown variable, either velocity or stress, is visualized by the following color code: blue colors show spots of zero velocity/stress, increasing magnitudes are represented via green, or turquoise colors and areas with the highest variable amplitudes are depicted in red colors. The color code is congruent for shear stress fields. Further, preferential flow paths can be detected by ongoing connections of high variable magnitudes through the porous media. Figure 45 also highlights several preferential flow paths in this exemplary velocity field.

Figure 46 and Figure 47 show slice number seven of the velocity/stress field changes over time. The increased biomass, as well as the establishment of preferential flow paths, can be seen by observed. The biomass distribution of experiment 1 occurs very homogenously over the total domain in the horizontal and vertical directions.

Timestep 0 – Empty domain

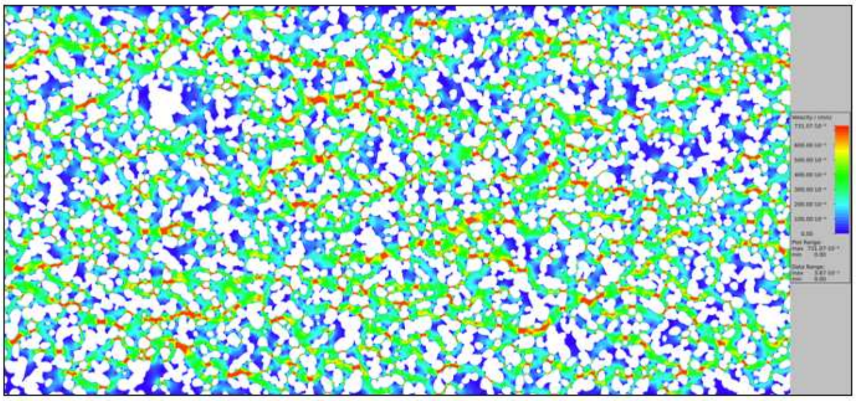

Timestep 1 – Simulation after 1 h

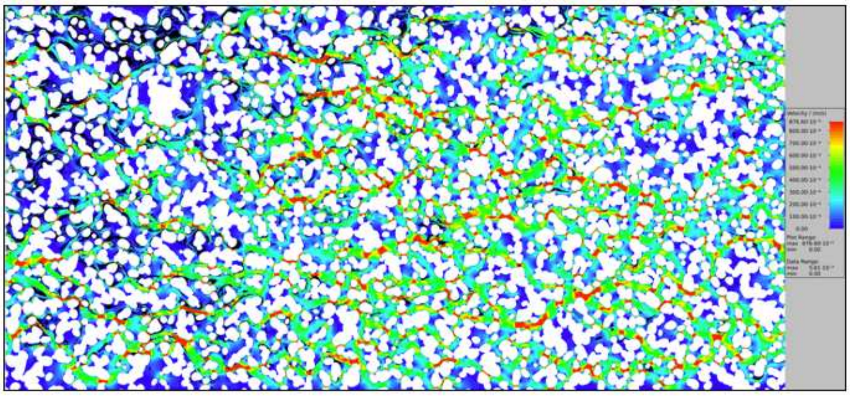

Timestep 2 – Simulation after 24 h

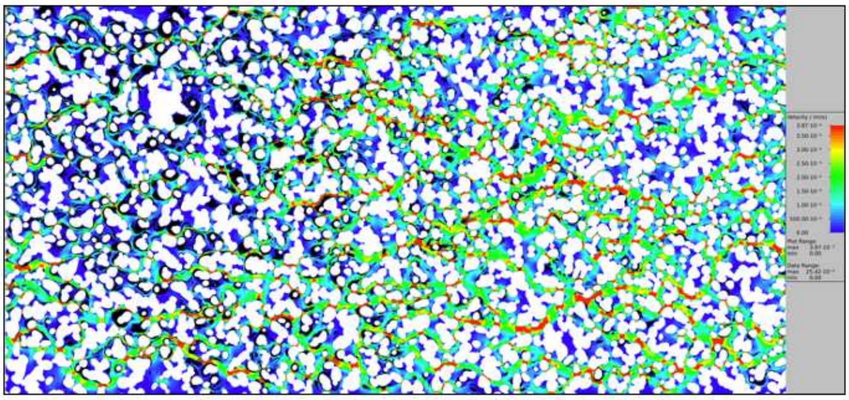

Timestep 3 – Simulation after 48 h

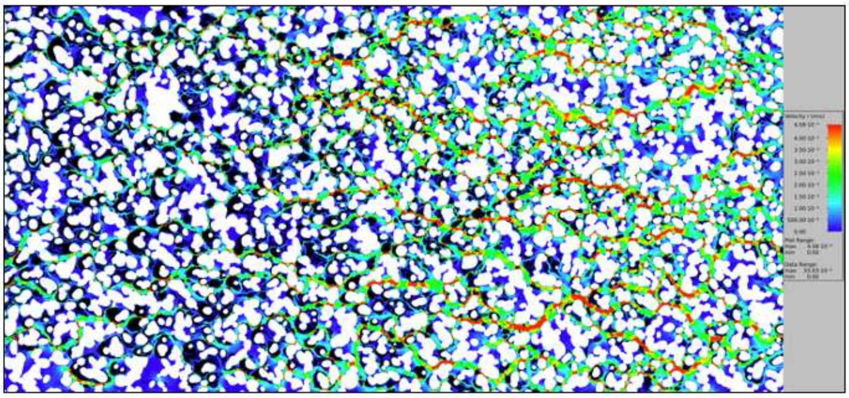

Figure 46: Velocity field Experiment 1 – Time series.

Timestep 0 – Empty domain

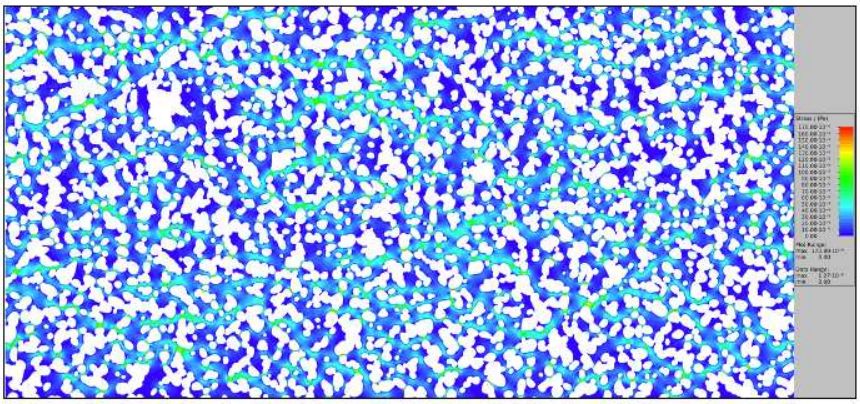

Timestep 1 – Simulation after 1 h

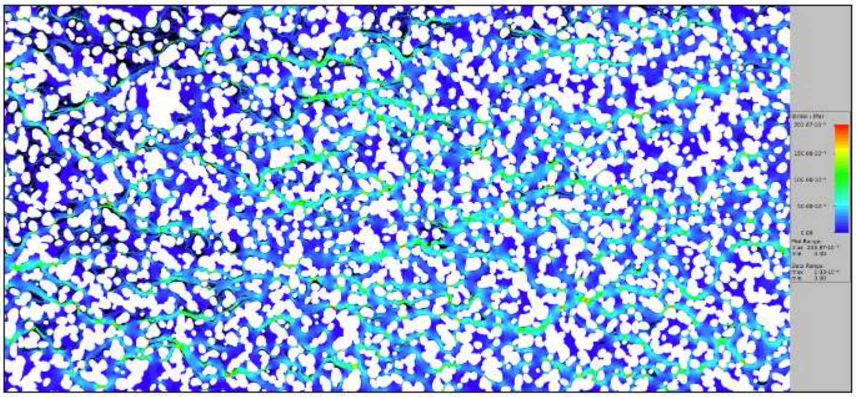

Timestep 2 – Simulation after 24 h

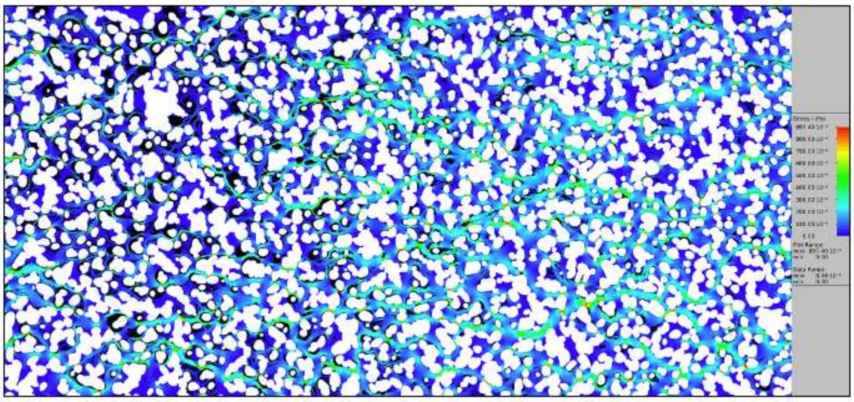

Timestep 3 – Simulation after 48 h

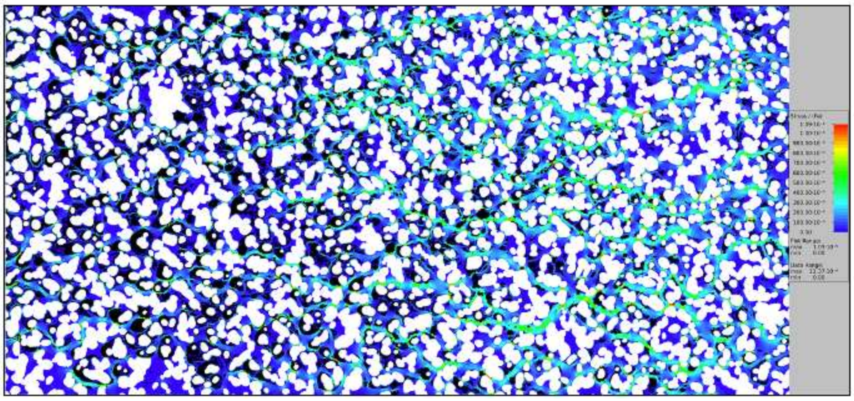

Figure 47: Stress field Experiment 1 – Time series.

The upcoming plot section (Figure 48) shows the comparison of varied biomass intra-permeabilities of the last timestep of Exp.1. Depicted biomass permeabilities are 0 mD (Permeability 3), 100 mD (Permeability 2) and 500 mD (Permeability 1). Permeability 0 is the ED without biomass as a reference.

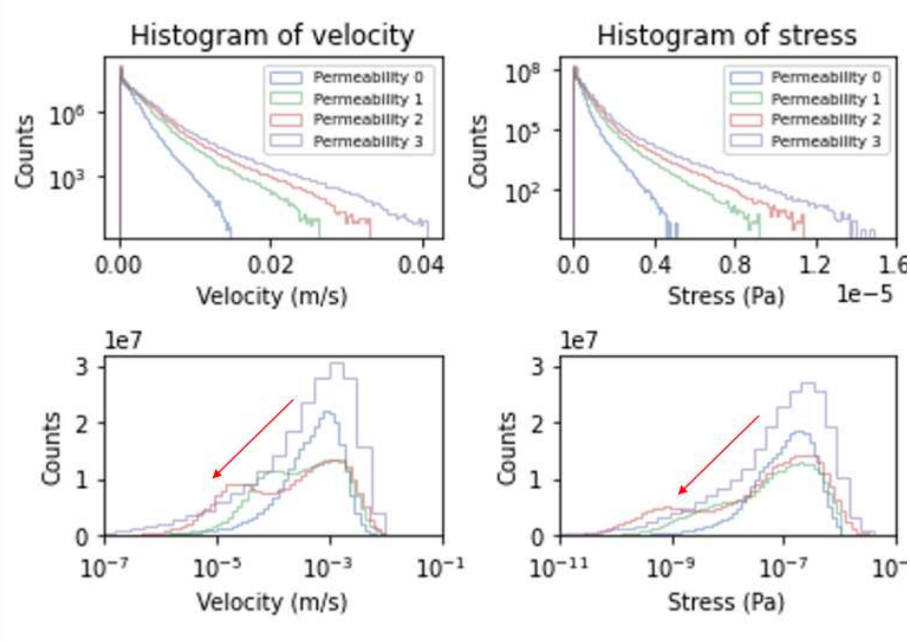

Figure 48: Experiment 1 – Comparison of velocity and stress histograms with different biomass permeabilities after 48 h. Permeability 0 – Empty domain (no biomass). Permeability 1 – 500 mD biomass permeability. Permeability 2 –100 mD biomass permeability. Permeability 3 – 0 mD biomass permeability.

It can be said that, with decreasing biomass permeability, the velocity/stress numbers increase, as shown in Figure 48 and Table 13. The bimodal configuration can be again detected and the degree of the peculiarity of the bimodal distribution is determined by biomass intra-permeability. The lower the permeability of the biomass, the more the bimodal configuration is pronounced. The case with zero biomass permeability (Permeability 3) does not follow any specific behavior and can be compared to the ED case (Permeability 0), except for the shift to higher numbers.

Table 13: Experiment 1 (comparison of permeability) - Data table of min. and max. values of velocity and stress.

Description	**Min. Velocity [m/s]**	**Max. Velocity [m/s]**	**Min. Stress [Pa]**	**Max. Stress [Pa]**
Permeability 0	6,57E-11	1,47E-02	2,34E-14	5,07E-06
Permeability 1	5,37E-11	2,64E-02	1,91E-14	9,11E-06
Permeability 2	6,01E-12	3,30E-02	4,25E-15	1,14E-05
Permeability 3	2,50E-27	4,06E-02	3,77E-26	1,48E-05

4.3.5 Histogram analysis of experiment 2

The following should describe the outcome of the simulation results from Exp. 2. Figure 49 shows the results of experiment 2 (biomass permeability: 125 mD) over time and it also depicts four timesteps, which were simulated with a lowered injection rate of 0,05 ml/h, compared to Exp. 1. Timestep 0 is referred to the start of the experiment, represented by the empty domain model without any biomass accumulation. The subsequent timesteps correspond to the first timestep (after one h) and last timestep (after 60 h) and an arbitrary timestep in the middle (40 h). The typical bimodal behavior establishes over time as in Exp. 1 obtained.

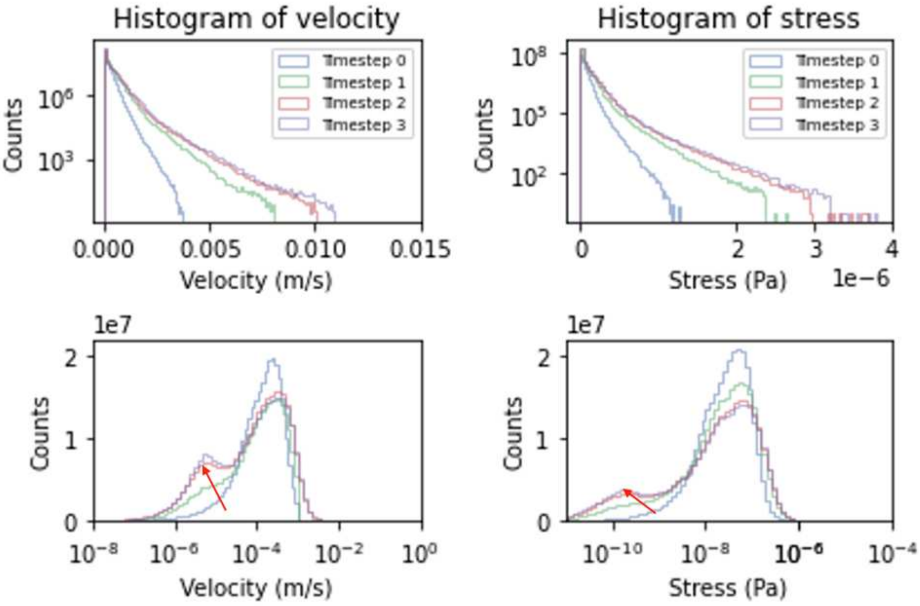

Figure 49: Experiment 2 - Velocity and stress histograms over time with a simulated biomass permeability of 125 mD. Timestep 0 – Empty domain (no biomass). Timestep 1 – Simulation after 1 h. Timestep 2 – Simulation after 40 h. Timestep 3 – Simulation after 60 h.

Table 14 shows the data summary of the minimum and maximum values of velocity and stress.

Table 14: Experiment 2 (comparison over time) - Data table of min. and max. values of velocity and stress.

Description	**Min. Velocity [m/s]**	**Max. Velocity [m/s]**	**Min. Stress [Pa]**	**Max. Stress [Pa]**
Timestep 0	1,64E-11	3,67E-03	5,86E-15	1,27E-06
Timestep 1	1,62E-12	8,06E-03	5,78E-16	2,64E-06
Timestep 2	6,32E-13	1,00E-02	4,50E-16	3,67E-06
Timestep 3	2,87E-13	1,09E-02	1,02E-16	3,79E-06

Figure 50 and Figure 51 show slice number seven of the velocity and stress field changes over time. In contrast to Exp. 1, the biomass distribution of Exp. 2 is limited to the entry area of the domain and the spreading of the microbe’s volume looks more heterogeneous.

Timestep 0 – Empty domain

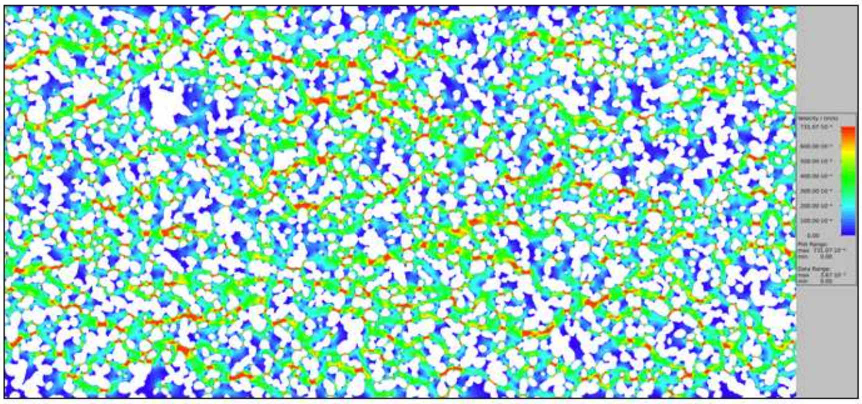

Timestep 1 – Simulation after 1 h

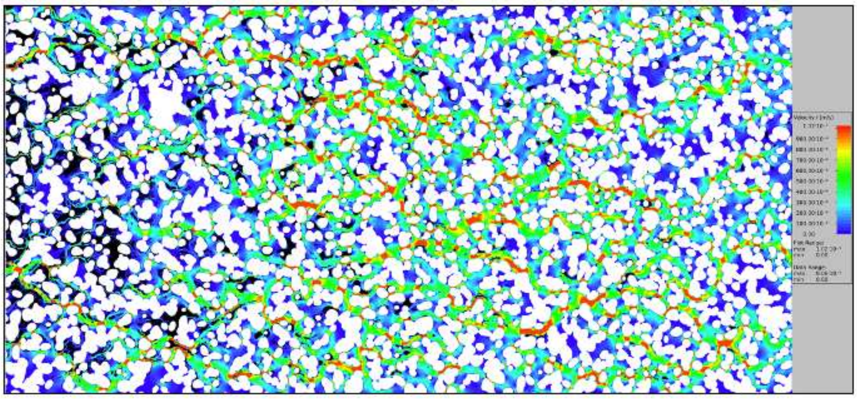

Timestep 2 – Simulation after 40 h

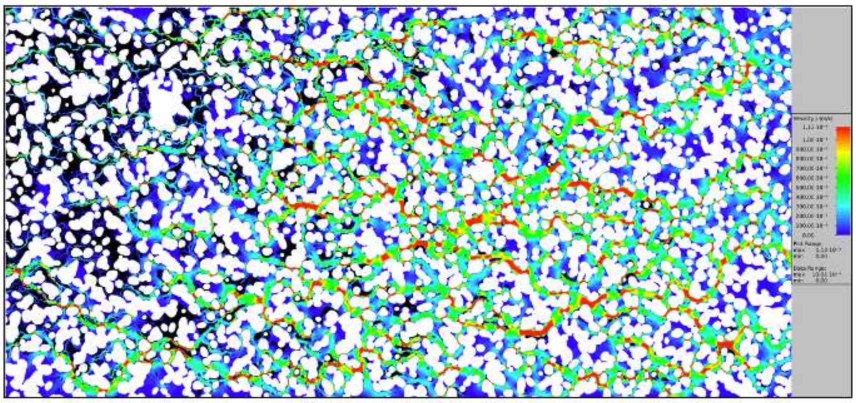

Timestep 3 – Simulation after 60 h

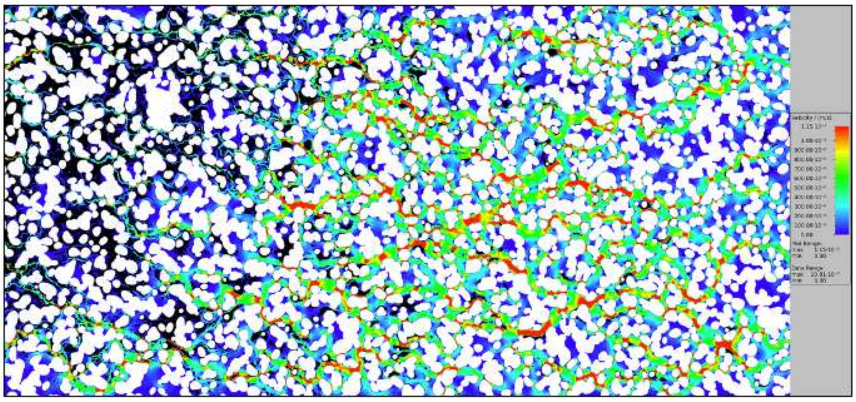

Figure 50: Velocity field Experiment 2 – Time series.

Timestep 0 – Empty domain

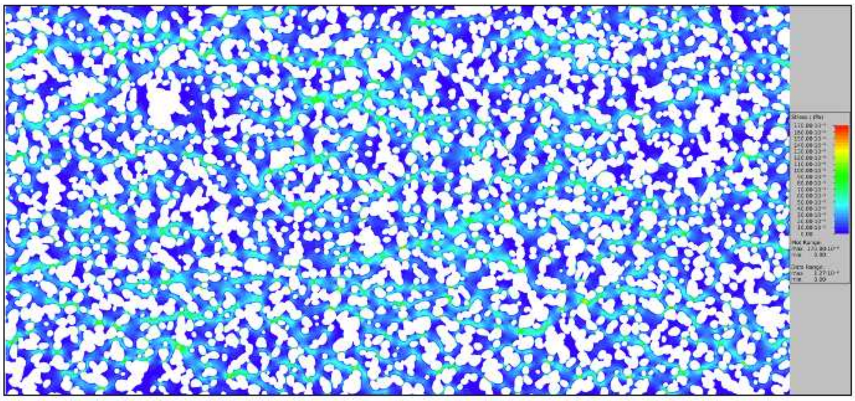

Timestep 1 – Simulation after 1 h

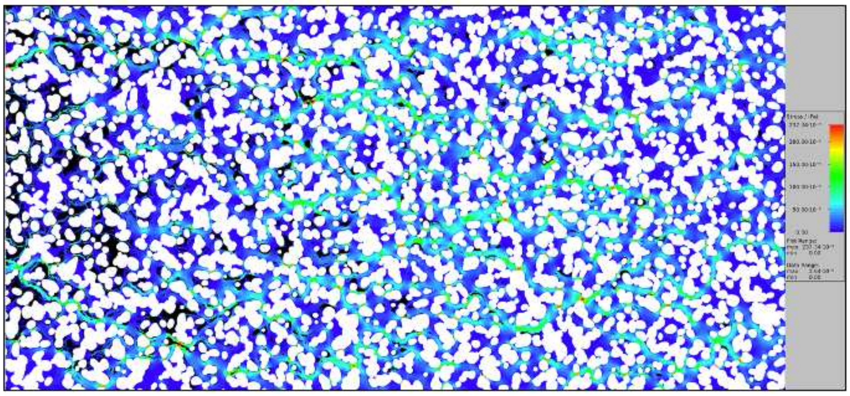

Timestep 2 – Simulation after 40 h

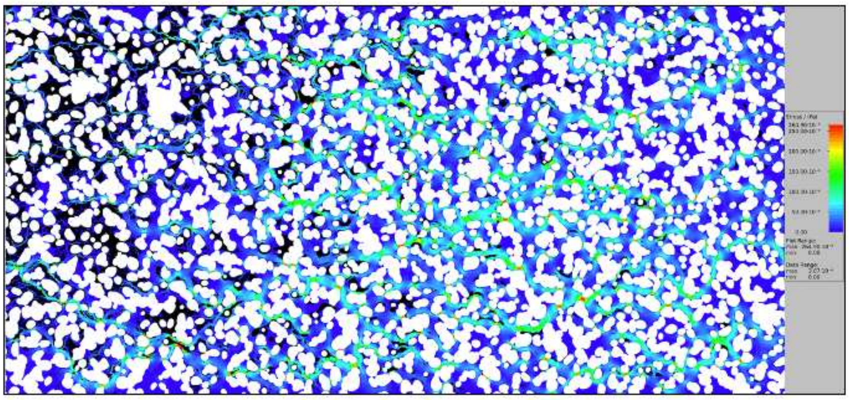

Timestep 3 – Simulation after 60 h

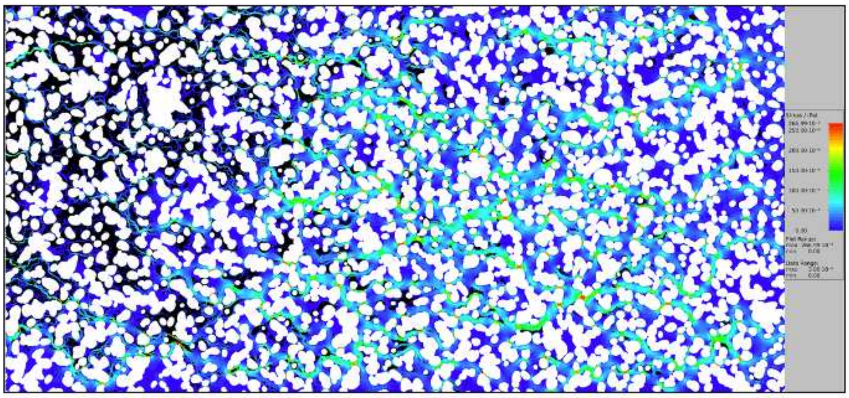

Figure 51: Stress field Experiment 2 – Time series.

Figure 52 shows the comparison of varied biomass intra-permeabilities of the last timestep of Exp.2. Depicted biomass permeabilities are 0 mD (Permeability 3), 125 mD (Permeability 2) and 500 mD (Permeability 1). Permeability 0 is the ED without biomass as a reference.

As expected and described for Exp. 1, the velocity/stress numbers increase with decreasing biomass permeability. This statement is further underlined by Table 15. The bimodal configuration can be detected and the degree of the peculiarity of the bimodal distribution is determined by intra-biomass permeability. The case with zero biomass permeability (Permeability 3) does not follow any specific behavior and can be compared to the ED case (Permeability 0), except for the shift to higher numbers.

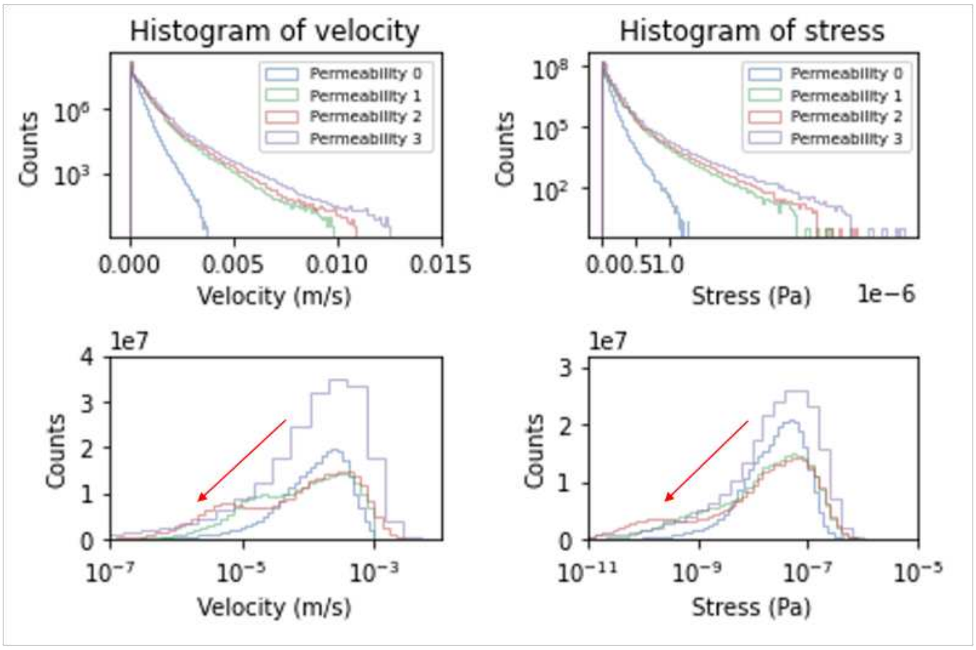

Figure 52: Experiment 2 – Comparison of velocity and stress histograms with different biomass permeabilities after 60 h. Permeability 0 – Empty domain (no biomass). Permeability 1 – 500 mD biomass permeability. Permeability 2 –125 mD biomass permeability. Permeability 3 – 0 mD biomass permeability.

Table 15 shows the data summary of the minimum and maximum values of velocity and stress of experiment 2.

Table 15: Experiment 2 (comparison of permeability) - Data table of min. and max. values of velocity and stress.

Description	Min. Velocity [m/s]	Max. Velocity [m/s]	Min. Stress [Pa]	Max. Stress [Pa]
Permeability 0	1,64E-11	3,67E-03	5,86E-15	1,27E-06
Permeability 1	6,83E-13	9,79E-03	2,45E-16	3,41E-06
Permeability 2	2,87E-13	1,09E-02	1,02E-16	3,79E-06
Permeability 3	3,197E-30	1,26E-02	2,67E-26	4,49E-06

4.3.6 Regions of interest – ROI

This chapter shows potential for future work and investigations. It deals with the analysis of two regions of interest. The ROIs are selected to investigate biomass-induced effects in more detail. Figure 53 locates the selected ROIs. ROI 1 is in the near injector region, which expects high biomass accumulations and ROI 2 adjudges at the end of the model, where a minor amount of biomass is located.

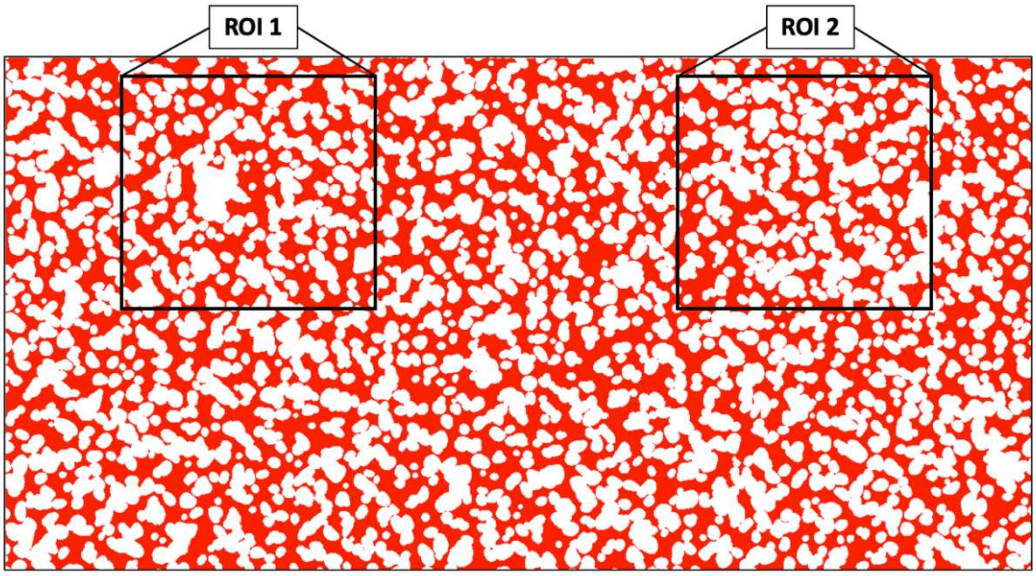

Figure 53: Empty domain showing the locations of ROI 1 and ROI 2.

Figure 54 displays the velocity and stress fields of the empty domains of the ROIs (top row) and the images after 60 h at an injection rate of 0,05 ml/h (bottom row). On the left is the velocity field and on the right, the stress field is depicted. The plugging of pore throats due to biomass accumulation can be seen and the pore throats are significantly reduced, leading to reduced porosity. Flow paths in the ED still exist in the image after 60 h, but new preferential flow paths are also established.

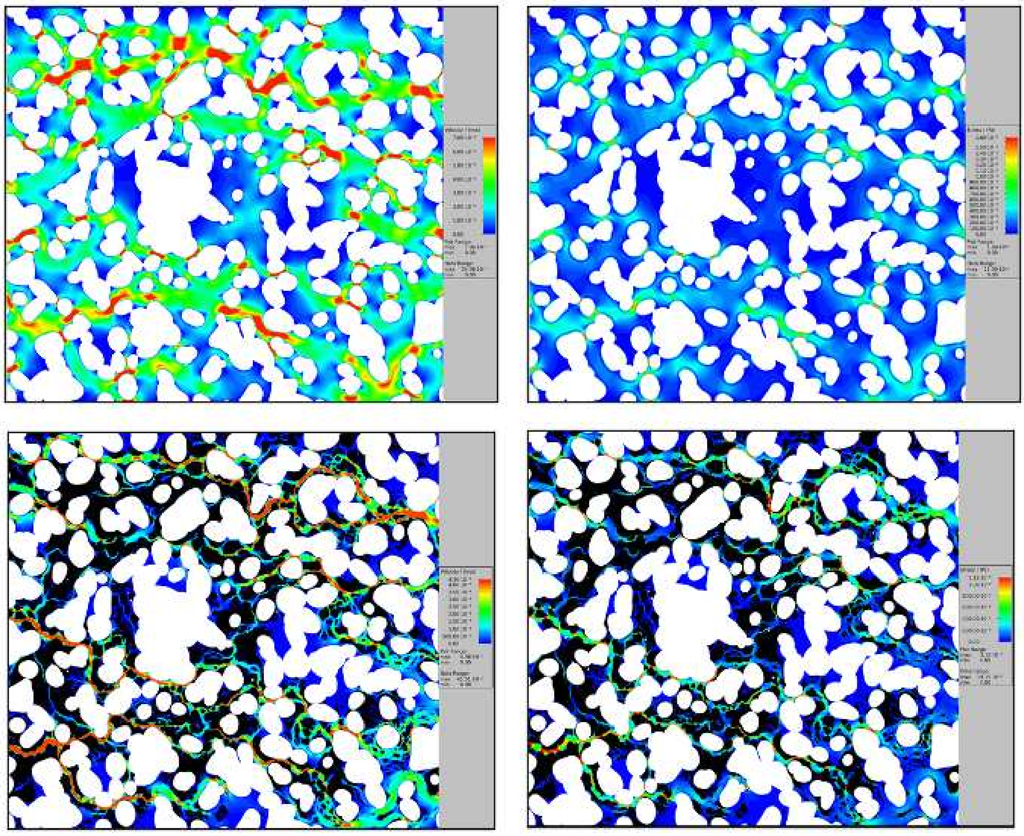

Figure 54: ROI 1 - Velocity and stress fields at an injection rate of 0,05 ml/h. Top-left: Velocity field of ED. Bottom-left: Velocity field after 60 h. Top-right: Stress field of ED. Bottom-right: Stress field after 60 h.

Figure 55 depicts the histogram analysis of the two timesteps. As awaited, timestep 1 (after 60 h) shows a widened histogram, leading to an increased number of higher velocities and stresses. Moreover, the bimodal distribution establishes compared to the starting domain.

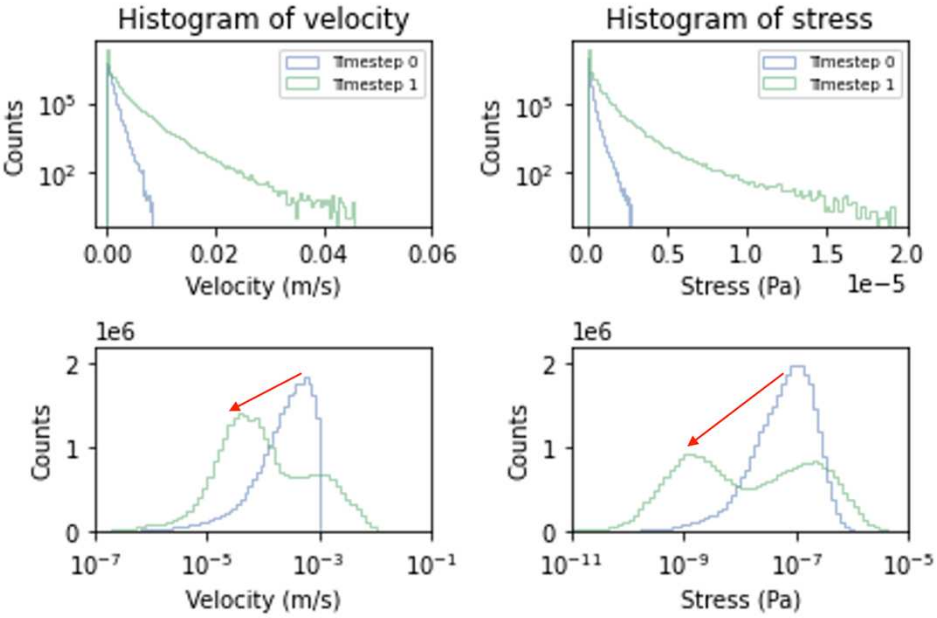

Figure 55: ROI 1 - Velocity and stress histograms over time with a simulated biomass permeability of 125 mD and injection rate of 0,05 ml/h. Timestep 0 – Empty domain (no biomass). Timestep 1 – Simulation after 60 h.

Table 16 shows a data summary of ROI 1 of the minimum and maximum values of velocity and stress.

Table 16: ROI 1 - Data table of min. and max. values of velocity and stress.

Description	**Min. Velocity [m/s]**	**Max. Velocity [m/s]**	**Min. Stress [Pa]**	**Max. Stress [Pa]**
Timestep 0	1,82E-10	8,50E-03	6,48E-14	2,81E-06
Timestep 1	7,52E-11	4,60E-02	2,68E-14	1,91E-05

Table 17 summarize the simulation results of ROI 1 and ROI 2. It shows that the porosity decreases massively after time in ROI 1, combined with a massive loss of permeability. ROI 2 points out a contrary situation, where porosity stays almost unaffected and permeability decreases by only 1,00 D.

Table 17: Simulation results of ROI 1 and ROI 2.

Description		**Permeability**	**Porosity**
ROI 1	At start	3,44 D	46,98 %
	After 60 h	0,39 D	22,25 %
ROI 2	At start	2,61 D	45,83 %
	After 60 h	1,61 D	41,00 %

In comparison, Figure 56 reveals a section on the right side of the total domain, where a minor amount of biomass was accumulated. The pore radius stayed unaffected and no biofilms on the pore walls could be detected, hence no significant induced reduction in porosity and permeability. The biomass aggregates in clumps, which might be an effect of lower velocities and stresses. Nevertheless, the PFPs developed intensively over time.

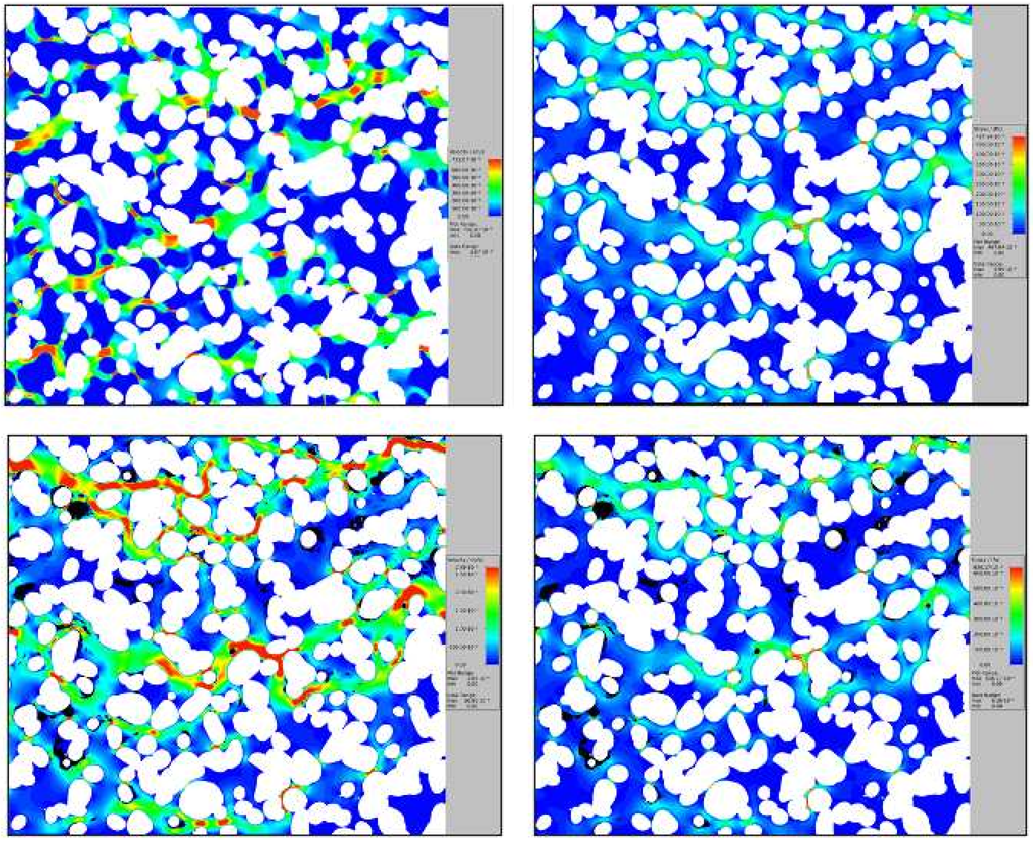

Figure 56: ROI 2 - Velocity and stress fields at an injection rate of 0,05 ml/h. Top-left: Velocity field of ED. Bottom-left: Velocity field after 60 h. Top-right: Stress field of ED. Bottom-right: Stress field after 60 h.

The histogram analysis for ROI 2 in Figure 57 shows fewer velocity and stress values than in ROI 1. This can be explained due the low development of biomass accumulations. Therefore, in the peak analysis, no biomass-induced effect of bimodal establishment occurs.

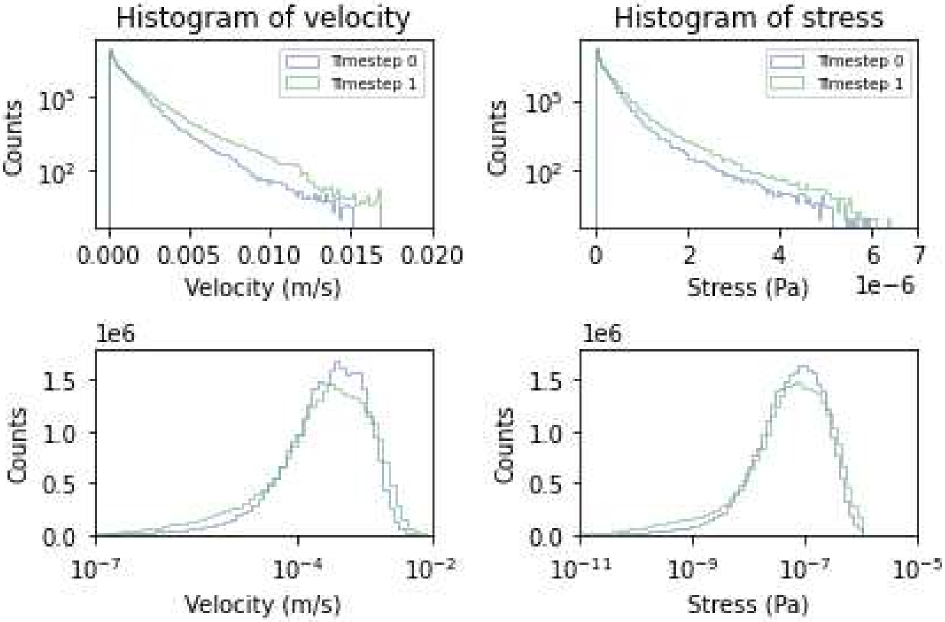

Figure 57: ROI 2 - Velocity and stress histograms over time with a simulated biomass permeability of 125 mD and injection rate of 0,05 ml/h. Timestep 0 – Empty domain (no biomass). Timestep 1 – Simulation after 60 h.

Table 18 shows the data summary ROI 2 of the minimum and maximum values of velocity and stress.

Table 18: ROI 2 - Data table of min. and max. values of velocity and stress.

Description	Min. Velocity [m/s]	Max. Velocity [m/s]	Min. Stress [Pa]	Max. Stress [Pa]
Timestep 0	1,01E-10	1,15E-02	3,61E-14	5,95E-06
Timestep 1	1,11E-11	1,68E-02	3,96E-15	6,39E-06

4.4 Heterogeneity analysis

The simulation model was analyzed due to its heterogeneity in the variable's permeability and porosity. The interest was to examine whether a small elementary volume could represent the total domain. The methodology of how the analysis was conducted is described in Chapter 3 (Figure 28 and Table 5). Figure 58 illustrates the heterogeneity analysis of the ED. The correction factor (~ 1 D) were applied to the simulation permeability outcomes, as described in previous chapters. The domain size increase from left to right. The blue line shows permeability and the red line shows porosity. Furthermore, a confidence interval of 5 % is included. If the variable enters the confidence interval, the specific model size can be defined as a representative elementary volume of the entire domain.

The permeability and porosity reduce from step to step until 100% of the domain size is reached. Except the 8 % domain does not follow this trend. The permeability enters the confidence interval in approximately 80 % of the total domain size. Hence, it can be said that 80 % of the domain size is representative of the entire model. Whereas for porosity, the representative volume is about 60 % of the domain. Further on, the porosity trend faces less variance than the permeability values.

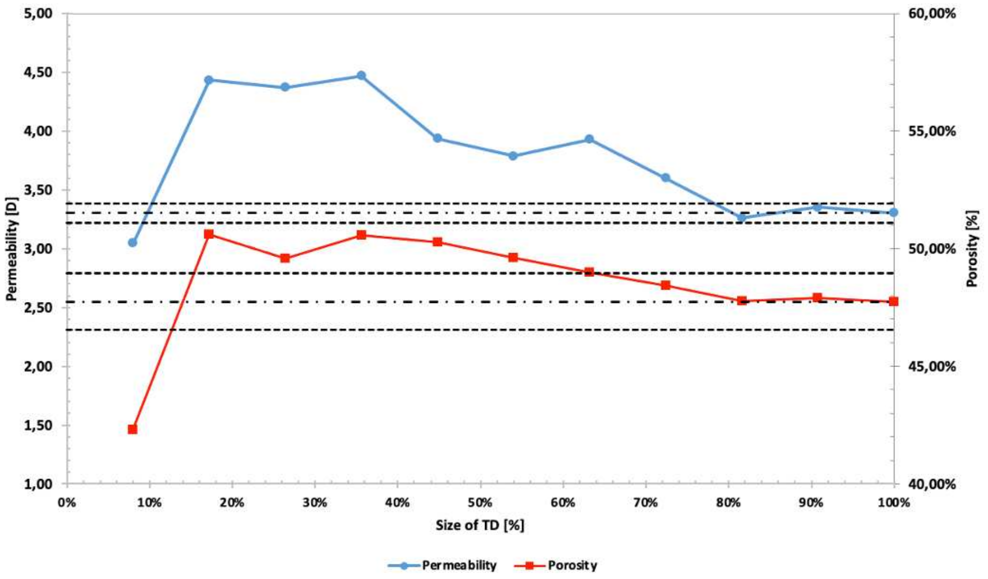

Figure 58: Heterogeneity analysis of the empty domain displaying permeability and porosity. 10 % simulation results. Black lines indicate a confidence interval of 5 %.

Figure 59 and Figure 60 display the heterogeneity analysis of Exp. 1 and Exp. 2. In both plots, permeability and porosity are shown in the first (after one h) and last timestep (after 48 h – Exp. 1 or 60 h – Exp. 2).

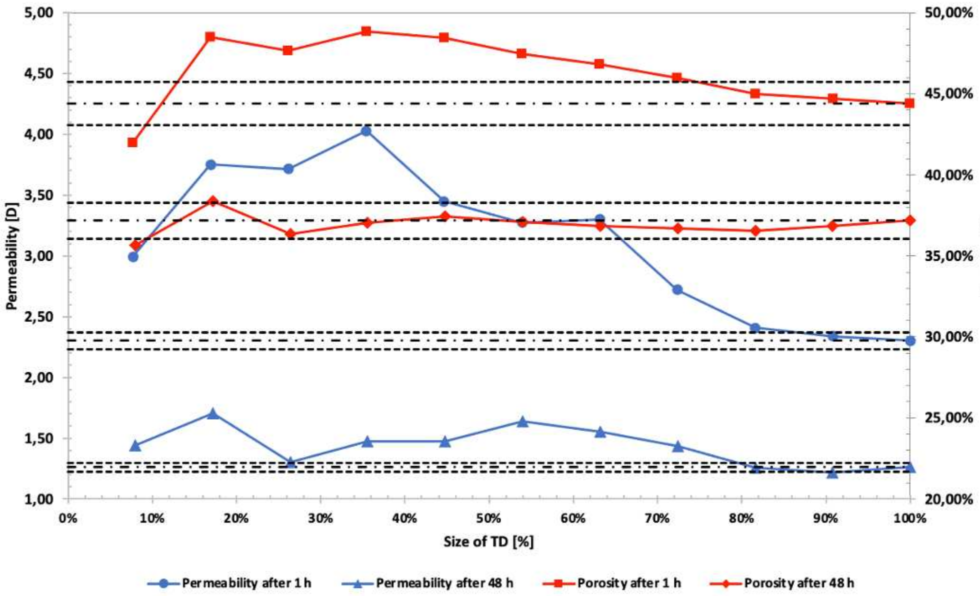

Figure 59: Experiment 1 - Heterogeneity analysis of the first (after 1 h) and last timestep (after 48 h) displaying permeability and porosity. Black lines indicate a confidence interval of 5 %.

It can be said that over time, the biomass accumulates in a way that the model decreases its heterogeneity, which is indicated by the earlier intersection into the confidence interval. In Figure 59, the REV for permeability is after one hour at 82 % and slightly evolves to 79 %. In contrast, the porosity after one hour is 78 % and after 48 h, all reduction steps of TD are in the confidence interval. Furthermore, the trends flatten and reduce the variances in the results, which is the effect of biomass accumulation.

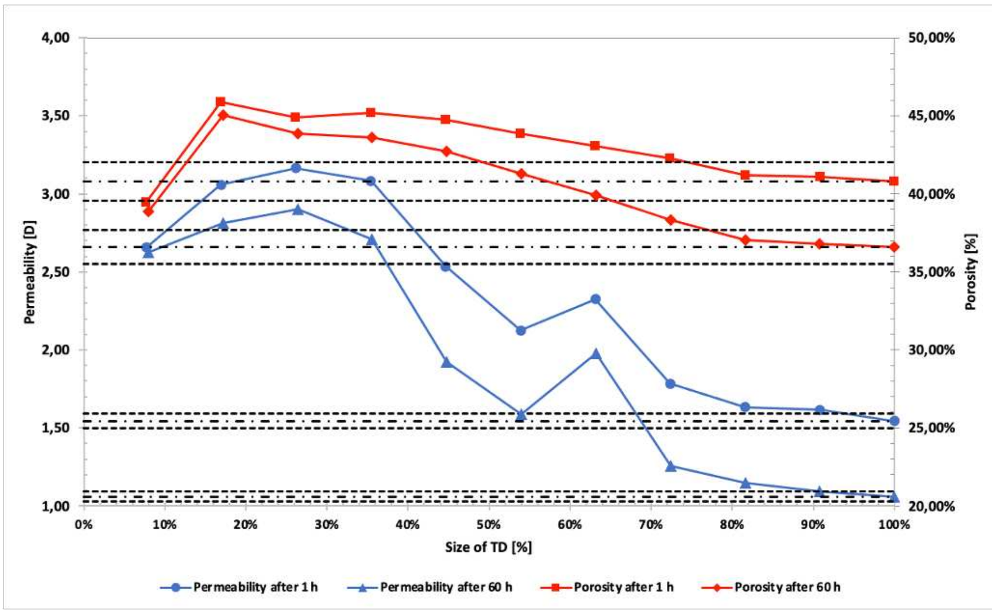

Figure 60: Experiment 2 - Heterogeneity analysis of the first (after 1 h) and last timestep (after 60 h) displaying permeability and porosity. Black lines indicate a confidence interval of 5 %.

Figure 60 computes the completely contrary results of experiment 2. The representative volume for permeability is approximately 88 % and for porosity, 78 % of TD. Both stayed the same, whether after one h or 60 h. Even the trends remain unaffected over time. The main reason might be the lowered injection rate and concomitant more heterogeneous biomass distribution as in experiment 1.

A summary of all conducted heterogeneity simulation runs over time is depicted in Figure 61 for permeability and Figure 62 for porosity. The left side shows Exp. 1, the right Exp. 2 and the upper row plots permeability, whereas the lower row refers to porosity. These plots underline the described impact of the different injection rates. On the one side, in Exp. 1, the trend flattens for permeability and porosity and on the other side, in Exp. 2, the trend stays unaffected. Moreover, the gap between the starting model (ED) and the first timestep (after one h) is more significant in Exp. 2 than in Exp. 1. Thus, the composition of the pore space also confirms this behavior. If Figure 36 and Figure 37 are compared, the biomass volume after one hour distinguishes completely.

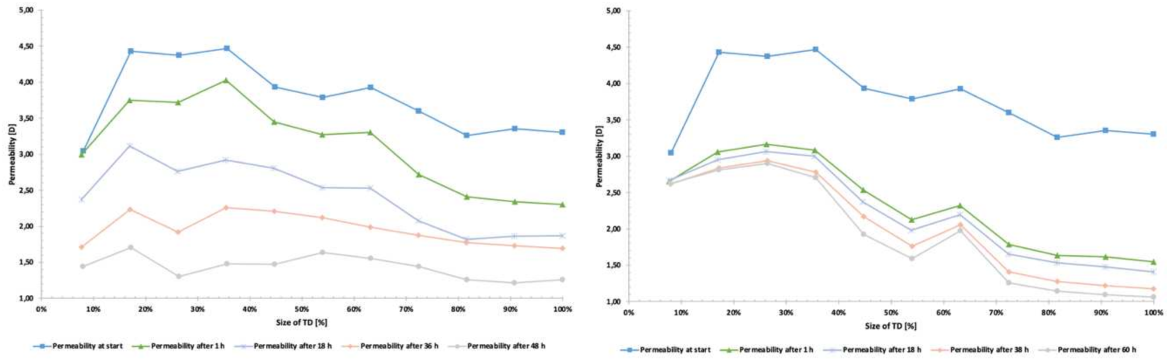

Figure 61: Heterogeneity analysis of permeability. Left – Experiment 1. Right – Experiment 2.

Representative volumes can be only found from approximately 80 % of the TD onwards. Nevertheless, significant disparities between the experiments and the varied injection flow rates can be found over time. The higher flow rates in Exp. 1 lead to more homogenous biomass settlement than is the case for the lowered injection rate in Exp. 2.

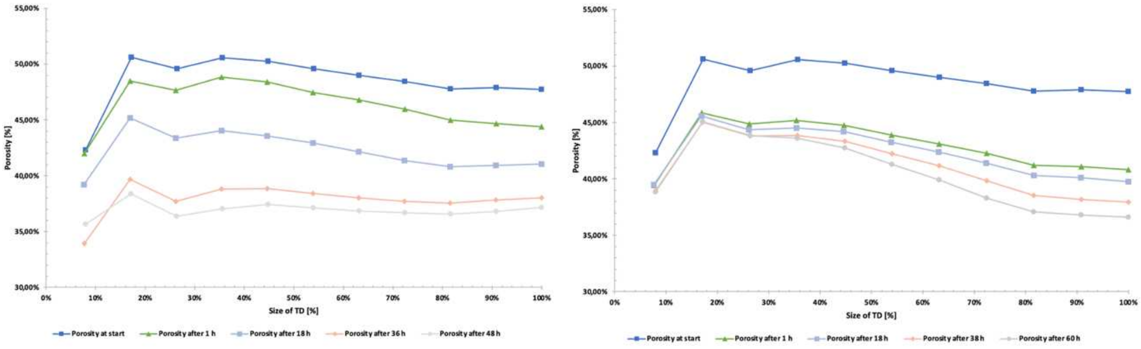

Figure 62: Heterogeneity analysis of porosity. Left – Experiment 1. Right – Experiment 2.

4.5 Discussion section

This thesis focused on enhancing the numerical model setup and matching it with experimental data. Therefore, porosity-permeability relationships were computed to compare experimental results with the simulation outcomes. The simulations were conducted mainly on the total domain, except for future work outlook, two regions of interest were investigated. Besides, different simulation settings were used until the correct domain size with an implemented curvature was found (see Chapter 3.3.8 – Simulation roadmap). The empty model was simulated with bifurcating in- and outflow channels, which decreased the overall permeability of the simulation model. Due to the adaption of the numerical setting, the simulation results require the consideration of a correction factor. The information for the introduction of a correction factor was gathered from the empty domain fitting (Table 6 and Table 7) and it consists of the consideration of channels (0,24 D), the numerical difference in error bounds (0,5 D) and a systematic graphical error from Figure 33 (0,26 D). Thus, it results in an impact of roughly 1 D, considered in the simulations, including biomass accumulations to fit the experimental ones. Based on Figure 34 and Figure 35, several biomass intra-permeabilities were used to fit the observed experimental outcome. A biomass permeability of 100 mD for Exp. 1 and 125 mD for Exp. 2 matched best and was utilized for further investigations. Figure 35 also points out a break in the trend of Exp. 2, which can be explained due to the filtration events in the domain. The microbial culture used was Methanobacterium formicicum, which is different from previous studies.

Furthermore, in Figure 34, preferential flow paths and biomass detachments can be detected due to the flattened trend of permeabilities. This can also be seen in the experimental results in Figure 31. As a result, the growth and detachment rates are equal and no further significant variances in permeability occur. Unless, in filtration events, indicated by high-pressure jumps, a considerable amount of biomass is detached from an accumulation. Filtration events also reveal that shear stresses in the flow paths are high enough to enable the detachment of accumulated biomass.

Two experiments were part of this thesis, which distinguished from each other by the injection flow rate. The higher flow rate achieved a higher growth rate of biomass and created a more homogenous biomass distribution over the entire domain, which is depicted in the heterogeneity analysis over time in Figure 61 and Figure 62. The biomass accumulation in experiment 2 is much more heterogenous, which might be induced by the lower injection rate. The critical shear stresses are reached less often, which decreases the detachment rate, leading to favored local accumulations compared to distribution over the total domain. This can be flawlessly seen in the time series of the flow fields of Exp. 1 (Figure 46 and Figure 47) and Exp. 2 (Figure 50 and Figure 51). It can be stated that decreasing velocity in the flow channels favors heterogeneous biomass distribution.

The influence of injection flow rates on hydraulic simulation outcomes was marginal compared to pressure drop input. Still, the velocity and stress fields were susceptible to it and exhibited an increase by a factor of four, which can be captured in Figure 43. Therefore, different velocity and shear stresses occur in the domain and the growth and biomass accumulation get impacted differently. In general, both experiments faced an enlargement of the width of the histograms, which means an increase in velocity and shear stress over time due to pore throats accumulations by biofilms. Furthermore, a shift to the left in the increased injection rate scenario is visible. As the simulation outcomes represent, biomass accumulations decrease the permeability and porosity of the micro model over time. The statement of Thullner (2008) that in a constant flux system, narrower pore throats lead to increased flow velocities and consequently, higher shear stresses can be confirmed.

The ROI investigations show different kinds of accumulation types of biomasses. The biomass gathers as stream tracers in high permeable sections, accompanied by high velocities and stresses. It tends to form layers and accumulations around the grains and the biomass settles within a preferential flow path, which promotes channelization (Figure 54). Thus, Table 17 underlines the massive reduction in permeability and porosity. While Figure 56 displays a region with lower permeability and therefore, lower velocity and stress magnitudes. In this region of interest, the biomass aggregates as clumps and hence, the impact due to the hydraulic properties is reduced to a minor extent. The resulting shapes of the biomass aggregates are also a function of viscous dissipation, the loss of energy from the pore fluid to the biomass.

The velocity and stress distribution at the beginning of the histograms are also noteworthy, where a bimodal configuration establishes. This bimodal distribution starts with the onset of biomass accumulation and evolves in both experiments (Figure 44 and Figure 49). Finally, this behavior was also seen in the analysis of variation in biomass intra-permeabilities, displayed in Figure 48 and Figure 52. Both experiments showed the same behavior and the bimodal distribution did not appear for the impermeable case. The degree of peculiarity increases with reduced biomass permeability and it is best represented in the plots at a permeability of 100 mD for Exp. 1 and 125 mD for Exp. 2.

Chapter 5

Summary, Conclusion and Future Work

5.1 Summary and conclusion

The study of microbial growth and its impact on hydraulic properties is essential to establishing underground hydrogen storage and in-situ gas conversion to broader utilization. Pore-scale images in high-resolution were gathered from the experimental setup, which is part of the course of a doctoral thesis. This was the starting point of this master thesis. Therefore, this thesis uses a “Digital Twin” approach to resolve the biomass-induced effects on the porous medium by direct numerical simulations. The images were cropped and segmented based on the grey values of the raw image. As a next step, the images were uploaded to the numerical simulator GeoDict and a 3D structure was established. The model was layered (10 layers) and curvatures were implemented in the simulation domain. To match experimental results, direct numerical simulations on the TD and ROI were conducted with varied biomass intra-permeabilities. The results were compared to the observed practical outcomes in normalized reduced porosity-permeability plots.

Moreover, the flow fields of velocity and stress on TD were simulated and analyzed via histograms in further detail. A macro script with the interplay of a python script enabled the construction and comparison of different timesteps and biomass intra-permeabilities with the empty domain. Furthermore, the influence of curvature and varied injection flow rates on the simulation model was investigated. In the end, a heterogeneity analysis was done to determine if finding a representative volume for the TD is possible.

This thesis aimed to study the impact of microbial growth, with the used microbial culture M. formicicum, on the hydraulic properties using a realistic reflecting numerical model. Therefore, the numerical model was enhanced to correspond to the micro model manufacturer’s blueprint. The depth of the domain was approximated to 18,82 μm by adding layers and curvatures were implemented to the channels in the domain. Significant impacts of curvature and bifurcating in- and outflow channels can be obtained. Therefore, they were considered via a correction factor on an empty domain model since it is not possible with the current experimental setup to gather images of the channels with biomass accumulations. Further impacts, such as the numerical error (comparison of 5 % and 10 % simulations), were included in the simulation outcomes. The simulations were compared to experimentally observed results and depicted in permeability vs. time and normalized reduced porosity-permeability relation plots. Some data points showed suitable matches and especially in experiment 2, a break in the trend of permeability results can be seen that might be explained due to filtration events. The discovered biomass intra-permeability, which fitted the experiments best, was 100 mD for Exp. 1 and 125 mD for Exp. 2.

The temporal velocity and stress distributions play a significant role in biofilm reconfiguration, preferential flow path formation and intra-biomass permeability. The velocity and stress fields were analyzed using histograms and the results revealed that the net accumulation of biomass decreased the hydraulic properties following a power law. As a result, narrower pore channels led to increased velocities and shear stresses in the domain. Moreover, the width of the histograms increased over time and a bimodal distribution of the velocity and stress peaks was detected. This refers to the assumed intra-biomass permeability and is first noticed with the onset of biomass accumulation. This bimodal distribution is an indicator of flow presence in the biomass accumulations and hence, a potential for advective nutrient transport within the biomass. Bimodal configurations in the histograms were verified by comparing two distinct regions of interest.

The ROI investigations show different kinds of accumulation types of biomasses. The biomass gathers as stream tracers in high permeable sections, accompanied by high velocities and stresses. It tends to form layers and accumulations around the grains and the biomass settles within a preferential flow path. While in regions with lower permeability and therefore, lower velocity and stress magnitudes, the biomass aggregates as clumps. Hence the impact due to the hydraulic properties is reduced to a minor extent. The resulting shapes of the biomass aggregates are also a function of viscous dissipation, the loss of energy from the pore fluid to the biomass.

Furthermore, the impact of the injection flow rate on biomass settlement is decisive. According to the heterogeneity analysis, higher injection rates lead to more homogenous distributions than lowered injection rates. Higher flow rates increase the velocity and stress magnitudes and hence, the detachment rate of biomass is increased and reshuffling of biomass is of more frequent occurrence.

5.2 Future work

For potential future work, the numerical model setup can be enhanced further with the knowledge gained during this thesis. The degree of curvature of the MM influences the permeability results of the simulator. In this thesis, the curvature was averaged from 20 to ten layers, showing room for improvement in the numerical simulation setting. Furthermore, the channel effect was included via a correction factor. But the in- and outflow channels without biomass accumulations were considered since it was not possible with the current experimental setting to take images of biomass accumulated bifurcating channels. This approach can be a massive potential to enhance the numerical setup. Moreover, the Stokes-Brinkmann equations were selected due to explained reduced simulation duration. Still, in the future, the impact of including the inertia of the fluids using the Navier-Stokes-Brinkmann on the flow fields could be investigated.

The topic of ROI analysis was already broached in Chapter 4. Still, for future work, the regions of interest will be the foundation to investigate the transport mechanisms (diffusion and advection) by extracting the Peclet number and other dimensionless numbers like the Damköhler numbers. Furthermore, the velocity and stress fields analysis can be enhanced to develop a critical shear stress rate for distinct biomass accumulation settings, which might indicate when biomass detachment happens.

Finally, during the writing process of this thesis, experiments with a third phase (gas phase) were also conducted for an enhanced understanding of the conversion process. In the next phase, a numerical setup including a continuous gas phase can deliver information about the gas permeability and nutrient consumption.

References

Abdallah, W. et al. (2007) Fundamentals of Wettability. Oilfield Review.

ADAC (2022) 'Wasserstoffautos: Technik, Modelle, Tests, Tankstellen'. Available at: https://www.adac.de/verkehr/tanken-kraftstoff-antrieb/alternative-antriebe/wasserstoffauto-so-funktioniert-es/.

Ahmad, I. and Husain, F.M. (2017) Biofilms in Plant and Soil Health. Wiley Blackwell.

Ananthanarayan, R. and Paniker, C.J. (2008) Ananthanarayan and Paniker's textbook of microbiology (7th ed., repr.). Orient Longman Private Ltd.

Anderson, W. (1986) Wettability Literature Survey-Part 2:Wettability Measurement. SPE-13933-PA. Society of Petroleum Engineers.

Aufrecht, J.A. et al. (2019) Pore-scale hydrodynamics influence the spatial evolution of bacterial biofilms in a microfluidic porous network. PLoS ONE. Available at: https://doi.org/10.1371/journal.pone.0218316.

Bailey, R. (2021) 'Phases of the Bacterial Growth Curve.', ThoughtCo. Available at: thoughtco.com/bacterial-growth-curve-phases-4172692.

Barraud, N. (2007) Nitric oxide-mediated differentiation and dispersal in bacterial biofilms. School of Biotechnology and Biomolecular Sciences. The University of New South Wales, Sydney (Australia).

Batstone, D.J. et al. (2002) Anaerobic Digestion Model No.1 (ADM1). London: IWA Publishing.

Berg, S. et al. (2019) 'Ilastik: Interactive machine learning for (bio)image analysis.' Available at: https://www.ilastik.org/about.html.

Bhavishya, M. (2017) How to Develop Robust Solid Oral Dosage Forms from Conception to Post-Approval.

Bielinski, A. (2007) Numerical simulation of CO2 sequestration in geological formations. Available at: https://doi.org/10.18419/opus-252.

BP Energy Outlook (2022) BP Energy Outlook 2022.

Buchgraber, M., Kovscek, A.R. and Castanier, L.M. (2012) A Study of Microscale Gas Trapping Using Etched Silicon Micromodels.

Characklis, W.G., McFeters, G.A. and Marshall, K.C. (1990) Physiological ecology in biofilm systems. New York: New York: John Wiley & Sons, pp. 341–394.

Clement, T.P. et al. (1997) Microbial growth and transport in porous media under denitrification conditions: experiments and simulations, pp. 269–285.

Corey, A.T. and Brooks, R.H. (1964) Hydraulic Properties of Porous Media and Their Relation to Drainage Design. Colorado State University. Available at: https://doi.org/10.13031/2013.40684.

Cunningham, A.B. (1991) Influence of biofilm accumulation on porous media hydrodynamics.

Davis, J. and Updegraff, D.M. (1954) Microbiology in the petroleum industry., pp. 215–238.

Dopffel, N., Jansen, S. and Gerritse, J. (2020) Microbial side effects of underground hydrogen storage - Knowledge gaps, risks and opportunities for successful implementation.

Dr. Jawad, A. et al. (2017) Reservoir engineering handbook.

Engineering ToolBox (2008) Gases Solved in Water - Diffusion Coefficients. Available at: https://www.engineeringtoolbox.com/diffusion-coefficients-d_1404.html [Accessed 13.10.2022].

Garrison, A.T. and Huigens, R.W. (2016) Eradicating Bacterial Biofilms with Natural Products and Their Inspired Analogues that Operate Through Unique Mechanisms. Researchgate. Available at: https://www.researchgate.net/publication/311664511_Eradicating_Bacterial_Biofilms_with_Natural_Products_and_Their_Inspired_Analogues_that_Operate_Through_Unique_Mechanisms.

Gasunie - Crossing borders in energy (2022) Longread Hydrogen - What is hydrogen? Available at: https://www.theworldofhydrogen.com/gasunie/what-is-hydrogen/ (Accessed: 7 July 2022).

Gerlach, R. and Cunningham, A. (2010) Influence of Biofilms on Porous Media Hydrodynamics. In: Porous Media: Applications in Biological Systems and Biotechnology. Taylor and Francis Group. Available at: https://doi.org/10.1201/9781420065428-6.

Glover, P.W., Zadjali, I.I. and Frew, K.A. (2006) Permeability prediction from MICP and NMR using an electro-kinetic approach., p. Geophysics 71(4): F49-F60. Available at: https://doi.org/10.1190/1.2216930.

Hagemann, B. (2018) Numerical and Analytical Modeling of Gas Mixing and Bio -Reactive Transport during Underground Hydrogen Storage. Cuvillier Verlag.

Hassannayebi, N. (2019) An assessment of underground hydrogen storage: Transport, geochemistry, and bioactivity. Montanuniversity Leoben.

Hassannayebi, N. et al. (2021) Relationship Between Microbial Growth and Hydraulic Properties at the Sub-Pore Scale. Available at: https://doi.org/10.1007/s11242-021-01680-5.

Hilden, J. et al. (2021) FlowDict - User Guide: GeoDict release 2022. Math2Market GmbH. Available at: https://doi.org/10.30423/userguide.geodict2022-flowdict.

Hommel, J., Coltmann, E. and Class, H. (2018) Porosity-permeability relations for evolving pore space: a review with focus on (Bio-)geochemically altered porous media, pp. 589–629. Available at: https://doi.org/10.1007/s11242-018-1086-2.

idealhy (2013) 'Liquid Hydrogen Outline: Why liquefy hydrogen? Why IDEALHY?', Integrated Design for Efficient Advanced Liquefication of Hydrogen. Available at: https://www.idealhy.eu/index.php?page=lh2_outline.

IEA (2019) 'World total final consumption by source, 1971-2019.' Available at: https://www.iea.org/data-and-statistics/charts/world-total-final-consumption-by-source-1971-2019.

IRENA (2018) HYDROGEN FROM RENEWABLE POWER. IRENA. Available at: https://www.irena.org/-/media/Files/IRENA/Agency/Publication/2018/Sep/IRENA_Hydrogen_from_renewable_power_2018.pdf.

Jammernegg, B. (2020) The influence of microbial growth on hydraulic properties of subsurface gas storage sites and in-situ gas conversion. Master Thesis.

Jiang, G., Li, Y. and Zhang, M. (2013) Evaluation of gas wettability and its effects on fluid distribution and fluid flow in porous media. Petroleum Science.

Joseferd, R. and Mahmood, S.M. (2015) Certification of approval importance of porosity - permeability relationship in sandstone: petrophysical properties.

Kadner, R.J. and Rogers, K. (2022) Bacteria. Encyclopedia Britannica. Available at: https://www.britannica.com/science/bacteria/Physical-requirements.

Kanaani, M., Sedaee, B. and Asadian-Pakfar, M. (2022) Role of Cushion Gas on Underground Hydrogen Storage in Depleted Oil Reservoirs. Volume 45. Journal of Energy Storage. Available at: https://doi.org/10.1016/j.est.2021.103783.

Karimifard, S. et al. (2021) Modeling the impact of evolving biofilms on flow in porous media inside a microfluidic channel, p. 116536. Available at: https://doi.org/10.1016/j.watres.2020.116536.

Kogure, T. et al. (2011) Relative Permeability of Water and Supercritical CO2 System under Steady-state Flow Conditions in Porous Sandstones. Journal of Geography. Available at: https://10.5026/jgeography.120.944.

Lu, X. et al. (2020) The Brooks and Corey Capillary Pressure Model Revisited from Pore Network Simulations of Capillarity-Controlled Invasion Percolation Process. MDPI.

Maier, R.M., Pepper, I.L. and Gerba, C.P. (2009) Maier, R. M., Pepper, I. L., & Gerba, C. P. (2009). Environmental microbiology (2nd ed.). Elsevier/Academic Press.

Math2Market GmbH and Fraunhofer ITWM (2022) 'GeoDict (Standard Edition)'.

McPhee, C. and Zubizarreta, I. (2015) Developments in Petroleum Science.

Metz, B., Davidson, O. and De, C. (2005) B. Metz, O. Davidson, C. De, et al., Carbon Dioxide Capture and Storage. IPCC Special Report. IPCC Special Report, p. 208.

Meyers, R.A. (2002) Encyclopedia of physical science and technology (3rd ed.).

Micronit B.V. (2020) EOR Information - Physical Rock Network. Available at: https://store.micronit.com/eor_chip.html?_gl=1%2Ax5g4kg%2A_ga%2ANDU5MjgwNTk2LjE2NDI3NjY0MDc.%2A_ga_JGJRD2FQVG%2AMTY2NDc5NTU1OS4xMS4wLjE2NjQ3OTU1NTkuMC4wLjA.

Mohanta, T., Dutta, D. and Goel, S. (2017) Fundamentals of Microbiology. Vol. 10, pp. 301–321. Springer International Publishing.

Moore, J. and Shabani, B. (2016) A Critical Study of Stationary Energy Storage Policies in Australia in an International Context: The Role of Hydrogen and Battery Technologies. energies.

Nagib, M. (2021) 'Reservoir Engineering Fact Sheet'.

Nikolaev, D. (2020) Numerical simulation of Bio-reactive transport process: Application of underground methanation reactor. Montanuniversity Leoben.

Ott, H., Roels, S.M. and De Kloe, K. (2015) Salt precipitation due to supercritical gas injection: I. Capillary- Driven Flow in Unimodal Sandstone. Intern. J. Greenh., pp. 247–255. Available *at: https:// doi.org/10.1016/j.ijggc.2015.01.005.*

Pan, B. et al. (2021) Underground hydrogen storage: Influencing parameters and future outlook. Elsevier B.V.

Panfilov, M.B. (2016) Underground and pipeline hydrogen storage. Elsevier.

Panfilov, M.B. (2018) Physicochemical fluid dynamics in porous media: Applications in petroleum geosciences and petroleumengineering.

Parker, N. et al. (2018) Microbiology. Revision MB-2016-002(05/18)-BB. OpenStax.

RAG Austria AG (ed.) (2021) 'Shaping the future of energy', p. 61.

Rose, W. (1949) Theoretical Generalizations Leading to the Evaluation of Relative Permeability. Available at: https://doi.org/10.2118/949111-G.

Rossen, W.R. (2000) Snap-off in constricted tubes and porous media. Colloids and Surfaces. Physicochemical and Engineering Aspects. Available at: https://doi.org/10.1016/S0927-7757(99)00408-2.

Roux, E. et al. (2020) Fluid Shear Stress Sensing by the Endothelial Layer. frontiers in Physiology. Available at: https://10.3389/fphys.2020.00861.

Sandnes, M.F. (2020) Wetting Stability of Aged Limestone in the presence of HPAM polymer.

Saracco, R. (2021) Post-Pandemic Scenarios – XLI – Energy 3, IEEE Future Directions. Available at: https://cmte.ieee.org/futuredirections/2021/05/28/post-pandemic-scenarios-xxxxi-energy-3/ (Accessed: 5 July 2022).

Singh, H. (2017) Representative Elementary Volume (REV) in Spatio-Temporal Domain: A Method to Find REV for Dynamic Pores. Journal of Earth Science, pp. 391–403. Available at: https://doi.org/10.1007/s12583-017-0726-8.

Singh, H. and Srinivasan, S. (2014) Some Perspectives on Scale-Up of Flow and Transport in Heterogenous Media. Bulletin of Canadian Petroleum Geology.

Singh, K. et al. (2021) New type of pore-snap-off and displacement correlations in imbibition. Elsevier B.V.

Slichter, C.S. (1905) Field measurement of the rate of movement of underground waters.

Stewart, T.L. and Fogler, H.S. (2001) Biomass plug development and propagation in porous media. Biotechnol, pp. 353–363.

Stolten, D. et al. (2020) Robust Design of a Future 100% Renewable European Energy Supply System with Hydrogen Infrastructure.

Szyk, B. and Czernia, D. (2022) Online Calculation Tool for Enthalpy of Chemical Reactions. Omni Calculator. Available at: https://www.omnicalculator.com/physics/enthalpy.

Tarkowski, R. (2019) Underground hydrogen storage: Characteristics and prospects. Elsevier, pp. 86–94. Available at: https://doi.org/10.1016/j.rser.2019.01.051.

Tay, J.H., Liu, Q.S. and Liu, Y. (2001) The effects of shear force on the formation, structure and metabolism of aerobic granules., pp. 227–233.

The Engineering Toolbox (2021) Solubility of Gases in Water. Available at: https://www.engineeringtoolbox.com/gas-air-systems-t_22.html.

The Paris Agreement | UNFCCC (2015). Available at: https://unfccc.int/process-and-meetings/the-paris-agreement/the-paris-agreement (Accessed: 7 April 2022).

Thomas, R.L. and Gehle, R.M. (2000) A brief history of salt cavern use.

Thullner, M. (2008) Comparison of bioclogging effects in saturated porous media within one- and two-dimensional flow systems. Elsevier.

Tryggestad, C. et al. (2021) McKinsey & Company - Global Energy Perspective 2021.

Tweheyo, M., Talukdar, M. and Torsæter, O. (2001) Hysteresis effects in capillary pressure, relative permeability and resistivity index of north sea chalk.

U.S. Department of Health & Human Services (2021) 'ImageJ - Image Processing and Analysis in Java'. Available at: https://imagej.nih.gov/ij/.

USP (2015) General Notices, Requirements. United States Pharmacopeia. Available at: https://www.uspnf.com/sites/default/files/usp_pdf/EN/USPNF/usp-nf-notices/usp38_nf33_gn.pdf.

Van der Hart, P.-H.K. (2021) A Pore-Scale Study of Underground Hydrogen Storage in Porous Media. Master Thesis. University of Bergen.

Vandevivere, P. and Baveye, P. (1992) Relationship between transport of bacteria and their clogging efficiency in sand columns, pp. 2523–2530.

World Economic Forum (2021) '4 technologies that are accelerating green hydrogen revolution', World Economic Forum. Available at: https://www.weforum.org/agenda/2021/06/4-technologies-accelerating-green-hydrogen-revolution/.

World Energy Council (2020) International Hydrogen Strategies: A study commissioned by and in cooperation with the World Energy Council Germany. World Energy Council - Weltenergierat Deutschland.

Wu, T.L. (2022) 'Examining the Pros and Cons of Hydrogen Energy', Earth.org. Available at: https://earth.org/pros-and-cons-of-hydrogen-energy/.

Yao, K.-M., Habibian, M.T. and O'Melia, C.R. (1971) Water and waste water filtration. Concepts and applications. Environmental Science & Technology. American Chemical Society, pp. 1105–1112. Available at: doi: 10.1021/es60058a005.

Yue, M. et al. (2021) Hydrogen energy systems: A critical review of technologies, applications, trends and challenges. Elsevier. Available at: https://doi.org/10.1016/j.rser.2021.111180.

Zabranska, J. and Pokorna, D. (2017) Bioconversion of carbon dioxide to methane using hydrogen and hydrogenotrophic methanogens. Biotechnology Advances. Available at: https://doi.org/10.1016/j.biotechadv.2017.12.003.

Zivar, D., Kumar, S. and Foroozesh, J. (2020) Underground hydrogen storage: A comprehensive review.

Züttel, A. (2004) Hydrogen storage methods, pp. 157–172. Available at: https://10.1007/s00114-004-0516-x.

Appendix A

Appendix A

Several codes were written to extract specific data. A macro script was used to create the velocity and stress fields, including the creation of a npz.-file. This file stored all available velocity and stress data in an array. The python script was written to plot histograms with the aim to compare different time steps.

A.1 Macro script – create velocity and stress field

This code is copyright by Saeid Sadeghnejad (University Mainz).

```
# -*- coding: utf-8 -*-
"""
Created on Thu Nov 25 22:19:12 2021
@author: saeid
"""
import numpy as np
import struct


def calcShearForces(VelocityFieldPath = 'FlowField_z.vap', viscosity = 7.125e-4):
# computes shear forces: Tau = Mio*du/dx

    # load previous velocity field
    LoadVolumeField_args_1 = {
```

```
        'FileName'                  : VelocityFieldPath,
        'OverrideFileName'          : '',
        'Mode'                      : 'Selected',        #possible values: Selected, All
        'ComponentsToLoad'          : 'Velocity:Velocity',
        'KeepVolumeFields'          : False,
        'KeepCompression'           : 'DecompressIfPossible',   # Possible values: DecompressIfPossible, KeepCompression
        }
    gd.runCmd("GeoDict:LoadVolumeField", LoadVolumeField_args_1, "2021")
    V = gd.getVolumeField('Velocity')
    dV = np.gradient(V) #  gradient of velocity field
    magnitude = np.sqrt(np.square(dV[0]) + np.square(dV[1]) + np.square(dV[2]))
    shear = magnitude*viscosity

    # np.savetxt('Velocity.csv', V.flatten(), delimiter=',')
    # np.savetxt('Stress.csv', shear.flatten(), delimiter=',')
    # np.save('Velocity2', V.flatten())
    np.savez_compressed('Velocity.npz', V.flatten())
    np.savez_compressed('Stress.npz', shear.flatten())



    # visualize stress field in GD
    addNewField2vapFile(vap_file_path=VelocityFieldPath, property=shear)


def addNewField2vapFile(property, vap_file_path='FlowField_z.vap',
                        new_vap_file_name='test.vap', HeaderLength = 2048):
    '''
    This funciton addes a new field (property) to a previous .vap file,
```

```
save it with a new name and reload it into unser interface of GD.
It changes the header of vap file to include the 4th image (property) to V, Vx, Vy, Vz, and P


Paramerters:
-vap_file_path      : the old .vap file
-new_vap_file_name  : the name of new .vap file
-property           : the property that should be added to the vap file (3D numpy array)
-HeaderLength       : the size of header of .vap file
'''


info      = gd.getVolumeFieldsInfo()
nx, ny, nz = info[0]['dimensions']
#find the actual end of header
with open(vap_file_path,'rb') as input:
    aByte= input.read(1)
    eoh = 0
    while aByte and ord(aByte) != 0:
        aByte= input.read(1)
        eoh += 1
print('eoh= ',eoh)


# extract header and data in byte
with open(vap_file_path,'rb') as input:
    header = input.read(HeaderLength)   #1011  1131 (including the last enter (\n))
    data   = input.read() # velocity, velocityX, velocityY, velocityZ, Pressure
# adding new headers, 4th image (property))
HeaderLines = header.splitlines()   # split into a list of string
```

```
# adding new headers for the 4th image (property filed)
HeaderLines.insert(31, b'Image3:Names          Stress')
HeaderLines.insert(32, b'Image3:Units          Pa')
HeaderLines.insert(33, b'Image3:Types          float')
HeaderLines.insert(34, b'Image3:Grids          center')
HeaderLines.insert(35, b'NumberOfImages        3')
HeaderLines.insert(36, b'NamesOfImages         Velocity,Pressure,Stress')
HeaderLines.insert(37, b'EntriesOfImages       3,1,1')
HeaderLines.pop(38)
HeaderLines.pop(38)
HeaderLines.pop(38)
HeaderLines.pop(38)
# make an empty array of bytes to fill the header untiel HeadreLength
# ATTENSION: if the name of property changes (here Stress=121 bytes),
# the header length should be adjusted in the llowing line
HeaderLines.insert(39, bytes(bytearray(HeaderLength-eoh-121)))

# write to a new file
with open(r'test.vap','wb') as f:
  for l in HeaderLines:
    f.write(l)
    f.write(b'\n')
  f.write(data)
  # ‘F’ means to flatten in column-major (Fortran- style) order
  f.write(struct.pack('f'*property.size, *property.flatten('F')))

#load new volume field
LoadVolumeField_args_1 = {
```

```
    'FileName'                    : new_vap_file_name,
    'OverrideFileName'                : '',
    'Mode'                          : 'Selected',       #possible values: Selected, All
    'ComponentsToLoad'                : 'Velocity:Velocity',
    'KeepVolumeFields'                : False,
    'KeepCompression'          : 'DecompressIfPossible',       #       Possible       values: DecompressIfPossible, KeepCompression
    }
  gd.runCmd("GeoDict:LoadVolumeField", LoadVolumeField_args_1, "2021")


# Main
calcShearForces()
```

A.2 Python script – plot histogram

This code is originally from Saeid Sadeghnejad (University Mainz) and modified by Pit Arnold (Montanuniversity Leoben).

```
#!/usr/bin/env python3
# -*- coding: utf-8 -*-
"""
Created on Thu Jul 21 09:18:48 2022
@author: saeid
"""
from math import log10, floor
import time
import numpy as np
import matplotlib.pyplot as plt
# from scipy.stats import norm
# import statistics
plt.style.use('seaborn-deep')
```

```
#---------------------
# *** input params ***
NoTimeSteps = 3
UseScaleing = False # scale graphs or use the default value; True - Scaling; False - NoScaling

bin_V = 100
xlim_Vo = (0, 1e-2) # o...plot oben
ylim_Vo = (0, 1e8)
xlim_Vu = (0, 1e-3) # u...plot unten
ylim_Vu = (0, 1.4e8)

bin_S = 100
xlim_So = (0, 3.5e-6)
ylim_So = (0, 1e8)
xlim_Su = (0, 1e-6)
ylim_Su = (0, 1.75e8)

bin_log = 100

#---------------------

# load dict of arrays
V = []
S = []
plt.figure(1)

st = time.time()
```

```
exp_minV = 0

exp_maxV = -30

exp_minS = 0

exp_maxS = -30


#function to find exponent for logarithmic plotting

def find_exp(number) -> int:

    base10 = log10(number)

    return floor(base10)


for i in range(NoTimeSteps):

    V.append(np.load(f'Velocity{i+1}.npz'))

    V[i] = V[i]['arr_0']

    S.append(np.load(f'Stress{i+1}.npz'))

    S[i] = S[i]['arr_0']


    et = time.time()


    elapsed_time1 = et - st


    print('Execution time loading: ', elapsed_time1, 'seconds')


    # removing of zero elemens (solid structure)

    V[i] = V[i][V[i]!=0]

    S[i] = S[i][S[i]!=0]

    print(len(V[i]), len(S[i]))
```

```
et = time.time()

elapsed_time1 = et - st

print('Execution time removing zeroes: ', elapsed_time1, 'seconds')

# meanV = statistics.mean(V[i])

# et = time.time()

# elapsed_time1 = et - st

# print('Execution time calculating Mean Value: ', elapsed_time1, 'seconds')

# stDV = statistics.stdev(V[i])

# et = time.time()

# elapsed_time1 = et - st

# print('Execution time removing Standard Deviation: ', elapsed_time1, 'seconds')

minV = min(V[i])
maxV = max(V[i])

minS = min(S[i])
maxS = max(S[i])
```

```
exp_min_calcV = find_exp(minV)

if exp_min_calcV < exp_minV:

    exp_minV = exp_min_calcV
exp_max_calcV = find_exp(maxV)

if exp_max_calcV > exp_maxV:

    exp_maxV = exp_max_calcV

exp_min_calcS = find_exp(minS)

if exp_min_calcS < exp_minS:

    exp_minS = exp_min_calcS

exp_max_calcS = find_exp(maxS)

if exp_max_calcS > exp_maxS:

    exp_maxS = exp_max_calcS



# print('Mean value: ', meanV)
# print('Standard Deaviation: ', stDV)
print('Minimum Value Velocity:', minV)
print('Maximum Value Velocity:', maxV)
```

```
    print('Minimum Value Stress:', minS)
    print('Maximum Value Stress:', maxS)

    print('Minimum Exponent Velocity:', exp_minV)
    print('Maximum Exponent Velocity:', exp_maxV)
    print('Minimum Exponent Stress:', exp_minS)
    print('Maximum Exponent Stress:', exp_maxS)

    # plot velocity
    plt.subplot(221)
    _ = plt.hist(V[i] , histtype='step', bins= bin_V, alpha=0.5, label=f'Scan {(i+5)*i}')  # arguments are passed to np.histogram
    plt.yscale('log')
    plt.title("Histogram of velocity")
    plt.legend(loc='upper right')
    plt.xlabel('Velocity (m/s)')
    plt.ylabel('Counts')
    if UseScaleing:
        plt.xlim(xlim_Vo)
        plt.ylim(ylim_Vo)

    plt.subplot(223)
    _ = plt.hist(V[i] , histtype='step', bins= np.logspace(exp_minV,exp_maxV, bin_log), alpha=0.5)  # arguments are passed to np.histogram
    plt.xscale('log')
    plt.xlabel('Velocity (m/s)')
    plt.ylabel('Counts')
    if UseScaleing:
```

```
        plt.xlim(xlim_Vu)
        plt.ylim(ylim_Vu)


    # Plot stress
    plt.subplot(222)
    _ = plt.hist(S[i] , histtype='step', bins= bin_S, alpha=0.5, label=f'Scan {(i+5)*i}')  # arguments are passed to np.histogram
    plt.yscale('log')
    plt.title("Histogram of stress")
    plt.xlabel('Stress (Pa)')
    plt.ylabel('Counts')
    plt.legend(loc='upper right')
    if UseScaleing:
        plt.xlim(xlim_So)
        plt.ylim(ylim_So)


    plt.subplot(224)
    _ = plt.hist(S[i] , histtype='step', bins= np.logspace(exp_minS,exp_maxS, bin_log), alpha=0.5)  # arguments are passed to np.histogram
    plt.xscale('log')
    plt.xlabel('Stress (Pa)')
    plt.ylabel('Counts')
    if UseScaleing:
        plt.xlim(xlim_Su)
        plt.ylim(ylim_Su)


    et2 = time.time()
```

```
    elapsed_time2 = et2 - st


    print('Execution one loop: ', elapsed_time2, 'seconds')


plt.tight_layout()

plt.show()
```

List of Figures

List of Tables

Nomenclature

K	Permeability	[D]
ϕ	Porosity	[-]
R	Radius	[m]
Min	Minutes	[min]
h	Hours	[hours]
q	Flow rate	[ml/h]
C	Celsius	[°C]

Abbreviations

ATR	Autothermal Reforming
BC	Boundary Conditions
CCS	Carbon Capture and Storage
CCUS	Carbon Capture Utilization and Storage
CH_4	Methane
CO_2	Carbon Dioxide
ED	Empty Domain
EPS	Extracellular Polymeric Substances
EU	European Union
Exp. 1/2	Experiment 1/Experiment 2
GDP	Gross Domestic Product
GHG	Green House Gas
H_2	Hydrogen
H_2O	Water
LHV	Lower Heating Value
L. Casei	Lactobacillus Casei
MM	Micro Model
M. formicicum	Methanobacterium Formicicum
Pe	Peclet Number
PFPs	Preferential Flow Paths
POX	Partial Oxidation
PtX	Power-to-X
RE	Renewable Energy
RMSE	Root Mean Square Error
SMR	Steam Methane Reforming
TD	Total Domain

UHS	Underground Hydrogen Storage